Atomistic Simulations of Ferroelectric Lead Zirconate Titanate

Oliver T. Gindele

A dissertation submitted in partial fulfillment

of the requirements for the degree of

Doctor of Philosophy

of

University College London.

Department of Physics and Astronomy

University College London

February 8, 2017

I, Oliver T. Gindele, confirm that the work presented in this thesis is my own. Where information has been derived from other sources, I confirm that this has been indicated in the work.

List of Publications

- Published: O. Gindele, A. Kimmel, M. G. Cain, and D. Duffy, Shell Model force field for Lead Zirconate Titanate $Pb(Zr_{1-x}Ti_x)O_3$, The Journal of Physical Chemistry C 119, 17784 (2015).

- Submitted to Applied Physics Letters Materials: O. Gindele, C. Vecchini, P. Thompson, M. Stewart, M. G. Cain, D. M. Duffy, and A. Kimmel, Low Temperature Ferroelectric Behavior in Morphotropic $Pb(Zr_{1-x}Ti_x)O_3$

- In preparation: O. Gindele, R. Cohen and D. Duffy, Electrocaloric Effect in $Pb(Zr_{1-x}Ti_x)O_3$ from Molecular Dynamics Simulations

- In preparation: O. Gindele, J. Chapman, A. Kimmel and D. Duffy, Defect Mediated Stabilization of Charged head-to-head and tail-to-tail 90° Domain Walls in $BaTiO_3$ and $PbTiO_3$

Conference Contributions

- Poster presentation, New force field for $Pb(Zr_{1-x}Ti_x)O_3$ and its application for modelling domain walls under strain, PIEZO 2015, Maribor, Slovenia

- Poster presentation, Local structure of strained mono- and multi-domain $Pb(Zr_{1-x}Ti_x)O_3$, ISAF 2015, Singapore, Singapore

- Poster presentation, The Effect of B-Cation Clustering on the Piezoelectric and Dielectric Response of $PbZr_{0.5}Ti_{0.5}O_3$, EMF 2015, Porto, Portugal

- Talk, Stability of neutral and charged domain walls in $PbTiO_3$ and $BaTiO_3$ from first-principles, TYC Student Day 2015, London, UK

- Poster presentation, Evolution of the local structure of $PbZr_{0.5}Ti_{0.5}O_3$ with applied electric fields, FERRO 2016, Washington D.C., USA

Abstract

Ferroelectric materials are of technological importance for many applications and a thorough understanding of the origins of their high piezoelectric and dielectric properties is needed to optimise materials performance. One of the most widely used ferroelectrics is $Pb(Zr_{1-x}Ti_x)O_3$ (PZT), which shows excellent piezoelectric response near its morphotropic phase boundary (MPB). To study PZT in large scale molecular dynamics (MD) simulations, I have developed a shell model force field that reproduces the details of the phase diagram of the PZT solid solution. The developed force field supports the temperature induced phase transitions from cubic to low symmetry phases over the whole composition range and additionally reproduces the composition driven phase transitions. This force field was subsequently used to study a variety of different effects in PZT. First, the polarisation switching in near morphotropic PZT at different temperatures was investigated, where I report a reduction of the saturation polarisation, accompanied by an exponential increase of the coercive field, as the temperature decreased. The simulations further demonstrated that the switching mechanism is fundamentally different at low temperatures, where it occurs via polarisation rotation, than at high temperatures, where domain nucleation dominates. Second, a set of simulations on near morphotropic PZT showed that the response of the local structure to electric fields highly depends on the local B-cation environment. Furthermore, I find that B-cation clustering largely influences the piezoelectric properties of the material. In a third MD study the electrocaloric effect (ECE) in the PZT compound was calculated, finding that $PbTiO_3$ outperforms other compositions with its giant temperature change of 16 K. Lastly, density functional theory (DFT) calculations were performed to study defects and domain walls in the PZT end member $PbTiO_3$, where we show that the presence of a couple donor-acceptor defect pair stabilises charged head-to-head and tail-to-tail 90° domain walls in $PbTiO_3$.

Acknowledgements

I would like to express my special appreciation and thanks to my advisor Dorothy Duffy for all the support and encouragement she gave me. I appreciate all her contributions of time, knowledge and ideas to make my PhD experience productive. Her thoughtful guidance helped me to stay focused on the important tasks and to allowed me to grow as a research scientist.

Similar profound gratitude goes to Anna Kimmel who has been a great supervisor, even during her maternity leave. She provided countless insightful discussions and has motivated me through all three years. Her work ethic and determination was inspiring and I could always count on her immediate support.

I gratefully acknowledge the funding received towards my PhD from functional materials group at the National Physical Laboratory (NPL) and the Condensed Matter and Materials Physics (CMMP) group at UCL.

I would also like to thank Jacob Chapman with whom I shared a large part of my PhD experience and who has helped me many times with his ideas and contributions. My fellow post graduate students at NPL, Till Buchacher, Maciej Rokosz, Rui Lopes and Bin Chen, deserve another big thank you. They offered valuable inputs, kept the office entertained and often managed to put my work into perspective. Special thanks also goes to Markys Cain, Paul Weaver, Carlo Veccini, Pavlo Zubko, Martin Hytch, and Chris Pickard for all their helpful suggestions and advice. Further, to Ronald Cohen for all the supportive discussions, the knowledgeable contributions and his assistance in some of my work.

Finally, but by no means least, I would like to thank my family: my parents and my sister. They always supported me in all my pursuits and this accomplishment would not have been possible without them.

Da steh ich nun, ich armer Tor, und bin so klug als wie zuvor.

Johann Wolfgang von Goethe (Faust)

Contents

List of Figures

List of Tables

Chapter 1

Introduction

Ferroelectric materials have been intensively studied in the past 70 years due to their use in numerous applications, such as sensors, micro actuators, high frequency transducers and many more [3]. The key to the functionality of ferroelectric materials lies in the fact that these materials can adopt two or more polarisation states, which can be switched between by applying electric fields. Since all ferroelectric materials are also piezoelectric, a change in the polarisation will result in a change of strain, thereby coupling an external electric field to the mechanical state of the material. It is this electro-mechanical coupling that is exploited in most of the applications of piezoelectrics.

A prominent and widely used ferroelectric with a large piezoelectric response is lead zirconate titanate, $Pb(Zr_{1-x}Ti_x)O_3$ (PZT). This perovskite material is a solid solution of $PbTiO_3$ (PTO) and $PbZrO_3$ (PZO), which shows the best performance near the 48% Ti and 52% Zr mixture. Besides the composition in PZT, defects, such as vacancies and domain walls, are known to play a large role in the piezoelectric response of ferroelectrics. Even though PZT has been studied extensively [4], many open questions remain regarding its phase diagram, its B-cation arrangement and the interplay of defects with the polarisation switching. Of course, behind the motivation to study the underlying physics of PZT, and ferroelectrics in general, lies the urge to improve the material's properties for their use in devices and to incorporate their functionality into novel applications.

Accurate quantum mechanical calculations, particularly density functional theory (DFT), have been very successful in adding insight to the understanding of ferroelectrics over the past three decades. However, modelling disordered systems, such as PZT, or simulating features like domain walls or grain boundaries, requires large systems with thousands of atoms in order to replicate the details on a atomistic level. These large system sizes

make DFT calculations, that generally scale with $O(n^3)$ with the number of atoms (n), computationally very expensive. To overcome this size issue, classical simulations based on interatomic potentials can be used, since their demand of computational power are several orders of magnitudes lower. Unfortunately, this increase in efficiency comes at the cost of reduced accuracy and the loss of all electronic information. Nevertheless, deriving these potentials parameters from first-principles calculations, as for example from DFT, tends to produce potentials which replicate the important characteristics of the materials with an acceptable trade-off in precision.

Atomistic simulations, either classical or quantum mechanical, can shed light into the fundamental physics of materials by reaching beyond what's normally accessible by experimental procedures. This means that extreme or experimentally impossible conditions, such as high pressures, high temperatures or complex strain states, can be tested. Besides probing materials in different ways than in a laboratory setting, atomistic simulations provide a great amount of physical quantities that are usually not directly available from experiments. These can be atomic positions, atomic velocities, ionic charges, electronic density, pressure and the energy of the system. From these standard quantities many more material's properties can be derived. Last but not least, simulations offer an inexpensive and straight forward way to test theoretical models and compare them to experiments.

In this thesis, I built upon the advantages that atomistic simulation grants, and applied first-principles calculations and classical MD simulations to study different compositions of PZT, including PZO and PTO. The chosen methodology offers a great variety of topics to study in ferroelectric PZT, but I selected a few specific issues to investigate: The effect of the electric field on the polarisation and on the temperature in PZT. The influence of the B-cation arrangement on the piezoelectric properties and the effect of domain walls on the electronic properties in PTO.

The thesis is organised as follows: Chapter 2 summarises the important theory of ferroelectrics and gives a brief overview of the relevant materials. Chapter 3 describes the simulation and calculation methods with which the results of this work were obtained. The following five chapters then present results and detailed analysis of different research into ferroelectric PZT and PTO, with Chapter 4 describing the fitting and the characterisation of a shell model force field for PZT. This potential, which can be used in MD simulations, is an important outcome of this thesis and most results in the following chapters are based on

it. Chapter 4 further demonstrates the applicability of the force field to study domain walls and strain effects in PZT by utilizing MD simulations of up to half a million atoms. In chapter 5, the force field is then applied to study PZT in MD simulations with applied electric fields. Ferroelectric hysteresis loops of PZT are replicated and the effect of the B-cation, the temperature and the electric field on the switching dynamics are investigated. Chapter 6 offers a deeper analysis of the role of the B-cation arrangement in PZT and its effect on the piezoelectric properties. Different degrees of clustering and ordering of the B-site ions were studied with MD simulations. Chapter 7 discusses the electrocaloric effect, calculated from MD simulations, across the full compositional range of PZT, including PTO and PZO. This electrocaloric effect, which is particularly strong in PZT, can be used for solid state cooling. Lastly, Chapter 8 is a DFT study of charged head-to-head and tail-to-tail domain walls in PTO. Different point defects in PTO were analysed and it is shown how such defects can stabilise charged domain walls, which display great potential in improving piezoelectric devices. The cited references of all chapters can be found in the bibliography at the end of the thesis and the lists of figures and tables are available at the beginning.

The work presented in this thesis was completed between 2013 and 2016 in the Condensed Matter and Materials Physics (CMMP) group at University College London (UCL) and in the functional materials group at the National Physical Laboratory (NPL). All the simulations and the processing of the data have been performed using the computational facilities of UCL, NPL and the national supercomputer service ARCHER, for which CPU time was kindly provided by the UK's HEC Materials Chemistry Consortium (funded by EPSRC (EP/L000202)).

Chapter 2

Theory of Ferroelectric Materials

A ferroelectric material satisfies two conditions: It has two or more stable states with non-zero spontaneous electric polarisation in absence of an electric field and it has to be possible to switch between those two states. In most cases this switching relates to a reversal of the polarisation and it's the mechanism at the core of many of the applications of ferroelectrics.

For a spontaneous polarisation to occur in a crystal it has to be non-centrosymmetric. Crystals are grouped into seven systems according to the structure of their unit cells: triclinic, monoclinic, orthorhombic, tetragonal, rhombohedral (or trigonal), hexagonal, and cubic. Further, those 7 crystal systems consist of 32 point groups that reflect the symmetry of the crystal. Out of all the 32 crystallographic point groups, 21 are non-centrosymmetric and do not contain an inversion centre. Among these non-centrosymmetric groups 20 exhibit piezoelectricity, whereas one of these point groups contains symmetry elements which rule this effect out. The piezoelectricity occurring in materials without inversion symmetry is understood as a coupling of the electrical polarisation in a material to the mechanical strain. This effect leads to an accumulation of electrical charge when a mechanical stress is applied, which is called the direct piezoelectric effect. However, this response is reversible and a mechanical strain can be generated in a material with an applied electric field (indirect piezoelectric effect). Of those 20 groups that have no inversion centre and are, therefore, piezoelectric, 10 are pyroelectric, and they possess a unique polar axis. The pyroelectric effect in these materials generates an electric charge through change of temperature and is also reversible: the inverse response is called the electrocaloric effect. The produced charge in these materials appears on opposite faces of the crystal, specified by the polar axis. This direction is usually constant but in some materials the direction can be changed by an external electric field. Such materials are called ferroelectrics. By symmetry, all ferroelectric

materials are pyroelectric and all pyroelectrics are piezoelectric, but the reverse is not true. For example, ZnO is piezoelectric and pyroelectric but not ferroelectric, which means its spontaneous polarisation can not be reversed by an electric field [5].

Ferroelectric materials exhibit their spontaneous polarisation below a certain temperature called the Curie temperature. Above the Curie temperature, the material adopts a higher symmetry state with an inversion centre, therefore losing its ferroelectricity. Some materials, such as $BaTiO_3$, exhibit multiple phase transitions with temperature, which each change the crystal's point group [6]. The phases occurring in $BaTiO_3$, with increasing temperature, are as follows: rhombohedral, orthorhombic, tetragonal and cubic [6]. In the cubic phase, above the Curie temperature, no ferroelectricity is observed and the state is called paraelectric. The phases at lower temperature all have different symmetries and different directions of their polar axis, but they are all ferroelectric.

In this chapter we will have a brief look at the century long history of ferroelectrics and then explain the core concepts of the underlying theory of ferroelectricity. I will discuss the most prominent ferroelectric materials, especially PZT, which is the main subject of this thesis. This chapter should serve as introduction to all the concepts discussed in the following chapters, where more detailed information will be presented for each topic.

2.1 History of Ferroelectrics

Ferroelectricity and the materials in which this effect occurs have been studied for almost a century [3]. The first confirmed ferroelectric material was Rochelle salt ($KNaC_4H_4O_64H_2O$), which was first synthesised in 1655 by Seignette [3]. It was not until 1824, however, when pyroelectricity was discovered in Rochelle salt, amongst other materials, by Brewster [3]. At the end of the 19th century the Curie brothers then studied the pyroelectric effect in this salt in more detail [7]. It took another 40 years until Valasek took on his fundamental work on Rochelle salt, where he found an analogy between its dielectric properties and ferromagnetism [8]. Valasek's studies later led to the term ferroelectricity, which came from his comparison to the magnetic phenomena. Furthermore, Valasek was the first to measure the hysteretic behaviour of the polarisation in a ferroelectric, which is now known as a polarization vs. electric field (P-E) loop. In the following years, another potassium containing ferroelectric compound (KDP) was found by Bush and Sherrer and a first theoretical description of the phenomena was produced by Kurchatov [4]. After those first rather calm decades of ferroelectricity, interest sparked in 1940 with the discovery of $BaTiO_3$ (BTO), the classical ferroelectric perovskite, by Wainer and Salomon [3]. Soon, Ginsburg extended Landau's work on phase transitions to explain the phase transitions in BTO [4]. The discovery and the characterization of BTO marked the beginning of the ceramic transducer era and by the 1950s BTO transducers were well established. In this decade, further ferroelectrics, such as $KnBaO_3$, $PbTiO_3$, $PbZrO_3$ and sulphate containing compounds [3] were found. Those materials were all perovskites and after the success of BTO in various applications, scientists turned towards the lead containing ceramics. In particular, the solid solution of $PbTiO_3$ and $PbZrO_3$, abbreviated PZT, showed exceptional properties and a high Curie temperature [9] and consequently PZT replaced BTO in standard piezoelectric devices. In the 1960's and 1970's, many experimental studies using a variety of techniques, such as Raman, neutron, Brillouin, and Rayleigh scattering, were performed on the perovskite family. In this period the soft-mode theory of ferroelectrics was firmly established and during the subsequent decades more phenomena, such as relaxors and improper ferroelectrics, were discovered. Advances in synthesis of single crystals and thin films further expanded the knowledge in the growing field, as did the success of *ab initio* calculations on ferroelectric oxides [5]. On top of that, many more ferroelectrics, even organic ones, have been found in the last 30 years. As of today about 1000 of these

materials are known [4].

2.2 Perovskite Ferroelectrics and the Ferroelectric Phase Transition

The origin of ferroelectricity lies in the atomic arrangement of the ions in the crystal structure. In order to have a spontaneous polarisation a crystal has to be non-centrosymmetric (polar). However, there exist polar crystals with non switchable polarisation (for example wurtzite), therefore they are not considered ferroelectric [5]. The polarisation emerges as a dipole moment in the perovskite unit cell. Such a dipole moment is created through small displacements of the ions from the cubic perovskite structure. As seen for a classic perovskite ferroelectric in Fig. 2.1, the oxygen ions displace relative to the B-cations, leaving a non-zero dipole moment in the unit cell. Depending on which way the positively and negatively charged ions displace, the polarisation vector points up or down. In this simple picture the macroscopic polarisation is the sum over all unit cell dipole moments. Such a definition based on unit cell dipoles is, however, ill defined. This will be further explained in section 3.4.1.

In the perovskite family, ferroelectricity therefore exists through the symmetry lowering via a polar mode from a high symmetry (cubic, space group $Pm\bar{3}m$) structure. Often this polar mode is coupled to non-polar lattice modes and to the lattice strain. This is the reason for the large electromechanically coupling in ferroelectrics and it results in the very rich temperature-pressure phase diagrams of the perovskite oxides [5]. The symmetry breaking from the cubic phase to the lower symmetry polar phase (often tetragonal, space group *P4mm* as in Fig. 2.1) can also be described by Landau theory with the polarisation as the primary order parameter.

A defining property of a ferroelectric is the ability to switch between its discrete polarisation states. Since all ferroelectrics are also piezoelectric, this switching can be done with an electric field or with stress (strain). This coupling of strain and electric field (polarisation) is at the core of virtually all applications of piezoelectrics. Understanding the polarisation switching is important in order to improve piezoelectric devices. An established key measure that displays and quantifies the switching of a ferroelectric is the polarisation-electric field loop (P-E loop) and is very well documented for all conventional ferroelectrics. In contrast to a linear dielectric where polarisation vs. electric field would just produce a lin-

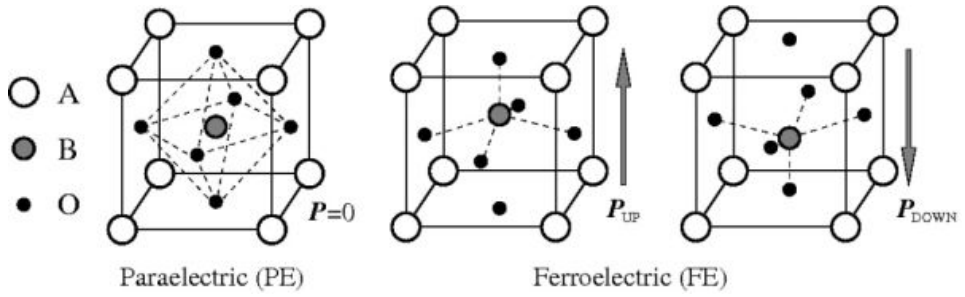

Figure 2.1: Structure of an ABO_3 perovskite in its paraelectric (cubic) and ferroelectric (tetragonal) phase. Reproduced from [10] with permission of the copyright owner under CC BY-NC-SA 3.0 license [11].

ear dependence, the P-E measurement results in a hysteresis (loop) as seen in Fig. 2.2. There are several experimental techniques to measure such a P-E diagram, all with subtle difficulties since leaky samples and bad contacting can produce misleading results. From the hysteresis curve one sees that the two polarisation states are stable within a certain range of electric field. At zero field one finds the remanent polarisation and the coercive field is also readily available from such a diagram as the zero polarisation value.

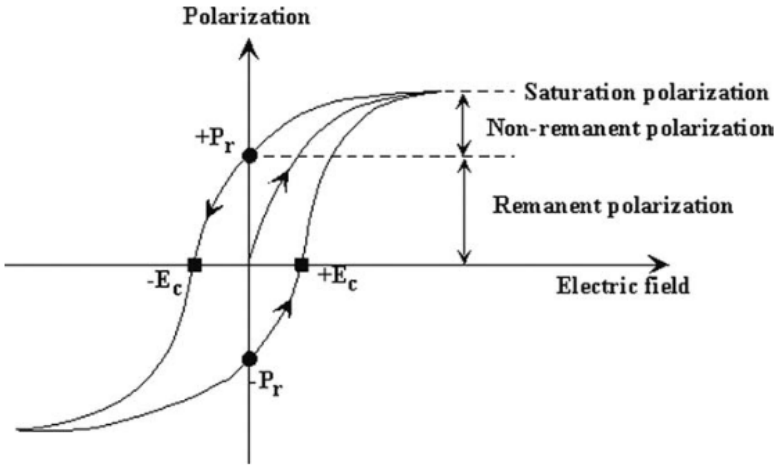

Figure 2.2: Characteristic polarisation vs. electric field (P-E) hysteresis of a ferroelectric. Reproduced from [4] with permission of the copyright owner.

2.3 Domains in Ferroelectrics

Going through the phase transition from the high symmetry state to the low symmetry phase a ferroelectric usually breaks up into parts of uniform electric polarisation: the ferroelectric domains. Such domains are energetically degenerate and separated by a region called a

domain wall. The driving force to create domain structures is the minimization of elastic and electrostatic energy in the material, including the energy associated with the creation of a domain wall. This means, the domain structure is strongly affected by factors that influence those energies, such as strain and electric field and it is, therefore, dependent on the processing [12] and the physical load. Domain walls are defined by the relative angle between the polarisation axis of the adjacent domains. In tetragonal ferroelectrics 180° and 90° domain walls (see Fig. 2.3) are encountered and they form in order to minimize the depolarizing energy or the strain energy, respectively [13]. In rhombohedral crystals 109° and 71° domain walls also occur. The 180° is distinct from most non-180° walls in that it does not respond to strain, only electric fields [14].

More generally, domain walls can be viewed as topological defects within the crystal structure of the ferroelectric [15]. They usually have very small widths of only a few nanometres and form a sharp structural interface between the domains. As mentioned above, strain and electrical boundary conditions play an important role in the formation of domain patterns. In thin films, for example, the domain patterns are dominated by the mechanical boundary conditions imposed by the substrate and the electrical boundary conditions of the free surface (or electrode). This will generally lead to different domain patterns than those present in bulk ferroelectrics [13].

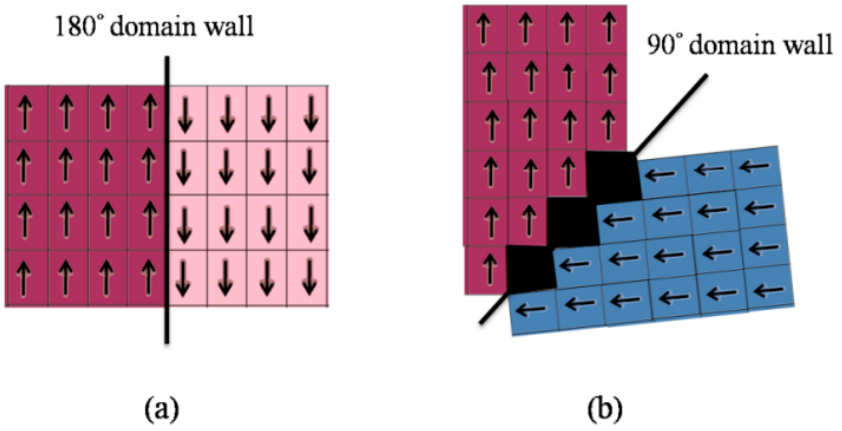

Figure 2.3: Schematic representation of (a) 180° and (b) 90° domain walls in a tetragonal ferroelectric crystal. The arrows designate the local polarisation. Reproduced from [16] with permission of the copyright owner under the CC BY-NC-SA 3.0 license [11].

Besides those boundary conditions, point defects in the vicinity of domain walls can also have a large influence on the domain structure and the mobility of the walls [15].

Such defects, for example oxygen vacancies, can lower the domain wall energy, effectively pinning the wall within the material [17]. This pinning of the domain walls lowers their mobility and therefore changes the response of the material to electric fields [17]. There are more ways in which domain walls can impact the properties of the whole ferroelectric, such as the finding by Seidel et al. [18], that domain walls act as conductive channels in insulating $BiFeO_3$ and the occurrence of charged domain walls in classical and improper ferroelectrics [19, 20], which influence the material's conductance and piezoelectric properties [21].

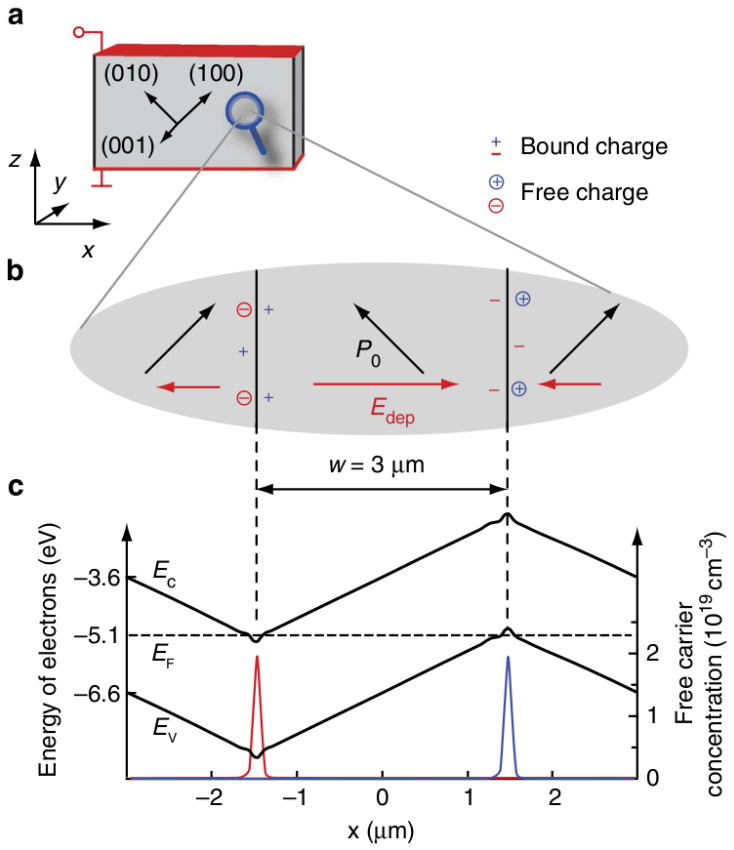

Figure 2.4: Sketch of charged 90° domain walls and their band structure. (a) Electroded $BaTiO_3$ plate. (b) 90° domain walls, where the black arrows designate the domain polarisation (P_0), which face head-to-head and tail-to-tail at the domain walls. The red arrow indicates the depolarizing field (E_{dep}). (c) Calculated band-structure [21] which shows the band bending induced by the E_{dep}. Free carriers are generated where the valence band or the conduction band crosses the Fermi energy. Reproduced from [21] with permission of the copyright owner under the CC BY-NC-SA 3.0 license [11].

Charged domain walls have only recently been confirmed experimentally [21], but propose great potential for enhancing ferroelectric properties or for usage in electronic devices

[19]. Originally, it was thought that charged domain walls, e.g. walls that carry a bound charge, are electrostatically "forbidden". However, Sluka et al. [21] proposed a model that explains the stability of charged domain walls and even suggests that they might enhance the electromechanical response in $BaTiO_3$. Fig. 2.4 shows the schematics of charged 90° domain walls, where the polarisation directions meet either head-to-head or tail-to-tail at the walls. This orientation leads to a build up of bound polarisation charge at the walls which has to be compensated by either defects or free charge carriers. If the bound charge is not fully compensated, a depolarising field will emerge which will in turn induce band bending. If the band bending is large enough, so that either the valence and or the conduction band crosses the Fermi energy, then free carriers (holes or electrons) are generated which will compensate the bound charge and increase the conductance at the domain walls [21]. The depolarising field might be strong enough to destabilise the ferroelectric state locally, which effectively removes the domain wall, or it could facilitate polarisation rotation in the domains. This polarisation rotation is believed to be the reason for an increased dielectric permittivity in BTO with a high density of charged domain walls [21].

We see that domain structure and domain walls largely influence piezoelectric performance, polarisation switching [22] and electronic properties of ferroelectric materials and more understanding of their effects is needed in order to fabricate improved or novel devices.

2.4 Electrocaloric Effect in Ferroelectrics

The electrocaloric effect (ECE) describes the cooling of a material by an applied electric field. It can be regarded as the inverse of the pyroelectric effect in ferro- or pyroelectrics, but more generally, it will appear in all dielectric materials [23]. The key concept behind the ECE is that the entropy (S) of a material changes as a function of the temperature (T) and applied electric field (E). This relationship can be used to construct cooling cycles via adiabatic, isothermal and constant E field steps. Such a cooling process is shown in Fig. 2.5 in a schematic diagram and starts with applying an electric field to a material. If this is done fast enough, so no heat transfer to a heat bath occurs, the step is adiabatic. The applied field orders the material's dipolar state, which in turn increases the temperature in the material. This temperature is then reduced by heat flow to a heat sink, also decreasing the material's entropy. Removing the field in a third step will result in adiabatic depolarisation, where the dipole moments disorder and the temperature is further reduced. This leaves the material in

a state with a lower temperature than the starting temperature and allows heat to be absorbed from a load.

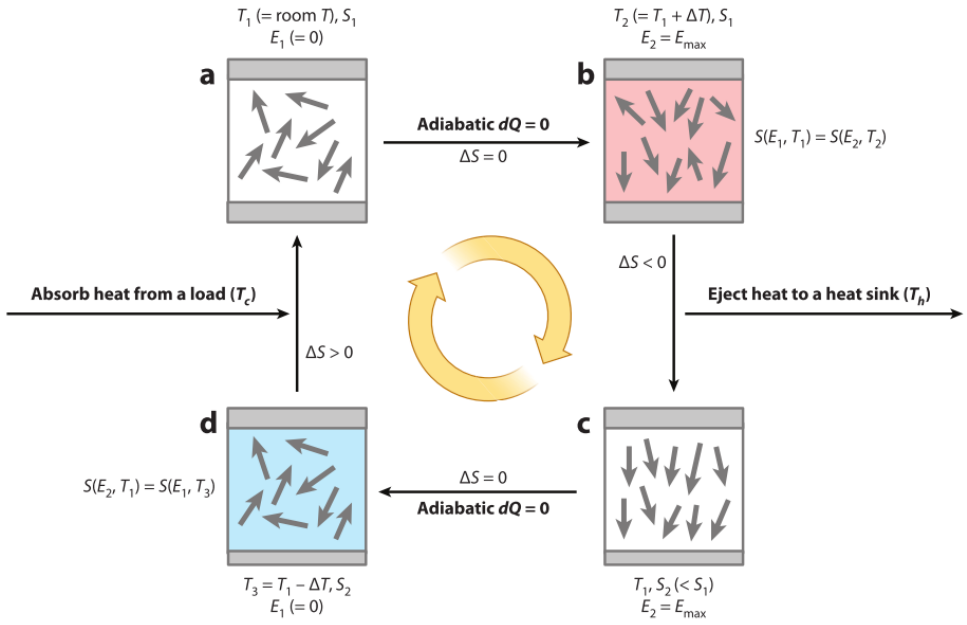

Figure 2.5: Electrocaloric cooling cycle. An applied electric field E heats the material from (a) to (b). The heat is ejected which reduces the entropy S in the material. Removing the field from (c) to (d) causes the material to cool further. Absorption of heat from a source allows the material to return to its original state (a). Reproduced from [24] with permission of the copyright owner.

This cooling cycle shows how the ECE can be used in solid state refrigeration and in novel miniaturised cooling devices which has resulted in a recent surge in interest [24] in this effect. Historically, the ECE has been known for many years and it was first described by Kobenko and Kurtschatov [25] as a small temperature change in Rochelle salt. The change in temperature in Rochelle salt was studied more accurately in later years and was found to be just a few mK [23]. Many dielectrics and ferroelectrics have been studied since, but mostly minute changes in temperatures were reported [23]. It was not until 2006, when the first so-called giant electrocaloric effect was reported by Mischenko [26] in $PbZr_{0.95}Ti_{0.05}O_3$. Many more publications on various materials followed and even surpassed Mischenko's seminal paper [23]. Fig. 2.6 shows the change in temperature vs. electric field for a few promising materials. With these recently found changes in temperature of few tens of K, actual solid state cooling devices based on the ECE might become a reality soon. The change in temperature (ΔT) reported in Fig. 2.6 requires rather large fields, but by using thin films instead of bulk ferroelectrics, such fields are accessible experimentally.

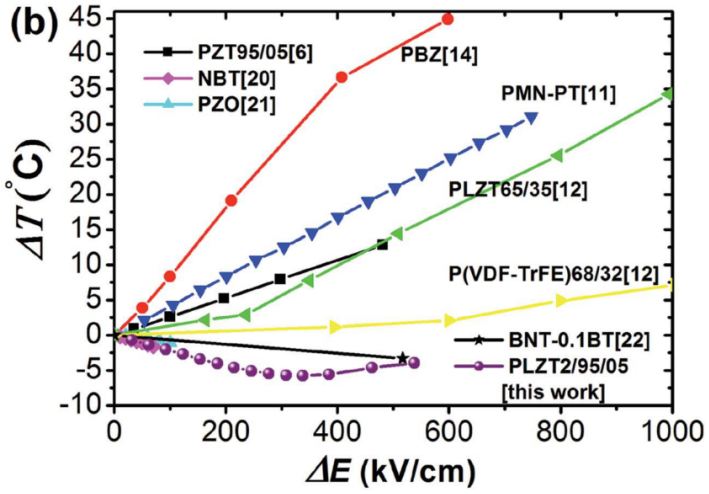

Figure 2.6: Change in temperature (ECE) with applied electric field for various materials. For the references please follow the original publication by Geng et al. [27]. Reproduced from [27] with permission of the copyright owner.

After all these years of research there is still no satisfying microscopic theory that explains the ECE [23]. Phenomenologically however, the ECE can be described by the Maxwell relations, which expresses the change in entropy (S) with electric field (E) at constant stress X as the change of polarisation (P) with temperature (T):

$$\left(\frac{\partial S}{\partial E_i}\right)_{T,X} = \left(\frac{\partial P_i}{\partial T}\right)_{E,X}, \tag{2.1}$$

where i is the component of the field or polarisation. From this equation the change in temperature can be calculated as [24]:

$$\Delta T = -\int_{E_1}^{E_2} \frac{T}{\rho C_E}\left(\frac{\partial P}{\partial T}\right)_E \mathrm{d}E \tag{2.2}$$

with ρ is the density and C_E is the specific heat capacity at constant electric field.

The ECE is therefore related to the change in polarisation with temperature, which can be calculated from simulations or measured in experiments, known as the indirect method. Typically, $(\frac{\partial P}{\partial T})$ is obtained from P-E hysteresis loops at different temperatures. Calculating the derivative of the polarisation in the vicinity of the phase transition can be difficult and the indirect method should therefore be applied with care [23]. The direct method, on the other hand, measures the actual change in temperature as a function of time, when the field is applied or removed. Several experimental techniques exist to measure the ECE with

the direct method such as Differential Scanning Calorimetry (DSC) or far infrared (IR) photometry. DSC measures the heat flow with time, while IR photometry measures the infrared intensity over time. Both methods are sensitive enough to detect the changes in temperature down to the mK range when an electric field is applied.

Until now, no commercial EC cooling device has been built, yet many patents have been filed and a few promising designs have been published [23]. Most noteworthy, a prototype of an electrocaloric oscillatory refrigeration (ECOR) chip, which is based on two EC devices, has been realized [28]. The ECOR chip with P(VDF-TrFE) as ECE material produced a temperature difference of 6 K between its hot and cold end [28].

2.5 Ferroelectric Materials

2.5.1 $BaTiO_3$

Barium titanate $BaTiO_3$ (BTO) is a simple ferroelectric perovskite with a 5 atom primitive unit cell (see Fig. 2.7). Its use from the 1950s onwards as a transducer and capacitor material made it a well established material to study ferroelectricity and phase transitions. Above 393 K BTO is in its paraelectric cubic state ($Pm\bar{3}m$) (see Fig. 2.7a) [6]. When cooled down BTO goes through a series of phase transitions, the first one being the cubic to tetragonal (*P4mm*, see Fig. 2.7b) transition at 393 K [6]. Below 278 K the orthorhombic phase (*Amm2*, see Fig. 2.7c) becomes stable until 183 K. Finally, the low temperature structure is rhombohedral (*R3m*, see Fig. 2.7d) [6].

All the phase transitions in BTO are accompanied by the displacements of Ti against the O octahedron, which happen along the polar axis respective for their phase. The polarisation of the ferroelectric phases are moderate with 27 μC/cm^2 for the tetragonal, 25 μC/cm^2 for the orthorhombic and 19 μC/cm^2 for the rhombohedral phases [6]. Compared to the more conventional lead containing ferroelectrics the polarisation and the piezoelectric coupling are rather low [29] in BTO. However, since BTO is a lead-free compound, a lot of research focusses on improving its piezoelectric performance for its use as an environmentally friendly alternative to PZT [29].

2.5.2 $Pb(Zr_{1-x}Ti_x)O_3$ (PZT)

Lead zirconite titanate $Pb(Zr_{1-x}Ti_x)O_3$ (PZT) is the solid solution of $PbTiO_3$ and $PbZrO_3$ (see Fig. 2.9), which makes up around 98 % of the total actuator market [30]. Its end member $PbZrO_3$ (PZO) is an antiferroelectric in the *Pbam* space group (see Fig. 2.8b)

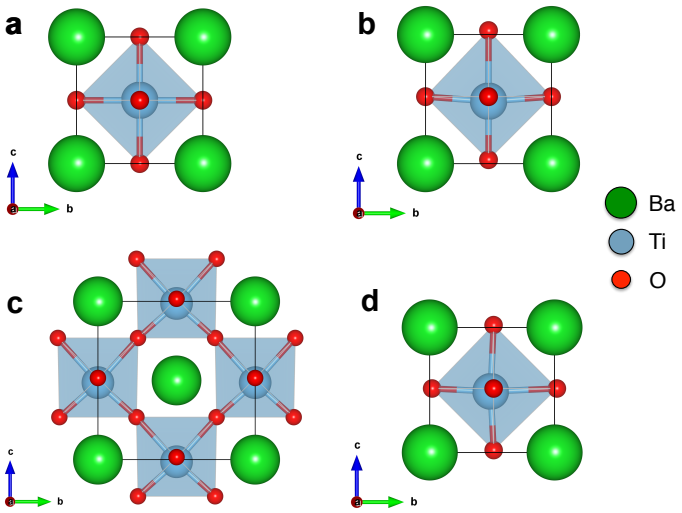

Figure 2.7: Crystal structures of the different phases of $BaTiO_3$. (a) cubic $Pm\bar{3}m$ (paraelectric, zero polarisation), (b) tetragonal *P4mm* (polarisation along [001]), (c) orthorhombic *Amm2* (polarisation along [011]) and rhombohedral *R3m* (polarisation along [111]).

at low temperatures. Its antiferrolectricity can also be described with the softening of a lattice mode, as in perovskite ferroelectrics. However, flexoelectric coupling transforms this phase into a missed incommensurate antiferroelectric one, where dipole moments within the unit cells cancel each other out [31]. The lattice parameters of PZO are $a = 5.886$ Å, $b = 11.749$ Å and $c = 8.248$ Å [32] in its 40 atoms unit cell. With small amounts of Ti, the system forms one of two rhombohedral phases (*R3c* and *R3m*) [33]. Figure 2.8c shows a small representation of this Zr rich part of the PZT solid solution in the *R3c* space group (polarisation direction along [111]). The right side of the phase diagram is dominated by the tetragonal ferroelectric $PbTiO_3$ (PTO) and the solid solution maintains the *P4mm* phase (see Fig. 2.8a) and the [001] polarisation direction of its right end member. The lattice parameters of PTO are $a = 3.899$ Å and $c = 4.153$ [34], while the oxygen octahedra in PTO (10.3 $Å^3$) are significantly smaller than the octahedra in PZO (11.8 $Å^3$).

The range between x=47% and x=52% Ti is called the morphotropic phase boundary (MPB) and has caught a lot of interest in research and applications in the last decades. The MPB is associated with the most favourable properties within the solid solution since the electromechanical coupling peaks at this composition range. This is explained by the competition between the tetragonal and rhombohedral phases at this composition. An applied electric field can therefore easily induce a transition between these phases and rotate the polarisation along $8 + 6 = 14$ directions. Newer studies on the MPB [35, 36] also show

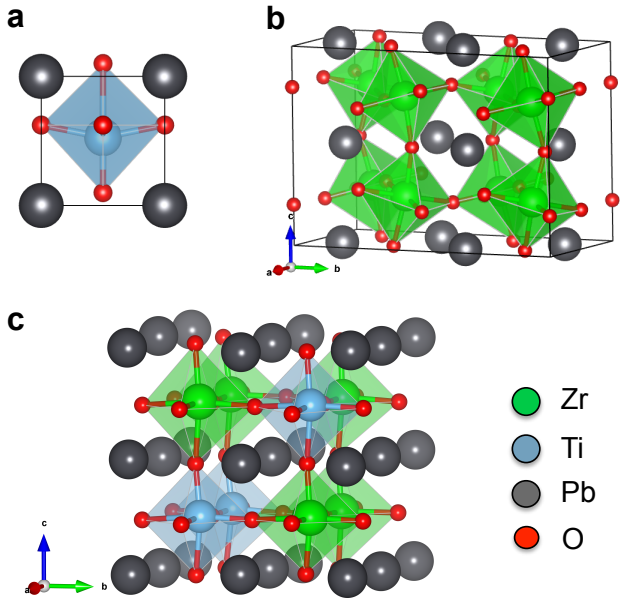

Figure 2.8: Crystal structure of (a) $PbTiO_3$ *P4mm* (polarisation along [001]), (b) $PbZrO_3$ *Pbam* (antiferroelectric) and (c) a representation of Zr-rich $Pb(Zr_{1-x}Ti_x)O_3$ in the *R3c* space group (polarisation along [111]).

monoclinic phases in vicinity of the MPB that facilitate this transition. Such a low symmetry phase is now believed to be responsible for the high piezoelectric response near the MPB. It is, however, still not clear whether such a phase is needed for enhanced properties and whether it exists in other lead based perovskites with an MPB [37]. Furthermore, novel research shows that these monoclinic phases coexists with a long-range average rhombohedral phase, that consists of low-symmetry structures at the local scale PZT [30]. Many open questions remain concerning the MPB and it is still a very active field of research expanding to other perovskite solutions.

Recently, some studies suggested that, in addition to the polarisation rotation, elastic softening of the lattice could be responsible for the large increase in piezoelectric response near the MPB [38]. Although in solid solutions with an MPB, the piezoelectric properties are greatly enhanced near the phase boundary, the existence of an MPB is not necessary for giant piezoelectric response. So called relaxor ferroelectrics ($PbZn_{1/3}Nb_{2/3}O_3$-$PbTiO_3$ and $PbMg_{1/3}Nb_{2/3}O_3$-$PbTiO_3$) show excellent piezoelectric behaviour without having an MPB [39]. Their piezoelectric coefficients can be an order of magnitude higher than in conventional ferroelectrics, so they are briefly discussed in the next section (2.5.3).

Since the Zr and Ti atoms have the same oxidation state (4+) they are randomly dis-

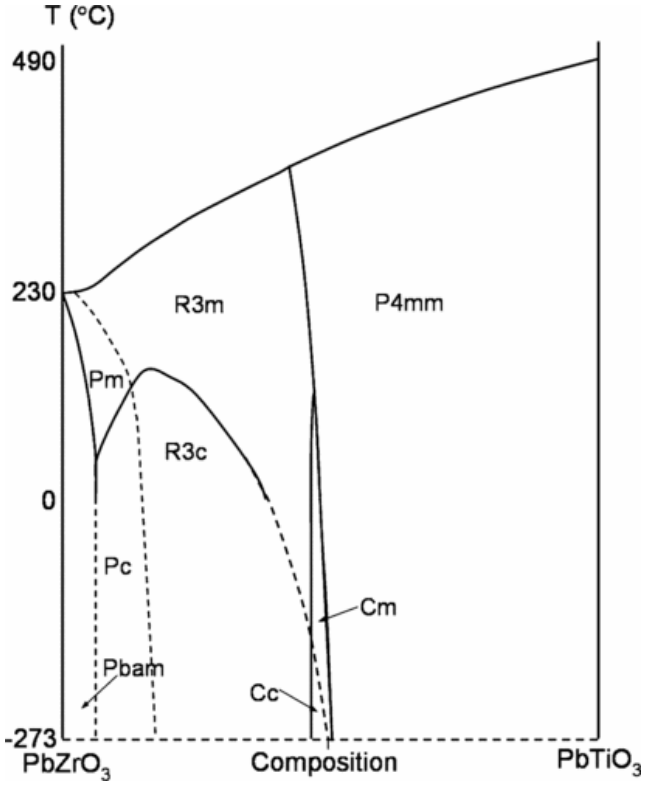

Figure 2.9: Phase diagram of $Pb(Zr_{1-x}Ti_x)O_3$. Reproduced from [33] with permission of the copyright owner.

tributed in the material, and no order is to be expected, due to electrostatic interactions [40]. However, a number of theoretical and experimental studies of PZT indicate that B-cations preserve a certain degree of order and clustering. In particular, a favourable ordering of B-cations along [100] and [111] directions was reported in [41] using ab-initio calculations. A long-range B-cation arrangement was found in PZT thin films grown on a $SrTiO_3$ substrate [42] and the existence of nanometre sized clusters of B-cations was shown in PZT bulk ceramics [43]. Recent results based on a multiphase description of the structure of PZT with composition in the vicinity of MPB (x=0.4) demonstrate that the permutation of B-site cations leads to the stabilisation of a variety of local phases, reflecting a relatively flat energy landscape of PZT in vicinity of the MPB. The specific clustering of B-cations and their arrangement into a preferred local phase significantly affects the ferro- and piezoelectric response of PZT. This provides pathways to control the properties of ceramic samples, especially in thin films where the chemical order is driven by film-substrate interactions.

2.5.3 Relaxor Ferroelectrics

A different class of ferroelectrics are the so-called relaxor ferroelectrics or relaxors. These materials display a characteristic frequency dependence of the dielectric constant (real and imaginary parts). In contrast to ordinary ferroelectrics, the peak of the dielectric constant around T_C is diffuse and strongly frequency dependent [44]. At high temperatures, relaxors are in a non-polar paraelectric phase similar to normal ferroelectrics. Cooling below the Burns temperature (T_B) induces a peculiar phase transition through which the material transforms into the ergodic relaxor state [44]. In this phase polar nanometre sized regions or polar nanoregions (PNRs) appear with random polarisation directions. Around T_B these PNRs are mobile, but upon further cooling, they will be frozen into a nonergodic state, similar to a dipole glass [44]. By applying a large electric field this nonergodic state can be transformed into a conventional ferroelectric phase, allowing for polarisation switching and its applications. One complexity of studying relaxors comes from the compositional disorder these materials usually exhibit [44]. As in PZT, the B-cations are randomly distributed, but in most cases the B-cations are not homovalent, leading to a random electric field within the material, which is believed to be the origin of their unusual dipolar behaviour [44].

Relaxor materials are widely used in industrial applications, because of their high dielectric and piezoelectric constants [45]. Moreover, their dielectric properties are stable over a rather wide range of temperatures, making these materials good candidates for ceramic capacitors [46]. One of the most prominent relaxor materials is the solid solution of $PbMg_{1/3}Nb_{2/3}O_3$ (PMN) and $PbTiO_3$ (PTO), often referred to as PMN-PT. PMN-PT single crystals are known for their high achievable strains (1.7 %) [47] and their excellent piezoelectric coefficient (d_{33} > 2500 pC/N) [45] , surpassing even PZT by almost an order of magnitude. Although, PMN-PT and other relaxor materials have already been implemented in many devices, further experimental and theoretical work is needed to fully understand these challenging but useful materials [45].

2.6 Applications of Ferroelectric Materials

Since all ferroelectrics show the piezoelectric and the pyroelectric effects [6] they are used in a variety of different applications, such as piezoelectric and pyroelectric sensors, generators, high frequency transducers, microactuators and infrared (IR) detectors [4]. More recently, interest in those materials comes from their potential use as non-volatile random access memories (NVRAM) [6]. Such memory devices would not require power to keep

stored data in memory, and bits written as polarized ferroelectric domains could be used for memory storage. To date, issues with this technology are fatigue of ferroelectric materials and the fact that generally a bit is destroyed during read out. Another possible route to ferroelectric memory cells are ferroelectric field effect transistors (FeFET). In those devices the dielectric gate is replaced by a ferroelectric gate (also dielectric) and the screening charge of the ferroelectric film is used to switch the semiconductor channel. Recent IBM research goes even further in implementing piezoelectrics into transistor technology. They designed a Piezoelectronic Transistor (PET) that uses a piezoelectric material coupled to a piezoresistive film [48]. An applied voltage on the piezo element can change the resistance in the piezoresistive layer and therefore act as a switchable conducting channel.

2.7 Motivation and Open Questions

The importance of ferroelectric and piezoelectric materials is clearly given by their numerous existing applications and the large potential for novel technologies these materials might support. Yet there is still a lot left to understand when it comes to the fundamental aspects of morphotropic solid solution perovskites like PZT or the contribution of domains to the material response. Atomistic simulations can help tackle these questions, since they allow the modelling of such materials at the relevant length and time scales. In this thesis molecular dynamics simulations and density functional theory calculations are used to gain further insight into a few areas of active PZT research: In chapter 4 a potential is developed to study PZT in large scale molecular dynamics simulations. This force field is then used in chapter 5 to study morphotropic PZT under applied electric fields, in chapter 6 to investigate the effect of B-cation disorder in PZT and in chapter 7 to quantify the electrocaloric effect in PZT. Chapter 8 concludes this work with density functional theory calculations on charged domain walls in PTO.

Chapter 3

Methods

Computer simulations have become an important element in all of modern science, including materials science. This success can be attributed to the striking increase of computational processing power, roughly following Moore's Law, and to the development of efficient algorithms. Nowadays, numerous material properties can be calculated from atomistic simulations, providing insight into the underlying physics of materials. This chapter introduces molecular dynamics simulations, an approach based on classical potentials, and density functional theory, a quantum mechanical method. Both methods are used in this thesis to study ferroelectric oxides in different conditions and configurations. The full details of each simulation are described in the relevant results sections.

3.1 Simulation Approaches to Study Ferroelectric Oxides

Atomistic simulations aim to reproduce the physics of materials, or molecular systems and can be divided into two categories: classical calculations based on potentials and quantum mechanical calculations. In the classical atomistic simulations the interactions between the atoms (particles) are approximated by potential parameters (force field), which are derived empirically or from quantum mechanical calculations. The functional form of these potentials is generally simple so that many particles can be simulated with a relatively low computational effort. This efficient approach can be useful to simulate large collections of atoms, such as in dense materials or in biological systems. Of course, results will depend heavily on the potential parameters which makes deriving appropriate parameters for classical simulations a challenging task (see section 3.2.3).

On top of the positions and velocities of the atoms, quantum mechanical simulations include the interactions between the electrons. This is done by solving Schrödingers equation which gives information about the electronic structure of the studied material. Since this method includes the electronic interactions that form the chemical bonds explicitly instead of approximating it by a potential, quantum mechanical methods are, generally, more accurate than their classical counter part. Furthermore, they can be used to study effects that depend on the electronic structure such as spectral properties.

Both varieties of atomistic simulations can be used to study the same physical systems, but there is a trade off in computational cost and accuracy between those methods. There are further techniques to simulate materials that don't rely on atomistic degrees of freedom. The effective Hamiltonian method for example, is a powerful method to investigate ferroelectrics based on the soft-mode theory [49]. Following a Landau type energy expansion, a simplified Hamiltonian is constructed that includes the relevant ferroelectric degrees of freedom. The parameters of the Hamiltonian are usually fitted to first-principles simulations and are derived independently. This is an advantage over force field methods where all the parameters are optimized simultaneously. Further methods like Monte-Carlo simulations and phase-field models have also been successfully applied to study ferroelectric oxides [49].

3.2 Classical Molecular Dynamics

3.2.1 Interatomic Potentials

Molecular Dynamics (MD) simulations solve the classical equations of motion step by step using defined interactions between the particles and aim to model the relevant properties of the material as accurately as possible. These interactions can be bonded or non-bonded. Non-bonded interactions include, for example, pair potentials, Coulomb or higher order potentials. Bonding interactions model intramolecular bonds by including bond-lengths, bond angles and molecular torsion angles. For simulations of molecular systems and polymers, bonding terms are needed to accurately describe the covalent bond. In oxide materials, non-bonding interactions are generally sufficient due to the strongly ionic character of the bonds in these materials. Forms often used for these non-bonded pair potentials in oxide materials include Lennard-Jones or Buckingham potentials (see Fig. 3.1). The Buckingham potential consists of an attractive and a repulsive part and has the following form:

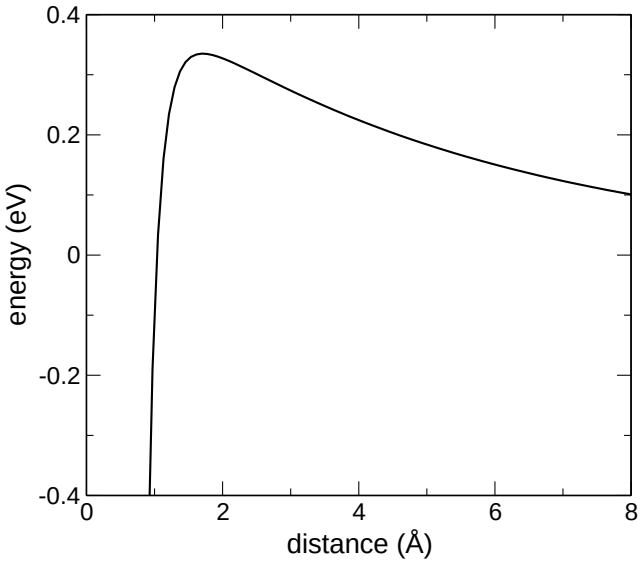

Figure 3.1: Buckingham pair potential.

$$V^{ij}_{Buckingham}(r) = A_{ij}\, exp\left(\frac{-r_{ij}}{\rho_{ij}}\right) - \frac{C_{ij}}{r_{ij}^6}, \tag{3.1}$$

where A_{ij}, ρ_{ij} and C_{ij} are parameters and r_{ij} is the separation between the particles i and j. To reduce the computational effort of calculating such short-range interactions, the potential is usually truncated at a certain distance (cut-off). Since this might lead to drifts in

energy when the potential is not close to zero at the truncation, the function is often shifted (smoothly or sharply) to approach zero at the cut-off.

In materials with charged particles, such as oxide (ionic) materials, the dominant force is the Coulomb interaction:

$$V^{ij}_{Coulomb}(r) = \frac{q_i q_j}{4\pi\varepsilon_0}\frac{1}{r_{ij}}, \tag{3.2}$$

with q_i being the charge on particle i, r_{ij} the separation between particles i and j and ε_0 the vacuum permittivity. Since the Coulomb force is long-range, it is not as easy to treat as other potentials. A truncation analogous to the short-range interactions would lead to charged spheres that badly converge with the cut-off radius. This problem was addressed by Ewald [50] in the 1920s and nowadays several ways to calculate electrostatic interactions in MD simulations are available. For periodic solids the Ewald sum is still the best technique [51] to calculate the Coulomb sum and with the smoothed particle mesh Ewald (SPME) method it has a very efficient implementation. The SPME decomposes the electrostatic interaction into a short-range part consisting of Gaussian screening charges. A second set of charges is superimposed in order to nullify the Gaussian charges, but this time on a grid in reciprocal space. This reciprocal part can be efficiently calculated via a fast fourier transformation (FFT). This way, the originally infinite Coulomb sum is replaced by two finite sums, one in real space and one in reciprocal space. Additionally, a self interaction energy corresponding to the Gaussians acting on themselves has to be included.

3.2.2 Shell Model

The so-called shell model adds another interaction to a force field that helps to stabilise the polar ferroelectric phases. In the shell model, each atom is composed of two charged, virtual particles: a positive core and a negative shell (see Fig. 3.2). Through this separation of charge, each atomic species becomes polarisable with a dipole moment specified by the displacement between core and shell. In the shell model applied in this thesis the core has a higher mass, the shell has a lower mass and the sum of the charges correspond to the total ion charge. The core and the shell interact via a spring potential of the form

$$V^{ij}_{Core-Shell}(r) = \frac{1}{2}k_2 r^2_{ij} + \frac{1}{24}k_4 r^4_{ij} \tag{3.3}$$

that keeps them from separating. Here r_{ij} denotes the core and shell separation, while

k_2 and k_4 are the spring constants. The shell model has been successfully applied to ferroelectric oxides since it was proposed by Dick and Overhauser [52]. Covalency effects are included through the atomic polarisability and can be extended for anisotropic behaviour (for example of oxygen) and anharmonic spring terms that further stabilize the tetragonal phase.

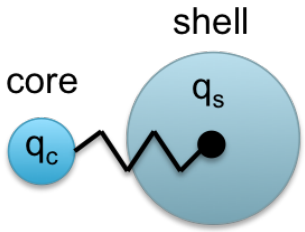

Figure 3.2: Diagram of the shell model. The atom is split into a core with charge q_c and shell with charge q_s that are connected by a spring (eq. 3.3).

3.2.3 Force Field Fitting

Once the functional form of the force field is chosen and it includes all the interactions needed to describe a material or molecule, the parameters of each interatomic potential have to be derived. There are two ways in which the parameters of the force field can be obtained: the force field can either be fitted to experimental data or data from *ab initio* calculations.

To perform a fit, a quantity that measures the quality of the fit is defined. Usually the sum of squares is used for this:

$$F = \sum_{i}^{obs} w_i (f_i^{calc} - f_i^{obs})^2. \tag{3.4}$$

Here w_i is a weighting factor, f_i^{calc} is the calculated value, while f_i^{obs} is the value of the observable. Whatever quantities are chosen as observables, F has to be minimized. The minimization can be done numerically with efficient algorithms like the Broyden-Fletcher-Goldfarb-Shanno (BFGS) [53] optimiser, which is also often used in geometry optimisations. Depending on the system and the number of variables this optimisation problem is not guaranteed to converge to a minimum. A successive approach of fitting a few parameters at a time while keeping others constrained might increase the chance of finding a satisfactory solution. Unfortunately, there is no general recipe on how to fit a force field and since the weight factors can be chosen freely there are infinite solutions to the problem. Addi-

tionally, systems with polarisable ions are very sensitive to parameters of the force field, so dynamic tolerances of the weight factors should be implemented. Careful testing of the force field is necessary, even if F has converged to a minimum.

3.2.4 Molecular Dynamics Algorithms

Besides static ground-state calculations like geometry optimisations, one can use interatomic potentials to perform dynamical simulations following Newton's equations. From the interatomic potentials $U(\mathbf{r})$ the atomic forces ($\mathbf{f}_i$) are calculated as derivatives with respect to the position of the ith particle ($\mathbf{r}_i$):

$$\mathbf{f}_i = -\frac{\partial}{\partial \mathbf{r}_i} U(\mathbf{r}^N). \tag{3.5}$$

Then Newton's equations can be written as

$$\dot{\mathbf{r}}_i = \frac{\mathbf{p}}{m_i} \tag{3.6}$$

$$\dot{\mathbf{p}}_i = \mathbf{f}_i, \tag{3.7}$$

where $\mathbf{p}_i$ is the momentum and m_i the mass of particle i. There exist many ways to integrate these coupled differential equations numerically in order to get the trajectory of all the particles with time. The Verlet-Algorithm in all of its forms is one of the most suitable [54] and most used MD algorithms. One of its forms, the Velocity Verlet (VV) algorithm is written, step by step as

$$\mathbf{p}_i(t + \frac{1}{2}\delta t) = \mathbf{p}_i(t) + \frac{1}{2}\delta t \mathbf{f}_i(t) \tag{3.8}$$

$$\mathbf{r}_i(t + \delta t) = \mathbf{r}_i(t) + \delta t \mathbf{p}_i(t + \frac{1}{2}\delta t)/m_i \tag{3.9}$$

$$\mathbf{p}_i(t + \delta t) = \mathbf{p}_i(t + \frac{1}{2}\delta t) + \frac{1}{2}\delta t \mathbf{f}_i(t + \delta t) \tag{3.10}$$

The VV algorithm conserves the volume in phase space, is time-reversible and is low-order, therefore allowing large timesteps. It also requires only one force calculation per timestep (forces are calculated after step from eq. 3.9), which makes it computationally efficient. The RATTLE [55] scheme can be incorporated within the VV code to include constrains on bond-lengths or angles, which is useful when the molecules exhibit high frequency vibrations.

In small bulk materials the use of periodic boundary conditions is essential. Even for a system with thousands of atoms, a significant number of atoms would be at the surface.

To realistically treat bulk materials, the system is replicated along the three cell vectors, eliminating all surfaces. The periodic box size should always be bigger than twice the cut-off to avoid particles interacting with themselves. With the introduction of the cut-off for the non-bonded potentials, the effort on the computation of the forces reduces greatly. However, there still needs to be a check performed for every particle to see if they are within the cut-off distance or not. This is very expensive for large numbers of atoms, so Verlet [56] proposed a technique to only consider atom pairs that will in fact lie within the truncation. So called neighbour lists are constructed for all neighbours that lie within the cut-off. Then for each particle the algorithm only loops through those lists (spheres around the particle) and calculates the forces. Obviously, particles will move out and into different lists with time, so careful checking and updating is necessary. Since neighbour list updates do not have to be performed at every timestep, this methods speeds up MD simulations significantly. An alternative approach, generally used in large systems, decomposes the box into cells (domains). Then the interaction partner of each particle is found within its own cell or the neighbouring cells. The decomposition in this so called linked-cell [57] algorithm can also be used to parallelise the code, treating each cell (plus neighbours) simultaneously, since they only slightly interact.

If all interatomic potentials relate to the potential energy of the system, then the total energy ($E_{tot} = E_{kin} + E_{pot}$) is conserved. In a system with fixed volume (V) and fixed number of particles (N) an MD calculation is then performed in the microcanonical ensemble (NVE). The temperature in an NVE ensemble should be relatively constant with small fluctuations. To simulate systems close to experiments or in order to explore phase stability controlling the temperature might be of interest. This can be done in several ways and will simulate a NVT ensemble. A straightforward way is to scale the velocities of all particles according to the Maxwell-Boltzmann distribution. This does not produce a canonical ensemble, it is however used to equilibrate systems from a different configuration or from a starting configuration far away from the equilibrium. Further approaches couple the system to a heat bath. This coupling can be weak as for the Berendsen [58] thermostat or strong as for the Nosé-Hoover thermostat [59, 60], which actually produces a canonical ensemble.

To directly simulate experimental conditions, one has to study systems with constant pressure (P) instead of constant volume. Such NPT ensembles further connect the system to a barostat, regulating the volume. Berendsen and Nosé-Hoover barostats are easily imple-

mented and work together with the thermostats. Other ensembles include the NST ensemble with constant stress (S) that allows relaxations of the cell parameters independently and the NPAT ensemble that keeps a constant area and relaxes the cell in one direction, are useful to study surfaces and 2D-like systems.

With simulations in those ensembles one can calculate all relevant properties (for example potential energy, volume, temperature, bond-lengths and more) as averages over time. Usually these averages are taken over a certain number of timesteps after the system has been equilibrated sufficiently long.

3.3 Density Functional Theory

For any given system the quantum mechanical wavefunction contains all the ground-state information about the system. To obtain this wavefunction (ψ) the Schroedinger's equation has to be solved which is in general a complex N-body problem. Density functional theory (DFT) maps this problem onto a much simpler one-electron problem, making it readily solvable using few approximations. The first simplification is the Born-Oppenheimer approximation, in which the electronic ground state is found within a configuration where the nuclei are frozen in space. This is justified through the largely different masses of electrons and nuclei which allows nuclei and electrons to be treated separately. This simplifies the problem of finding the wavefunctions of a given system but there is still the electron-electron interaction to be solved. Hohenberg and Kohn [61] made a first step to tackle this problem of electron-electron interaction by proving that the total energy of an electron gas is a unique functional of the electron density $n(\mathbf{r})$. Instead of finding the wavefunctions, one can, therefore, use the electron density as the relevant quantity of the system. The minimum of this functional of $n(\mathbf{r})$ is the ground-state energy of the system corresponding to the ground-state electron density. Kohn and Sham [62] went on to describe how to find such a functional by mapping the interacting electron system onto a system of non-interacting electrons in an external potential. This external potential has the same ground-state as the interacting electron potential so the exact ground-state can be defined with one-body electron wave functions ψ_i. The exact form of this external potential is unknown but can be approximated with great success for real systems. The framework that Hohenberg, Kohn and Sham provided is known as DFT and allows one to find the ground-state of any system by minimizing the density functional. This Kohn-Sham functional in natural units for the electronic energy (E_{el}) in a potential of fixed ions has the following form:

$$E_{el}[\mathbf{R}_k, \psi_i] = \sum_i^{occ} \langle \psi_i | -\frac{1}{2}\nabla^2 | \psi_i \rangle + \int v_{ext}(\mathbf{r}) n(\mathbf{r}) d\mathbf{r} + \frac{1}{2} \int \frac{n(\mathbf{r}_1) n(\mathbf{r}_2)}{|\mathbf{r}_1 - \mathbf{r}_2|} d\mathbf{r}_1 d\mathbf{r}_2 + E_{xc}[n], \tag{3.11}$$

where $\mathbf{R}_k$ is the position of ion k, ψ_i are the one-body wavefuntions and $n(\mathbf{r})$ is the electronic density at the position $\mathbf{r}$. The terms in eq. 3.3 correspond to kinetic energy, the electron-nuclei interaction through the electron-ion potential v_{ext}, the electron self interaction term and the exchange correlation energy $E_{xc}[n]$. The wavefunctions are orthonormal and the electron density is given by

$$n(\mathbf{r}) = \sum_i^{occ} \psi_i^* \psi_i. \tag{3.12}$$

In periodic solids the wavefunctions are usually expanded into Bloch functions (eq. 3.13 which is further explained in section 3.3.1). The exchange correlation ($E_{xc}[n]$) is unknown, but there are several functionals that approximate this term. The simplest one is the local density approximation (LDA) [63] which describes the exchange correlation as a functional of the electron density. Despite its simple and efficient approach LDA leads to good results, with one down side being that lattice constants are underestimated. Since the ferroelectric instability is very sensitive to pressure, inaccurate lattice constants can limit the use of LDA functionals. An improvement on LDA was to include gradient terms into the exchange correlation, a method known as generalized gradient approximation (GGA) [64]. Further approaches include meta-GGA and hybrid functionals which mix exact Hartree-Fock exhange into the exchange-correlations.

3.3.1 Basis Sets

In order to calculate the total energy via the Kohn-Sham equations (eq. 3.3) numerically the wavefunctions are expanded in some finite basis set [65]. In principle many types of functions could be used for the expansion and some of the most popular basis sets are Slater type orbitals (STO), Gaussian type orbitals (GTO) or plane waves (PW). For solids an expansion in plane waves is often used, since this basis set reflects the periodicity of the crystal. Together with a supercell approach the plane wave basis set can also be employed for finite sized, non-periodic systems. The plane wave expansion of a wavefunction (ψ_n) has the following form [65]:

$$\psi_{n,\mathbf{k}}(\mathbf{r}) = \sum_{\mathbf{G}} c_{n,\mathbf{k}+\mathbf{G}} e^{i(\mathbf{k}+\mathbf{G})\mathbf{r}} = e^{i\mathbf{k}\mathbf{r}} u_{n,\mathbf{k}}(\mathbf{r}). \tag{3.13}$$

where $\mathbf{G} = \sum_i n_i \mathbf{b_i}$, with n_i being integer and $\mathbf{b_i}$ being the lattice space vectors, $\mathbf{r}$ is a real-space vector, c_n the expansion coefficient and $u_{n,\mathbf{k}}$ has the periodicity of the lattice. For a complete representation of the wavefunctions a complete set of basis functions is needed which can require a large amount of plane waves (Fourier components). In practice, a finite basis set is used to restrict the number of plane waves, which reduces both the memory and the CPU demand. The size of the basis set (number of plane waves) is then determined by an energy cut-off (E_{cut}) which only includes plane waves with a kinetic energy below E_{cut} [65].

3.3.2 Pseudopotentials

The plane wave (PW) basis set described in the previous section (3.3.1) is not very practical to represent a solid with all its electrons: Because the inner wavefunctions close to the nucleis oscillate quickly, a very large number of plane waves is required to describe them accurately [65]. Fortunately, these inner wavefunctions are generally not involved in the formation of chemical bonds and the Coulomb potential around the core can be replaced by a weaker potential. This weaker potential is called a pesudopotential and it is much smoother around the core while it reproduces the valence region of the real atomic potential [65]. By removing the oscillations of the wavefunctions in the core region, the pseudo potential greatly reduces the number of plane waves needed which makes the PW basis set very practical to use.

3.4 Calculation of Ferroelectric Properties in Simulations

3.4.1 Calculation of Polarisation

A spontaneous, switchable polarisation is the defining characteristic of ferroelectric materials. The magnitude of the polarisation is routinely measured in experiments and reported, as it is a meaningful quantity for applications. It is therefore important to have efficient and accurate ways to calculate the polarisation, e.g. the macroscopic dipole moment in atomistic simulations. In the following paragraphs several possible routes to obtain the polarisation from simulations are briefly explained.

3.4.1.1 Calculation of Polarisation in DFT

The polarisation in atomistic or DFT simulations can be calculated via the Born effective charges (Z^*_{ij}) and the displacement of atom i from the centrosymmetric position (u_j) in each unit cell. The Born effective charge of an ion in a material with unit cell volume Ω is defined as $Z^*_{ij} = \frac{\Omega}{|e|}\frac{\delta P_i}{\delta u_j}$, with e being the elementary charge, is a measure of polarisation (P) in a ferroelectric. Further, it is a tensor that describes the amount each ion contributes to the spontaneous polarisation. Obtaining Z^*_{ij} in practice is straightforward since many available DFT and classical codes can calculate Born effective charges. The atomic displacements u_j can be extracted by subtracting a centrosymmetric reference cell from the simulated atomic structure. The polarisation is then retrieved through $P_i = Z^*_{ij}u_j$.

In DFT calculations such a unit cell based approach is ill-defined since the choice of unit cell is arbitrary and the electron density is delocalized. This can lead to wrong values of the polarisation and a different definition for polarisation on an atomic scale is needed. The framework of the modern theory of polarisation developed by King-Smith, Vanderbilt and Resta [66, 67] successfully defined not the polarisation but changes in polarisation as the intrinsic quantity. This change in polarisation can be calculated as a Berry phase or from maximally localized Wannier functions and is implemented in most DFT codes.

In practice, the route via Born effective charges is still often used, since it gives reasonable values for perovskite based ferroelectrics (see 8.1.2) and is easy to compute. In addition, by using $P_i = Z^*_{ij}u_j$, one can calculate a local polarisation, which is defined on a single unit cell. In a supercell simulation approach this can be used to obtain the polarisation locally and therefore determine its spatial variation in the whole system.

3.4.1.2 Calculation of Polarisation in MD

In classical simulations without electrons, the polarisation can still be accessed via Born effective charges or alternatively the ionic charges. Here, supercells are often used, allowing a better choice of reference and there are no delocalized electrons to be dealt with.

To calculate the polarisation of a periodic cell in MD simulations one can follow the approach of Sepliarsky et al. [68] and define a local polarisation for each B-cation centred unit cell. Such a cell consists of the B-cation in its oxygen octahedron and includes the 8 nearest A-site neighbours (compare with Fig. 2.1 for PTO). Taking the B-cation core as the reference point, all the contributions of all surrounding particles are added up according to eq. 3.14. Here, q_i and r_i are the charge and position of the particle i, while w_i corresponds

to a site specific weight to correct for shared atoms between cells. This sum is taken over all 29 particles and for each cell the polarisation is normalized by its volume Ω. This approach only minimally deviates from calculating the polarisation with atomic displacements and the Born-effective charges. For the PZT *P4mm* cell the difference between the two approaches is 0.3 $\mu C/cm^2$, with 43.2 $\mu C/cm^2$ calculated via Z^* and 42.9 $\mu C/cm^2$ via eq. 3.14.

$$P = \frac{1}{\Omega}\sum_i \frac{1}{w_i} q_i (r_i - r_B) \tag{3.14}$$

3.4.2 Calculation of the Piezoelectric Tensor

Dielectric and piezoelectric properties are further key quantities in studying ferroelectric materials and in judging their performance. Efficient and accurate routes to calculate these properties are therefore needed in order to characterize these materials using simulation methods. Two methods for obtaining these tensor properties in MD simulations are explained in the next paragraphs.

3.4.2.1 Derivative Based Calculation

One method to calculate the piezoelectric tensor stems directly from its definition: The piezoelectric tensor (d_{iv}) describes the linear coupling of the strain with the electric field, or alternatively the linear coupling of the polarisation with the stress, which both can be written in the following form [69]:

$$d_{iv} = \left(\frac{\partial \eta_v}{\partial E_i}\right)_\sigma = \left(\frac{\partial P_i}{\partial \sigma_v}\right)_E, \tag{3.15}$$

where η_v is the strain, E_i the electric field, P_i the polarisation, σ_v and the stress. The piezoelectric tensor is a third rank tensor. However, we can write it out in a convenient matrix form since the strain (η_v) and the stress tensors (σ_v) are symmetric, which reduces the number of independent components in the tensor from 27 to 18 in a triclinic crystal [70]. If the crystal has higher symmetry, the number of independent components is further reduced, as for example for the tetragonal *P*4*mm* point group which has only 3 independent components. Many important ferroelectrics exist in this tetragonal state and their piezoelectric coefficients are often written in the following matrix form:

$$d_{iv} = \begin{bmatrix} 0 & 0 & 0 & 0 & d_{15} & 0 \\ 0 & 0 & 0 & d_{15} & 0 & 0 \\ d_{31} & d_{31} & d_{33} & 0 & 0 & 0 \end{bmatrix} \tag{3.16}$$

Using eq. 3.15 to calculate d_{iv} is straight forward: Varying the electric field, while calculating the strain in a set of calculations will produce the η_v versus E_i behaviour which can be plotted. The slope of the field against the strain, e.g. $\left(\frac{\partial \eta_v}{\partial E_i}\right)_\sigma$, obtained through a linear fit is then the desired coefficient. To calculate the complete tensor the electric field has to be applied along all the relevant spatial directions.

3.4.2.2 Covariance Based Calculation

The second method for calculating the piezoelectric tensor (d_{iv}) is based on the covariance of the polarisation and the strain. This relationship can be written in the following form [69]:

$$d_{iv} = \frac{1}{k_B T} \langle \Delta P_i \Delta \eta_v \rangle, \tag{3.17}$$

where P_i the polarisation along direction i, η_v is the strain, T the temperature, k_B the Boltzmann constant, $\Delta X = X - \langle X \rangle$ and the averages are time averages.

This calculation can be performed on the fly in a molecular dynamics simulation but it generally requires very long run times [71] (for further information see section 6.1.1). One advantage of this approach over the derivative based method is that the whole tensor is obtained from a single simulation run. Furthermore, this approach can be used to calculate the piezoeletric tensor locally in small sections of the simulation cell.

Besides the piezoelectric coefficients, the electric susceptibility (χ_{iv}) can be calculated in a similar fashion as [71]:

$$\chi_{iv} = \chi_{\infty,iv} + \frac{1}{\Omega \varepsilon_0 k_B T} (\langle P_i P_v \rangle - \langle P_v P_i \rangle), \tag{3.18}$$

where Ω is the volume of the simulation cell, ε_0 the vacuum permittivity, T the temperature, k_B the Boltzmann constant and P_i the polarisation along i. Generally, the high frequency susceptibility is ($\chi_{\infty,iv}$) is small (5.7 for $BaTiO_3$) compared to the second term in eq. 3.18 and can be neglected [71]. From the susceptibility the dielectric constant (ε_r) is then calculated as $\varepsilon_r = 1 + \chi$. Again, very long simulation times are need to get accurate values of ε_r (and χ_{iv}) .

3.5 Software Used to Calculate Properties of Ferroelectric Oxides

The following presents a short description of the main software packages used in this work. All packages are suitable for large scale parallel calculations and are still under active development. Several further scripts have been used to create input files or to post-process the simulation output. Some of these scripts can be found under reference [72].

3.5.1 GULP

GULP the general utility lattice program [73] is a versatile package for symmetry adapted atomistic simulations. It can calculate a wide range of material properties, perform energy minimisation, geometry optimisations and MD simulations. In this thesis it was mostly used for force field fitting, geometry optimisations on small cells and force field testing.

3.5.2 DL_POLY_4

DL_POLY_4 [74] is a highly parallelised MD package that allows for simulations with up to 10^9 particles. It relies on the domain decomposition strategy to distribute particles over processors which makes it very efficient for simulations using large numbers of particles on a large processor count. DL_POLY_4 incorporates all standard potentials and boundary conditions to study molecules, biological systems and ionic compounds. The software package comes with a GUI and several useful utilities to build input files and analyse data. All MD results in this work were produced using DL_POLY_4.

3.5.3 CASTEP

CASTEP [75] is a DFT code based on plane-waves and pseudopotentials. It can calculate atomic structure, total energies and a wide range of properties like phonon dispersion curves and electrical response. Additionally, it can calculate IR, Raman, NMR and core level spectra. In this thesis CASTEP was used to calculate atomic structure and total energies.

3.5.4 CP2K

CP2K [76] is a code used to simulate atomistic or molecular systems. It incorporates classical potentials, as well as DFT methods based on a mixed Gaussian basis and plane-wave (GPW) approach. This approach makes the code very efficient for large systems, especially with the use of linear-scaling DFT methods. CP2K can also be used to perform MD or Monte Carlo simulations. In this report CP2K was used to calculate atomic structure and total energies.

Chapter 4

Fitting and Validating a Shell Model Force Field for $Pb(Zr_{1-x}Ti_x)O_3$

Complex perovskite solid solution materials, such as $A(BB')O_3$ or $AA'(BB')O_3$, are of great interest for actual or potential uses, based on their exceptional piezoelectric properties. One such material, lead zirconate titanate, $Pb(Zr_{1-x}Ti_x)O_3$ (PZT), is a technologically important compound due to its excellent piezoelectric properties [4]. PZT is a perovskite alloy of $PbZrO_3$ and $PbTiO_3$. One end member, $PbTiO_3$ (PTO) is a tetragonal ferroelectric [77], while $PbZrO_3$ (PZO) is characterized by an antiferroelectric ground state [78]. Neither compound exhibits particularly high piezoelectric properties, however, the solid solution of these materials gives rise to an exceptionally high piezoelectric response at a specific composition [79]. Further details on PZT can be found in section 2.5.2, including its intriguing phase diagram.

Understanding the properties of solid solution compounds at an atomistic level is particularly important for the design of high performance piezoelectrics. Density functional theory (DFT) calculations provide fundamental insight into the origin of ferroelectricity, domain wall behavior, grain boundaries and interfacial phenomena [80, 81, 82, 83]. However, modelling solid solution systems (in particular, PZT) with DFT is challenging: the disorder of the B-cations creates a statistical gap between small DFT accessible systems and the system size necessary to fully capture the effects of the disorder. Furthermore, defects such as vacancies or domain walls, play an important role in the piezoelectric response. Inducing such defects in simulations creates the need for even larger systems. To overcome this system size issue, I use large scale atomistic simulation with interatomic potentials based on the shell model, which has been shown to be a computationally efficient

method for studying ferroelectrics, while maintaining near DFT accuracy [84, 68].

A previous attempt to parametrise a shell model for the PZT compounds has been done by Kitamura et al. [85]. However, despite of the success of reproducing the low energy tetragonal phases of PTO and $Pb(Zr_{0.5}Ti_{0.5})O_3$, the force field [85] does not reproduce the antiferroelectric phase of PZO. Moreover, the force field does not predict the temperature induced phase transitions to high symmetry paraelectric phases of the three modelled compounds, i.e. PTO, PZO and $Pb(Zr_{0.5}Ti_{0.5})O_3$.

In this chapter I develop a shell model force field that reproduces the details of the phase diagram of $Pb(Zr_{1-x}Ti_x)O_3$, including the composition driven phase transitions at the morphotropic phase boundary (MPB). The force field also supports the temperature induced phase transition from low symmetry to high temperature cubic phases, as well as accurate structural properties of both end members of the PZT phase diagram, and represents an advance over currently published simulations.

The chapter includes two case studies which employ the PZT force field to show its applicability for molecular dynamics simulation of domains in ferroelectrics. Application 1 (section 4.3) shows the effect of strain on domains in PZT, while Application 2 (section 4.4) displays a proof of concept to simulate PZT ultra thin films under experimental conditions. The three following chapters (chapters 5, 6 and 7) further utilize the force field for more detailed investigations on PZT.

4.1 Fitting of the Shell Model Force Field

To develop a force field that reproduces the complex phase diagram of PZT, we would like to include all the possible interactions existing in PZT that we can infer from DFT calculations. This means different regions of the PZT phase diagram (see Fig. 2.9) with their different phases have to be analysed and incorporated. In order find stable phases in PZT for different compositions I used the results of structure searches. The structure searches were performed using the *ab initio* random structure searching (AIRSS) technique [86, 87]. The AIRSS technique generates a large ensemble of randomly generated structures with a reasonable starting volume and interatomic distances. A DFT code further preforms the energy optimisation of each of these structures. The CASTEP plane-wave code [75] with ultrasoft pseudopotentials [88] and the Wu-Cohen generalized gradient approximation functional [1] were used for further systems relaxation.

In order to probe the energy landscape of perovskite systems the AIRSS algorithm was strongly biased to preserve the ABO_3 topology. The potential energy surface was then sampled by supercells containing 1 to 8 formula units. Structure searching of the end members of the PZT phase diagram, PTO and PZO, demonstrated that PTO exhibits two stable phases: tetragonal (see Fig. 4.1a) and cubic. Meanwhile, PZO shows a diversity of phases depending on the supercell size (i.e. ferroelectric *P*4*mm*, *R*3*c* for 1-3 unit cells, antiferroelectric *Pbam*).

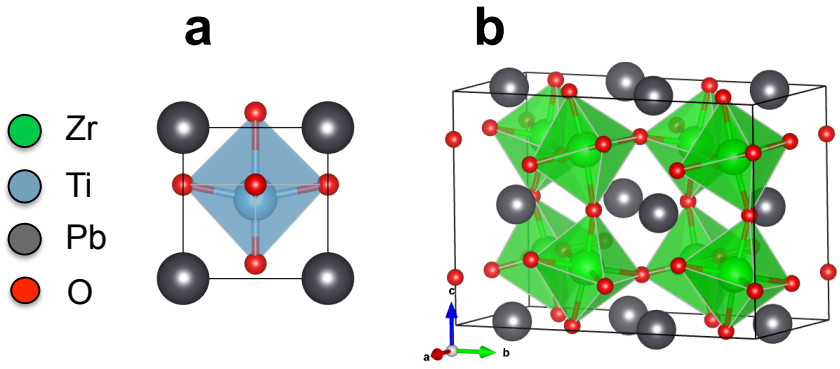

Figure 4.1: Crystal structure of (a) $PbTiO_3$ *P4mm* (polarisation along [001]), (b) $PbZrO_3$ *Pbam* (antiferroelectric).

The most stable phase was found to be *Pbam* (see Fig. 4.1b), while the least stable was the paraelectric $Pm\bar{3}m$ one. Sampling of the energy landscape of $Pb(Zr_{0.5}Ti_{0.5})O_3$ gave a large diversity of structures, in which stability strongly depends on the local arrangement of

B-cations. The most stable phase of PZT was found to be the ferroelectric *P4mm* structure. *P4mm* PZT is characterized by a checkerboard type order of Ti and Zr atoms within the ab-plane (Fig. 4.2a) and columns of B cations along *c* (Fig. 4.2b). For the force field fitting the most stable tetragonal phase of PZT, tetragonal and cubic phases of PTO and the most stable antiferroelectric and cubic phases of PZO were used. To consider the possible diversity in the Zr-O interactions the *R*3*c*, *Amm*2, and *P*4*mm* phases of PZO were also included, despite the fact that they are not found experimentally. Using these structures helped to incorporate the octahedron rotations found in the Zr rich part of the PZT phase diagram.

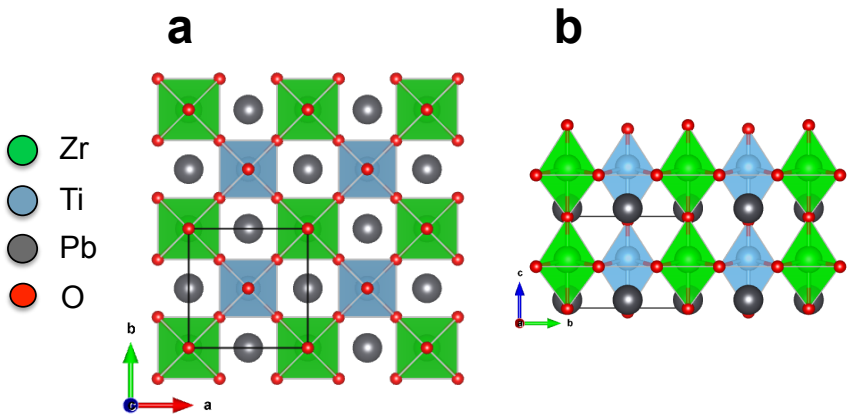

Figure 4.2: Crystal structure of PZT *P4mm*. a) view along *c* showing checkerboard ordering, b) view along *a* showing B-cation columns.

The PZT force field is based on the shell model and contains the Coulomb (eq. 3.2), Buckingham (eq. 3.1) and core-shell (eq. 3.3) interactions with a total of 28 parameters. To obtain the parameters for the force field I used a sequential approach, starting with a well tested parameter set for $PbTiO_3$ [84]. This force field reproduces PTO very accurately, including the tetragonal to cubic phase transition with temperature, lattice parameters, elastic constants and phonon frequencies. Taking this force field as an initial guess I used GULP [73] to fit the parameters to the *ab initio* results.

In a first step, the potential was fitted to $PbZrO_3$ structural data obtained from DFT calculations. Here, the parameters were optimised for the $Pm\bar{3}m$, *P4mm*, *Amm2*, *Pbam* space groups, leaving the Pb-O, O-O Buckingham and core-shell interactions from the previous force field unchanged. The Zr-O Buckingham parameters were then manually scanned on a grid search to find a set that gives the correct bond length and includes the rotations of the Zr-O octahedra in the *Amm2* and *Pbam* phases.

Table 4.1: Shell-model parameters for $Pb(Zr_{1-x}Ti_x)O_3$

short-range	A (eV)	ρ (Å)	C (eV^6)	
Pb - O	25223.874	0.229821	2.5658784	
Ti - O	1419.0969	0.312696	32.849274	
Zr - O	1479.9957	0.327618	39.359589	
O - O	13728.834	0.241404	100.71785	
species	$q_c(e)$	$q_s(e)$	k_2 (eV^{-2})	k_4 (eV^{-4})
Pb	11.697324	-10.223899	274.07860	1023162.3
Zr	11.228644	-8.279064	43803.694	127868.48
Ti	7.996850	-5.047270	36926.634	132998.80
O	2.466594	-3.940929	221.30147	67027.923

As a final step the two force fields were merged and reparametrised for the following phases: *P4mm* $PbTiO_3$, *Pm$\bar{3}$m* $PbTiO_3$, *Pm$\bar{3}$m* $PbZrO_3$, *R3c* $PbZrO_3$, *Pbam* $PbZrO_3$, *P4mm* $PbZr_{0.5}Ti_{0.5}O_3$. Here, all force field parameters were fitted to DFT structural data including atomic positions and lattice parameters. The ordered PZT tetragonal *P4mm* $Pb(Zr_{0.5}Ti_{0.5})O_3$ phase is the WC DFT ground state and was chosen as a representative phase at the 50/50 solid solution. To include relevant piezoelectric properties, the force field was also fitted to elastic constants [84], Born effective charges [89] and piezoelectric coefficients [89]. Additionally, energy differences between tetragonal and cubic phases for PTO and PZO were used as observables in order to match their Curie temperatures (T_c) [90].

4.1.1 Potential Problems in Fitting of Shell Model Force Fields

As mentioned in section 3.2.3, the fitting of a force field is generally not a straight forward procedure. Adding core-shell interaction further complicates the process, since the shell positions are not specified from either *ab initio* or empirical data. It is only the core positions, which are equal to the nuclei positions, that can be inferred directly from the observables. This issue can be overcome by simultaneously relaxing the shell during the fitting, which is implemented in GULP. In this approach, the shell forces are treated as observables, while the shell positions are then variables to be optimised. Although the core-shell parameters can be fitted to DFT data such as structure and Born-effective charges, the results can often

be poor.

In the case of developing a potential for PZT this meant that the k_2 and the k_4 terms of the core-shell interactions would get extremely large or nearly zero. These extreme values would occur even when all the observables are reproduced well. However, testing the fitted potential in geometry optimisations or MD simulation quickly reveals the main issue with extreme k values: large core-shell separations that will abort the simulation. This means the core-shell interactions are not stable and the shells are easily stripped of their cores, separating several Angstroms or more. GULP and DL_POLY_4 report these large, erroneous core-shell displacements and usually terminate. Paying extra attention to the core-shell parameters is therefore necessary in fitting a shell model potential.

However, even if a force field seems to behave well during testing, core-shell separation issues are common for the shell-models in ferroelectrics and will appear occasionally, mostly at higher temperatures. One way to prevent such errors that can abort a whole simulation, is to keep the core-shell from separating too far. This can be done by modifying the core-shell interaction as proposed by Chen et al. [91]. Here, the k_2 term includes a distance (r_{ij}) dependent 5th order term, $k_2 = 0.99 + 1000r_{ij}^5$, which restores the shell to its core for large separations. This core-shell interaction modification was only made for the MD simulations once a satisfactory force field was already obtained. For the obtained PZT force field I added this extra term to the core-shell interaction in DL_POLY_4, which helps to stabilise high temperature simulations. Note, when setting up simulations cells far from equilibrium positions, the core-separations errors still occur regularly.

All other parameters in the shell model force field are less sensitive and can be optimised straightforwardly. Nevertheless, thorough testing in supercell geometry optimisations or ideally with MD simulations is needed, even if the initial fitting results report great agreement with the observables.

4.2 Characterisation of the $Pb(Zr_{1-x}Ti_x)O_3$ Force Field

4.2.1 Structural Properties

In the previous section I successfully developed a shell model force field for PZT. To gauge how well it performs, the force field was characterised through geometry optimisation and with MD simulations for different compositions and temperatures.

The obtained force field reproduces the structural parameters of both end materials of the PZT phase diagram, PZO and PTO, very well. A comparison of structural parameters

Table 4.2: Structural parameters for different phases of PTO, PZO and PZT reproduced by *ab initio* calculations and the developed force field. For PTO and PZO the energy difference (ΔE) to the ground state (*P4mm* for PTO and *Pbam* for PZO) is reported.

	PTO				**PZO**				**PZT**	
	P4mm		*Pm$\bar{3}$m*		*Pbam*		*Pm$\bar{3}$m*		*P4mm*	
	DFT	FF	DFT	FF	DFT	FF	DFT	FF	DFT	FF
a (Å)	3.852	3.884	3.920	3.937	5.941	5.850	4.139	4.122	5.627	5.617
b (Å)	3.852	3.884	3.920	3.937	11.802	11.766	4.139	4.122	5.627	5.617
c (Å)	4.041	4.102	3.920	3.937	8.256	8.167	4.139	4.122	4.261	4.210
V (Å^3)	59.9	61.9	60.2	61.1	578.9	562.2	70.9	70.1	134.9	132.9
ΔE (meV)	0	0	78.8	96.6	0	0	62.6	71.5	-	-

for different phases of PTO, PZO and PZT obtained with the force field is shown in table 4.2. In particular, the force field reproduces the cubic phase of both PTO and PZO in a very good agreement with the DFT calculations. The difference in the lattice parameters, compared to DFT, is within 0.4%. Although the tetragonal phase of PTO shows a slightly increased tetragonality ratio compared to DFT results, the errors for the a and c lattice parameters are only 0.8% and 1.5%, respectively. The antiferroelectric *Pbam* phase of PZO is in good agreement with DFT with errors on a, b and c of 1.5%, -0.3% and -1.1%. The force field also reproduces the structure of the *P*4*mm* phase of PZT in very good agreement with DFT values. Here, errors on a and c are -0.2% and 1.2%, respectively. For both, PTO and PZO the cubic *Pm$\bar{3}$m* phase is the highest energy phase. The energy difference (ΔE) between the high temperature cubic phase and the tetragonal ground state in PTO is 96.6 meV and 71.5 meV between the cubic PZO phase and the orthorhombic ground state of PZO. Both energy differences slightly overestimate their respective DFT values. The ferroelectric displacements of ions in ordered PZT agree well with DFT. However, the Born effective charges are underestimated. The latter leads to underestimated values of polarisation of 43.08 $\mu C/cm^2$ obtained with the force field, compared to 81.00 $\mu C/cm^2$ calculated from by Wu et al. [89].

4.2.2 Potential Well of the Polar Mode in *P4mm* $Pb(Zr_{0.5}Ti_{0.5})O_3$

The force field reproduces the double well potential of *P4mm* PZT, as shown in Fig. 4.3, which describes the difference in energy of the system against the polar mode. For zero

Table 4.3: Comparison of calculated Born-effective charges and elastic constants with DFT and force field (FF) for $Pb(Zr_{1-x}Ti_x)O_3$.

Born effective charges			elastic constants		
	DFT[89]	FF		EXP[92]	FF
$Z^*(Pb)$	3.46	3.42	c_{11}	198.4	263.19
$Z^*(Zr)$	5.95	3.42	c_{12}	87.1	63.90
$Z^*(Ti)$	5.99	3.23	c_{13}	92.5	90.37
$Z^*(O)$	-4.28	-2.04	c_{33}	162.4	125.89
P_Z (μ C/cm^2)	81.00	43.08	c_{44}	47.4	57.76
			e_{66}	55.4	48.50

amplitude of the polar mode, PZT is in its centrosymmetric state with zero polarisation. Displacing the atoms along the polar Γ phonon mode lowers the total energy, until the PZT is in its ferroelectric *P4mm* ground state. Such a double well potential is characteristic for all ferroelectrics and can be calculated for PZT from DFT and the force field (Fig. 4.3). Clearly, the energy lowering is symmetric for positive and negative Γ displacements, leading to positive and negative polarisation.

The calculated energy lowering is 31% smaller for the force field (211 meV) compared to the DFT (308 meV) results. Since GGA functionals overestimate the tetragonality and polarisation in ferroelectrics, the calculated DFT values are likely to show a too large energy lowering. Indeed, LDA calculations showed a much flatter double well for PZT, with a well depth of 175 meV [93]. Thus, the predicted energy lowering by the force field reproduces PZT *P4mm* very well, considering that the values lie in-between the LDA and GGA results. From the energy difference the forces can be calculated as the derivative of the energy with respect to the displacement. The forces show the same underestimation of the GGA results as the energy, yet seem to be physically sensible for the same arguments as above. Having reasonable forces allows the force field to be employed in MD simulations. Additionally, the force field is expected to behave well under externally applied fields.

4.2.3 Temperature Induced Phase Transition

The temperature dependent properties (cell parameters, cell angles and polarisation) have been calculated with MD simulations in a 12x12x12 unit cell periodic box containing 8640

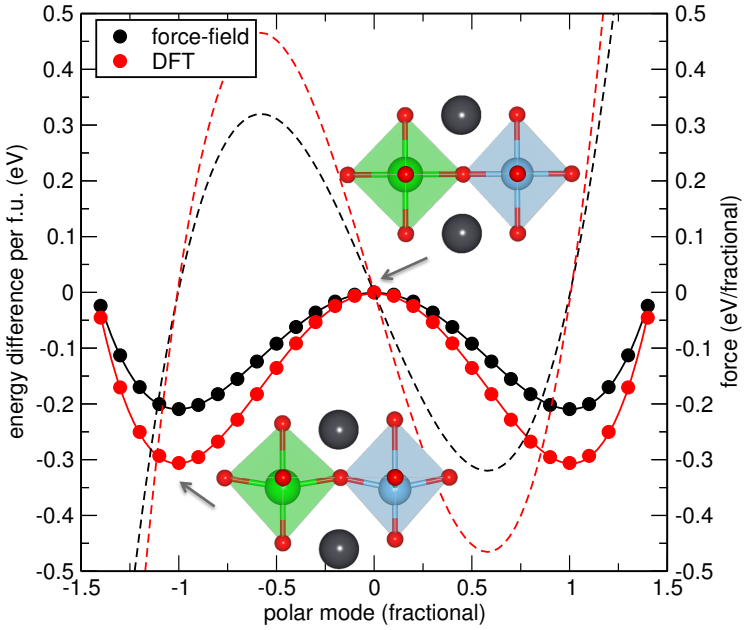

Figure 4.3: Energy (solid line) and derived forces (dashed line) of the polar mode of *P4mm* $Pb(Zr_{0.5}Ti_{0.5})O_3$ calculated from the force field and from DFT. The insets show the centrosymmetric state (top) and the structure with the fully condensed mode (bottom). The force field underestimates the forces by 31%.

atoms. In the disordered systems (10% - 90% Ti) the B-cations are randomly distributed over all possible B-cation positions. I used an NST ensemble with Nosé-Hoover thermostat (0.01 ps) and barostat (0.1 ps) to allow for phase changes and relaxations of the simulation box. The temperature was subsequently raised in 20 K steps and at each temperature the system was equilibrated for 4 ps followed by 6 ps production with a timestep of 0.2 fs.

The derived force field successfully reproduces the temperature induced phase transition from low symmetry to paraelectric phase in PZO, PTO and PZT. The temperature dependence of the lattice parameters of PZO is shown in Fig. 4.4a. At low temperatures the PZO systems adopts a structure with $a = b > c$ and $\alpha = \beta = 90^\circ$ while $\gamma > 90^\circ$. The system exhibits a clear phase transition at around 420 K, where the cell parameters equalize, resulting in the high temperature cubic phase. As seen in the inset of Fig. 4.4a the lattice angles are 90° above the transition temperature. The force field dynamically reproduces the low temperature antiferroelectric phase of PZO and phase transition to the paraelectric cubic phase at T_C=420 K.

At low temperatures PTO exhibits tetragonal symmetry with cell parameters satisfying $a = b < c$. The tetragonality ratio, a/c, decreases with raising temperature and at around

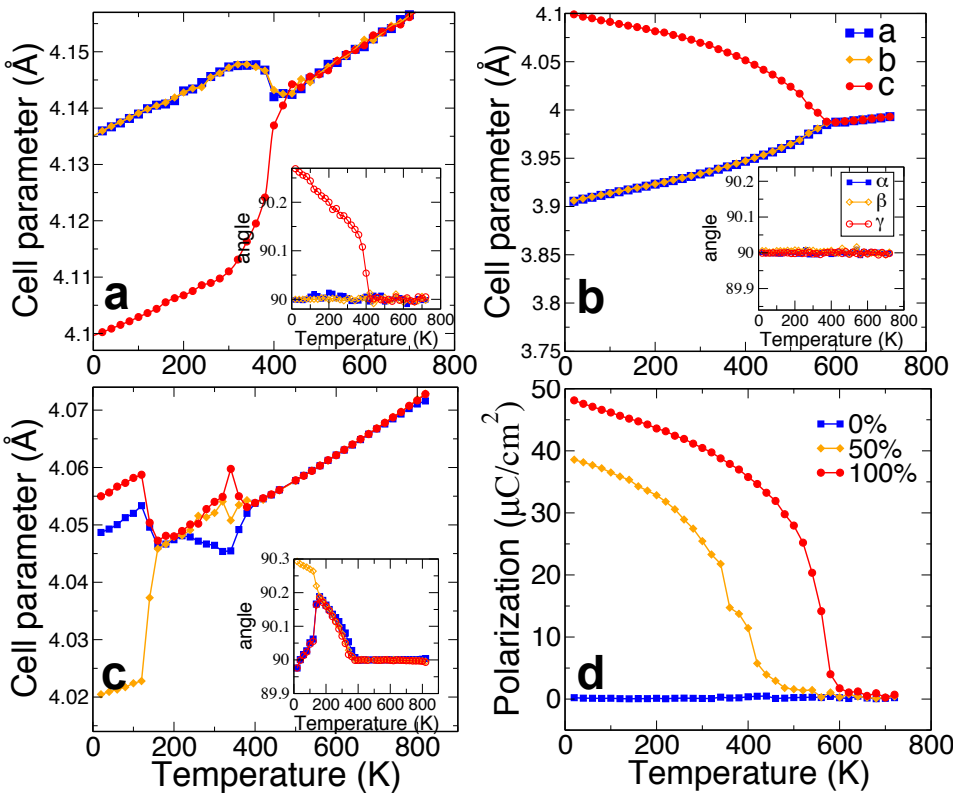

Figure 4.4: Temperature dependence of lattice parameters of (a) PZO, (b) PTO, (c) r-PZT and (d) the magnitude of polarisation for those compounds.

600 K a phase transition to the cubic phase occurs (Fig. 4.4b). The cell angles strictly stay 90° over the whole temperature range. The force field therefore dynamically reproduces the tetragonal and cubic phases of PTO with the T_C of 600 K.

Modelling of the thermal behaviour of lattice parameters for the ordered phase of PZT gives a very high estimate of the Curie temperature (T_C). Due to limitations of the core-shell model parametrisation the MD simulations became unstable above 1300 K, thus I was unable to find T_C for this phase (for more details see section 4.2.4). Introducing B-cation disorder brings the system out of its very stable, highly polar *P*4*mm* state and produces a phase transition to the paraelectric state at 420 K, about 200 K lower than experiments [94].

Further, the force field was applied to model the properties of PZT with random distribution of B-cations. Henceforth, I will denote the ordered *P*4*mm* phase of $Pb(Zr_{0.5}Ti_{0.5})O_3$ as o-PZT, while the system with random distribution of B-cations as r-PZT for the remainder of this chapter. I have found that r-PZT adopts monoclinic symmetry at low temperatures with $a \neq b \neq c$ and $\alpha = \gamma < \beta$. Simulated annealing induces a complex change of lattice

parameters with increasing temperature (see Fig. 4.4c). At about 200 K the system becomes rhombohedral $a = b = c$ and $\alpha = \beta = \gamma \neq 90^\circ$ and then adopts a tetragonal symmetry with $b = c > a$ and $\alpha = \beta = \gamma = 90^\circ$ at around 400 K. Due to introduced B-cation disorder, the rhombohedral to tetragonal transition is smoothed [95]. At 420 K the system undergoes a clear transition from tetragonal to the paraelectric cubic phase (Fig. 4.4d). The temperature dependence of polarisation for r-PZT is shown in Fig. 4.4d. One can see that the low temperature phase develops polarisation along [111] of 39 μC/cm^2, which is lower than that of o-PZT (43 μC/cm^2). With increasing temperature the polarisation decreases, and at 350 K where the system develops another phase, the magnitude of polarisation drops to 15 μC/cm^2. Finally, at 420 K the polarisation disappears which is indicative of a the transition to the paraelectric, cubic, phase. Remarkably, introducing randomness in the Ti and Zr cation ordering leads to the formation of monoclinic and rhombohedral phases.

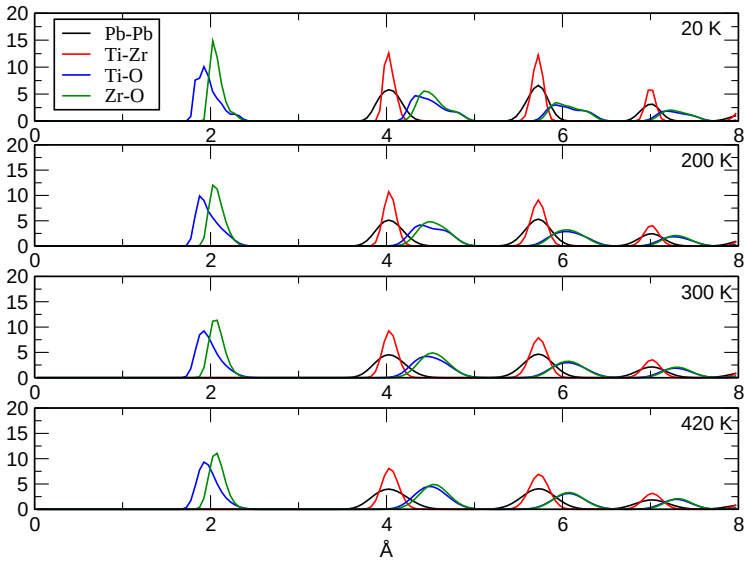

Figure 4.5: Radial distribution functions (RDF) for Pb-Pb, Zr-Ti, Ti-O and Zr-O ion pairs in random PZT at different temperatures.

Radial distribution functions (RDF) for r-PZT have been calculated in a 40x40x40 supercell (NST ensemble, Nosé-Hoover thermostat) at different temperatures (see Fig. 4.5). At 20 K the Ti-O and Zr-O peaks are asymmetric and the Ti-O peaks consists of several subpeaks which demonstrate the presence of different Ti-O bond lengths in the monoclinic phase. With increasing temperature all the peaks broaden and there is no shift or change in the Pb-Pb peaks. This means the Pb sublattice is unchanged through the several phase transitions while most differences are visible in the Ti-O. This suggests that at the MPB the

Ti ions (or Ti-O octahedra) mediate the subtle phase transitions with temperature.

4.2.4 High Temperature Stability of Ordered *P4mm* $Pb(Zr_{0.5}Ti_{0.5})O_3$

The previous section reported the phase transition with temperature from the ferroelectric to the paraelectric cubic phase across the whole composition of PZT. Interestingly, I found that $Pb(Zr_{0.5}Ti_{0.5})O_3$ in its *P4mm* space group does not show a cubic phase in the tested temperature range up to 1300 K. This is seen in Fig. 4.6, which shows the cell parameters of ordered *P4mm* $Pb(Zr_{0.5}Ti_{0.5})O_3$. Although there seems to be a phase transition at around 600 K, where the slopes of the cell parameters change, the cell parameters do not equalize for any given temperature. Therefore, no cubic phase and no ferroelectric to paraelectric phase transition occurs in the reported temperature range. Attempts to perform MD simulations at higher temperatures failed due to core-shell separation errors (see section 4.1.1). As a result, 1300 K marks the highest usable temperature for the PZT force field in NST simulations. Since this is at least twice as high as T_C for most of the solid solution, this temperature limit should not be an issue when simulating ferroelectric PZT or the phase transition.

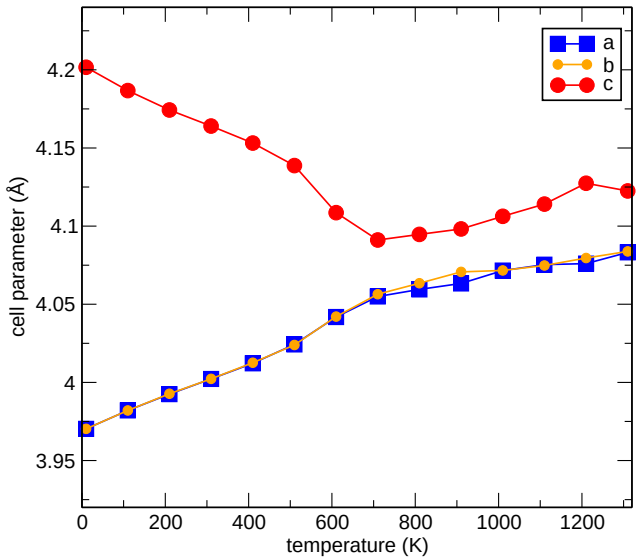

Figure 4.6: Cell parameters with temperature for *P4mm* $Pb(Zr_{0.5}Ti_{0.5})O_3$. No cubic phase is observed up to 1300 K for this configuration of PZT.

On the other hand, the inherent stability of ordered *P4mm* $Pb(Zr_{0.5}Ti_{0.5})O_3$ might reduce the usability of the force field to study chemically ordered structures and their phase transitions. The origin of this extraordinary stability lies in the fitting to the *P4mm* $Pb(Zr_{0.5}Ti_{0.5})O_3$ DFT structure. A WC (GGA) parametrisation was used which knowingly

overestimates the tetragonality and polarisation of ferroelectrics [96]. This large tetragonality probably had the effect of over stabilising the ferroelectric structure compared to the paraelectric one. In order to treat PZT realistically, e.g. as a disordered solid solution, a random distribution of the B-cation is advised which also avoids the problem of the stability of the peculiar *P4mm* ordered phase.

4.2.5 Composition Induced Phase Transition

Remarkably, besides the temperature induced phase transitions the force field also reproduces the composition driven phase transition of $Pb(Zr_{1-x}Ti_x)O_3$. Indeed, the increase of Ti content, x, induces a phase change from rhombohedral to tetragonal symmetry mediated by a monoclinic phase that agrees well with the experimental phase diagram of PZT [35, 94].

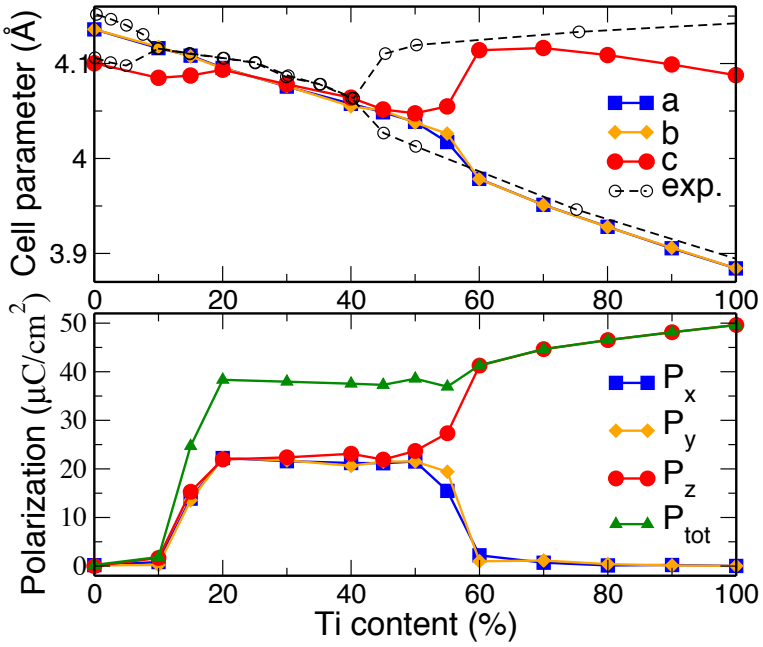

Figure 4.7: (top) The dependence of lattice parameters on the Ti content (blue, orange, red symbols corresponds to a, b and c lattice parameters, while black dotted line is experimental data by Shirane [9]). (bottom) The dependence of polarisation of r-PZT on the Ti content (Blue, orange, red and green symbols are x, y, z components and the magnitude of polarisation, respectively).

I have found that changing the Ti content (x) induces the variation of the averaged lattice parameters of the 12x12x12 unit cell system as seen in Fig. 4.7a. Indeed, at $x < 20\%$ the system exhibits $a = b \neq c$, then within $20\% < x < 45\%$ lattice parameters equalise $a = b = c$. At $x > 60\%$ the system stays with $a{=}b < c$ with all angles equal to 90 °. The system

exhibits monoclinic symmetry at low Ti content $x < 20\%$ (Fig. 4.7 top, where the large Zr content stabilises the antiferroelectric phase, so overall magnitude of polarisation of the system is zero (Fig. 4.7 bottom. Further increase of x up to 20% stabilises the ferroelectric phase with the gradual increase of all components of polarisation so the system maintains [111] polarisation that reaches the value of 38 μC/cm^2 at x=20%. Increase of the Ti content from 20% to 45% induces the system to adopt rhombohedral symmetry. The polarisation is oriented along [111] direction and stays at a constant value of around 40 μC/cm^2 within the range of x=20-45%. The interval of compositions with Ti content varying from 45% to 60% can be denoted as the MPB region, where the system is monoclinic at low temperatures and accompanied with a gradual increase of c-component of polarisation. The vector of polarisation increases its c-component and decreases the other components. Finally, at $x >$ 60% the polarisation direction is fully oriented along [001] and the magnitude increases with x until it reaches values of 49 $\mu C/cm^2$, characteristic of pure PTO. The system maintains the tetragonal state at $x > 60\%$, which suggests that the potential overestimates the width of the MPB region in comparison to experimental data (48-52%).

4.2.6 Domain Walls Energies for $Pb(Zr_{0.5}Ti_{0.5})O_3$

Domain walls play an important role in ferroelectrics and the developed PZT force field should represent them correctly. Therefore, the domain wall energies in PZT were compared between the force field and DFT results. Two kinds of domain walls were studied in PZT *P4mm*: Lead centered 180° and head-to-tail 90° domain walls, since DFT studies [84] for PTO show that lead centered domain walls are more stable than Ti centred. These configurations are shown in Fig 4.8 for PZT. In order to find their relative stability the domain wall energy has been calculated in the following way: $E_{DW} = (E_{domain} - E_{bulk})/A$. Here, E_{bulk} is the energy of the reference bulk, monodomain system and E_{domain} is the energy of the system with domain wall. The whole energy is normalised by the domain wall area (A).

The CP2K package [76] was used to study the stability of domain walls in PZT from DFT. Since CP2K had no k-point sampling at the time this thesis was written, gamma point calculations in supercells of 6xNx6 ($N = 6, 8, 10, 12$) were performed. An energy cut-off of 600 Ry and a relative cut-off of 60 Ry were used together with the PBEsol [97] parameterisation, PBE-GTH pseudopotentials [98] and MOLOPT [99] basis sets. CP2K was used in this case over the previously utilised CASTEP code since domain wall calculations in PZT

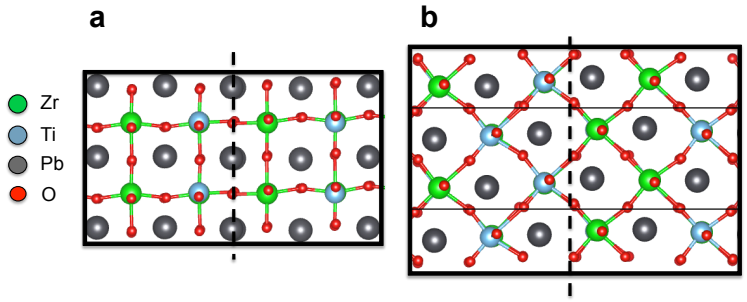

Figure 4.8: Schematic lead centred a) 180° and b) 90° head-to-tail domain walls in PZT.

require large systems with over 100 atoms. For such system sizes a local basis set code performs better than a pure plane-wave code. A comparison with the previously used CASTEP code on lattice parameters and electronic structure has been performed. The calculated lattice parameters of PZT *P4mm* from the two codes do match very well. The differences are all within 1%. Additionally, the electronic density of states agrees very well too.

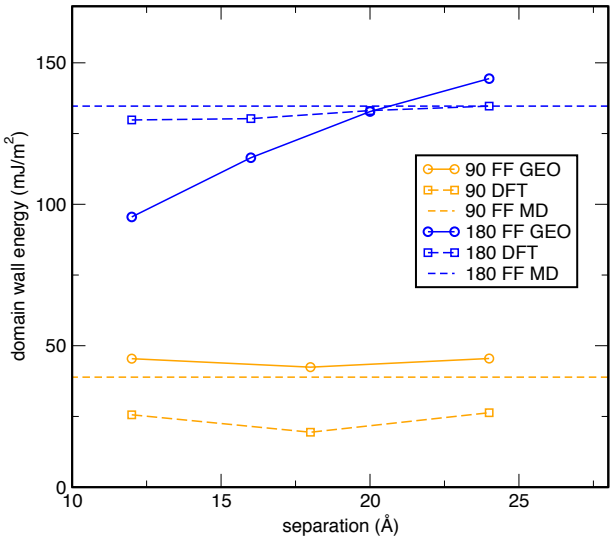

Figure 4.9: Energies for 180° and 90° domain walls in $Pb(Zr_{0.5}Ti_{0.5})O_3$ *P4mm*. FF GEO labels the geometry optimisation with the force field and FF MD denotes MD energies with the force field at 10 K. Note that the MD values correspond to very large separations of 115 Å for 90° and 630 Å for 180°. DFT energies were calculated with CP2K.

The domain wall energies were calculated in two different ways: for small systems full geometry optimisations were performed in GULP and in CP2K. These systems have a separation between the domain walls of 6, 8, 10 and 12 unit cells in the 180° case. The

energies of larger separations were calculated with low temperature MD at 10 K in an NPT ensemble. The domain wall energies with separation between the walls is shown in Fig. 4.9. Here the dashed lines correspond to the MD values at large separations of 115 Å for 90° and 630 Å for 180°.

For 180° the MD and DFT energies are very close and in very good correspondence to literature values of 132 mJ/m^2 for PTO calculated by DFT (LDA) [100]. Another DFT (LDA) study [93] reports a domain wall energy in PZT of about 160 mJ/m^2 for a Zr centred domain wall and of about 330 mJ/m^2 for a Ti centred wall in a (100) PZT superlattice. The force field values obtained by geometry optimisation show a strong dependence on domain size. This is probably due to convergence problems for large systems during the geometry optimisation. On the other hand, the DFT values are very stable with increasing separation.

The agreement between calculated domain wall energies for 90° is less good, 43 mJ/m^2 for the force field and 26 mJ/m^2 for DFT and differ much more. Again the DFT results are comparable to literature DFT (LDA) values [101] for PTO of 29 mJ/m^2. As for the PTO case [84] the 90° domain walls are about 5 times more stable than the 180° domain walls.

The DFT and force field values are in good agreement for 180° domain walls. For 90° domain walls the force field overestimates the domain wall energies almost by a factor of two. This might be a limitation in the shell-model, since Shimada [84] et al. show a similar overestimation of 90° domain wall energies in their PTO force field. Also, the structure of the PZT supercell seems to influence domain wall energies drastically, since this defines which atoms (species) are placed at the domain wall. The relative difference in stability of the two domain walls is, however, consistent with the literature and this will allow us to use the force field two study those types of domain walls in more realistic systems.

4.3 Application 1: Biaxial Strain

To put the PZT force field into use, I investigated the effect of strain on bulk r-PZT with and without domain walls. MD simulations were performed in an NPAT ensemble that keeps a and b cell parameters fixed but relaxes the c direction. First, annealing of the individual systems was done in 50 K steps from 10 K to 310 K under NST (Berendsen thermostat) for 4 ps each. After that, equilibration at 310 K under NST (Nosé-Hoover thermostat) took place for 8 ps. Then the cell parameters along a and b were equally stretched or compressed by a relative amount. This effectively induces strain in the ab-plane. However, the system is kept in the NPAT ensemble for 8 ps and is therefore able to relax along c, reducing overall stress.

The systems were strained from -5% to +5%, whereas negative (-) denotes compressive strain and positive (+) denotes tensile strain.

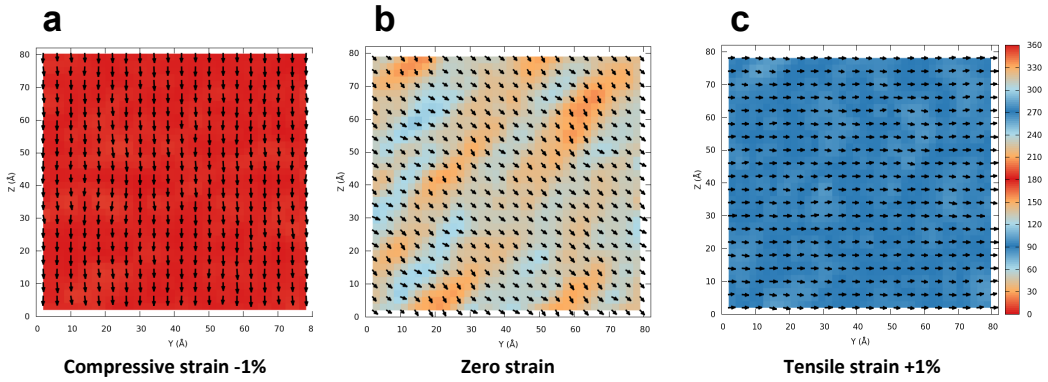

Figure 4.10: Polarisation profile of r-PZT Bulk systems under biaxial strain shown in the yz plane. Black arrows correspond to the polarisation direction and magnitude in each unit cell (averaged along x). Colour represents angle of the polarisation vector. (a) -1% compressive strain, (b) zero strain, (c) +1% tensile strain.

The unstrained bulk system breaks up into weak domains as seen in Fig. 4.10b. The overall direction of polarisation is along [111]. Applying compressive biaxial strain rotates the polarisation smoothly along [001]. On the other hand, tensile strain will rotate the polarisation along [110]. Fig. 4.10c shows all the dipoles aligning along y, but there is an equal polarisation contribution along x, making the overall polarisation direction [110], thus complying with the biaxial strain condition. The polarisation in this system is shown in Fig. 4.12a and demonstrates the same three regions pictured in Fig. 4.10. For compressive strains the polarisation is strictly along z. Between -0.5% and +0.5% the polarisation is along the unstrained r-PZT direction eg. [111]. Then for tensile strain the polarisation rotates into the xy-plane. There is a linear increase with polarisation in both strain regimes, once the polarisation states are fully adopted. The configurational energy in Fig. 4.11a also shows the two regions with a transition zone from -1% to +0.5%. In the monodomain states the configurational energy has a quadratic dependence on strain.

For 180° domain walls the configurational energy (see Fig. 4.11b) again shows two regions with a crossover at 1% tensile strain. With tensile strain the domain wall broadens, lowering the configurational energy. After the crossover, the system develops its polarisation along y ([010]) while still maintaining a very broad domain wall. Only for large tensile strains of over +3% the domain wall vanishes and the system polarises along [110]. Under

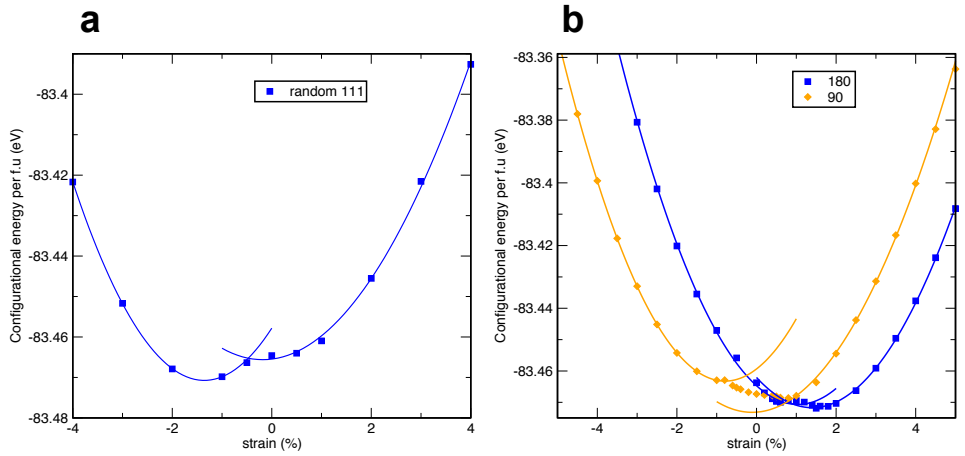

Figure 4.11: Configurational energy of bulk $PbZr_{0.5}Ti_{0.5}O_3$ in different structures with biaxial strain. (a) r-PZT (b) 180° and 90° domain walls.

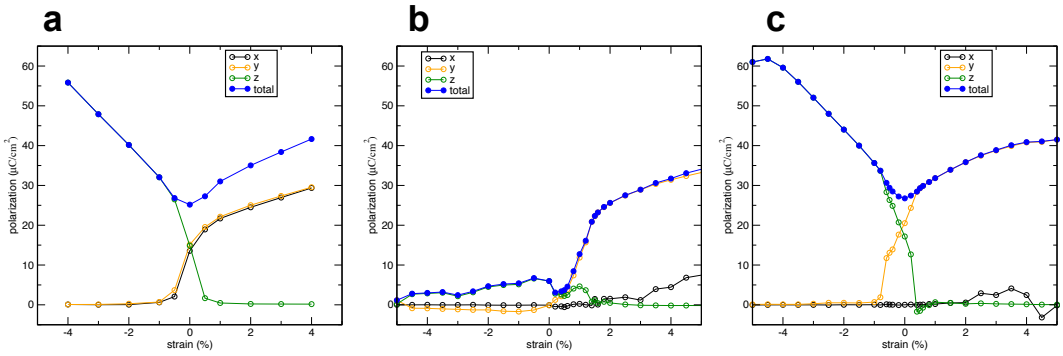

Figure 4.12: Polarisation of the (a) r-PZT bulk, (b) 180 °, (c) 90° systems under strain.

compressive strain the domain wall narrows but stays intact even for large strains of up to -5%. Images of the strained 180° domain walls can bee seen in Fig. 4.13. Regarding the polarisation (see Fig. 4.12b), it can be seen that the polarisation along y develops (rotates) between +0.5% and +1.7%. After +3% strain the polarisation rotates slowly into the xy plane, similar to the bulk system. For compressive strains the total polarisation is close to zero since the two opposed 180° domains cancel each other.

For 90° domain walls the zero strain state consists of domains polarised along y and domains polarised along z as shown in Fig. 4.14b. Compressive strain favours the domains polarised along z ([001]), which then grow at the expense of the perpendicular domains until a monodomain state is reached. This [001] monodomain is fully developed at -1% compressive strain (see Fig. 4.14a). For tensile strain the [010] domains will grow until at 0.8% the whole system is polarised along y. Here, the polarisation is only along y and a

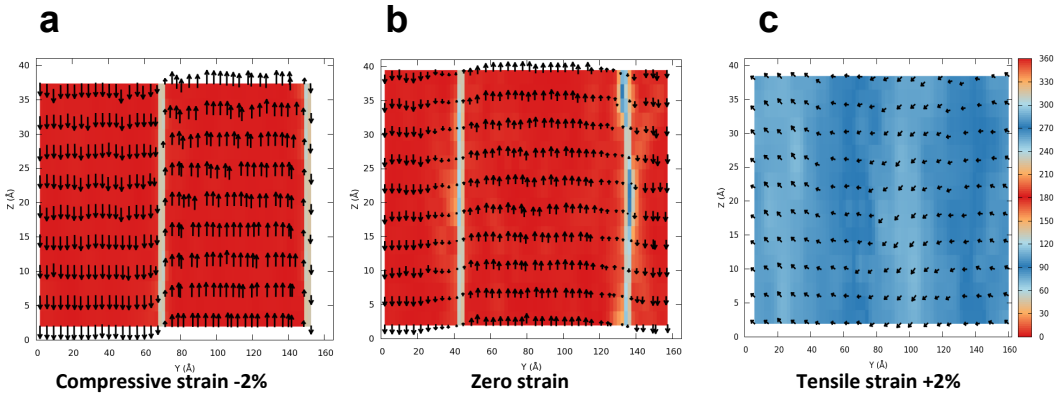

Figure 4.13: Polarisation profile of 180° domain walls under biaxial strain shown in the yz plane. Black arrows correspond to the polarisation direction and magnitude in each unit cell (averaged along x). Colour represents angle of the polarisation vector. (a) -2% compressive strain, (b) zero strain, (c) +2% tensile strain.

contribution along x does not build up below +2%. This difference to the bulk case, where polarisation is fully along [110] for large tensile strain, stems from the way the biaxial strain was applied. Relative strains were applied after the system was equilibrated. The bulk system is symmetric in the ab-plane, making relative strains along x and y equal. The 90° domain system on the other hand, has a domain wall that changes the dipoles in the yz plane but not along x. Therefore, a and b are not equal any more after equilibration, in fact b (along y) is larger because the domain walls are spread out. If now strain is applied by the same relative factor it will be larger along y than along x. This results in the polarisation being favoured along y. The energy plot (Fig. 4.11b) shows the two domain states with a transition corresponding to the multidomain state. Here, tensile strains lower the energy slightly. The polarisation plot (Fig. 4.12c) is similar to the bulk case. In the multidomain state (between -1% and 0.8%) the polarisation along y or z changes rapidly with applied strain.

In all the studied cases, there is a linear increase of polarisation with strain once a monodomain state is achieved. This strain polarisation coupling is larger in the compressive strain regime than in the tensile one. In the 90° domain system this coupling along certain directions is even larger in the multidomain state. If only specific polarisation directions are concerned such domain states could enhance the electromechanical properties of piezoelectrics. With large enough tensile strain 180° and 90° domain walls can be eliminated, changing not only the polarisation but also the energetics of the system. Unfortu-

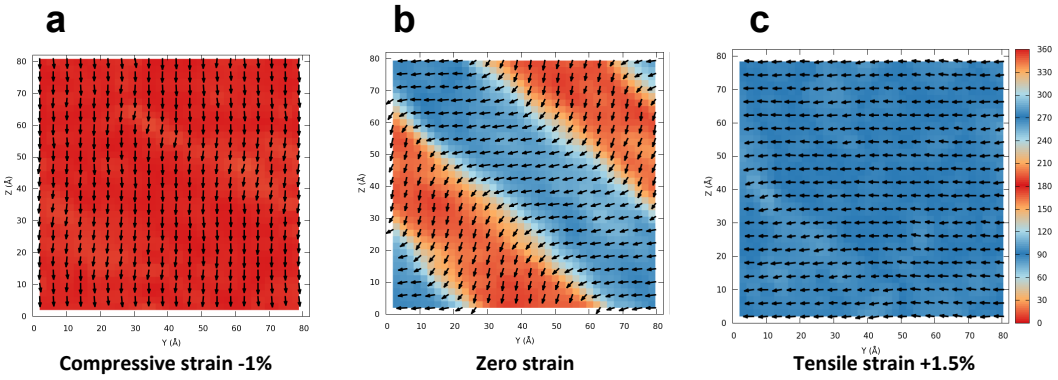

Figure 4.14: Polarisation profile of 90° domain walls under biaxial strain shown in the yz plane. Black arrows correspond to the polarisation direction and magnitude in each unit cell (averaged along x). Colour represents angle of the polarisation vector. (a) -1% compressive strain, (b) zero strain, (c) +1.5% tensile strain.

nately, strains of several % are usually too large to be realised in bulk ceramics, in thin films however this might be possible and could provide possible ways of domain engineering.

4.4 Application 2: Simulations of PZT Thin Films in Closed Circuit Conditions

In section 4.3 I showed how one can simulate domain patterns in PZT with the shell model force field. Such simulations are useful in studying the effect of strain or electric fields on the domains, but their size and the artificial set-up of the domain structure limits the comparison with a real material. In this section I show the applicability of the PZT force field to model domains in ultrathin PZT films under experimental closed circuit conditions. A transmission electron microscopy (TEM) image (see Fig. 4.15) of such a $Pb(Zr_{0.8}Ti_{0.2})O_3$ film was taken by our collaborators in the group of Martin Hytch at the Centre National de la Recherche Scientifique (CNRS) in Toulouse. The film was epitaxially grown on a $SrTiO_3$ (STO) substrate and covered with a top electrode of Pt. It clearly shows an a/c domain pattern, which is often found in ferroelectric thin films. Here, the 'a' domains are polarised in-plane (parallel to the substrate), while the 'c' domains are polarised out of plane (perpendicular to the substrate). The film is about 100 nm thick and the STO substrate was n-doped to make it a conductive electrode.

In order to accurately model a thin film in closed circuit conditions, the surface polarisation of the ferroelectric has to be screened. If this polarisation is not compensated, a

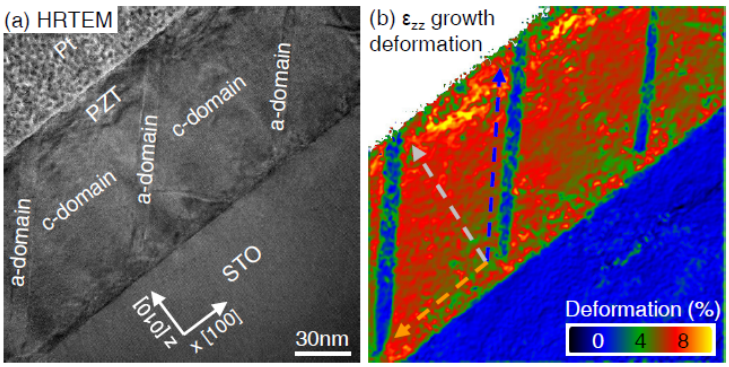

Figure 4.15: High Resolution Transmission Electron Microscopy (HRTEM) image of a $Pb(Zr_{0.8}Ti_{0.2})O_3$ thin film on $SrTiO_3$ (STO) with a top Pt electrode. The strain profile shows a clear a/c domain pattern with thin, needle-like 'a' domains.

ferroelectric slab with a surface will build up a depolarising field in its top layers so that the polarisation at the surface is zero. Alternatively, a ferroelectric slab could also build complex domain structures with vortices and closure domains to reduce its out of plane surface polarisation, as seen in work by J. Chapman which was recently submitted to Physical Chemistry Chemical Physics (PCCP). The sample shown in Fig. 4.15 has large 'a' domains ending at the Pt, where the metallic electrode screens the polarisation.

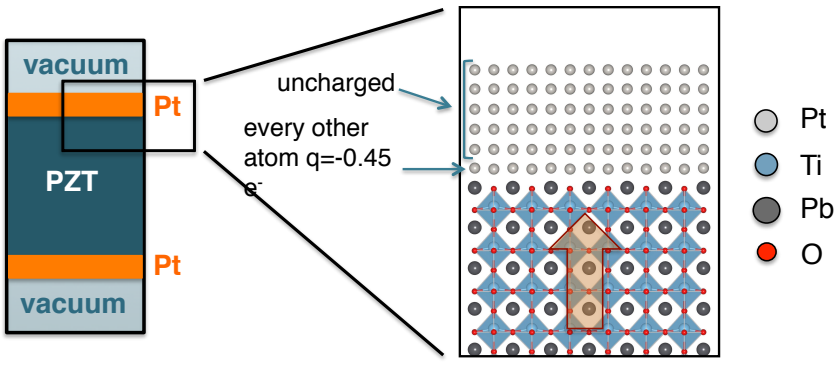

Figure 4.16: Schema of the Pt/PZT interface, which models the electrode and introduces screening in the ferroelectric bulk.

To model the screening at the PZT/electrode interface 6 Pt layers were used, which exactly cancelled the out of plane surface polarisation of PZT. Importantly, only the interfacial Pt layer carried a charge of $q = 0.45e$ on every other atom, while the remaining 5 atomic layers were uncharged. The charged Pt atoms are placed directly above the Pb ions and the charge was selected to be either positive or negative depending on the polarisation

of the PZT bulk. The value of the compensating charge on Pt was chosen to reproduce the bulk polarisation in PTO in all layers, so that no depolarising field occurred. For the Pt-Pt interaction a classical Finnis-Sinclair type metal potential [102] was used, that accurately describes bulk fcc Pt. To bond the Pt layer to the PZT I used a simple quadratic potential between the Pb and Pt atoms.

Further, the STO substrate was modelled with a cubic STO shell model force field which is compatible with the PZT force field. The coordinates of the first 4 unit cell layers of STO were kept fixed to model the clamping by the substrate, while 4 additional layers were allowed to relax. On top of these 8 unit cell layers of STO 90 layers of PZT were added with 6 atomic layers of Pt as the top electrode. The supercell dimensions of the whole system amounted to $6\times160\times98$ perovskite unit cells (PZT+STO), corresponding to about 2.4 nm $\times$ 63 nm $\times$ 40 nm with about 478 000 atoms. This system is about half the size of the 100 nm thick experimental sample and should therefore show a comparable domain pattern. For the surface termination I used a vacuum layer of 10 nm between the Pt and the STO with 3D periodic boundary conditions (see Fig. 4.16). I then performed an MD simulation in an NVT ensemble with Nosé-Hoover thermostat (0.01 ps) where the a and b cell vectors were fixed to match the STO lattice parameters (a=3.905 Å). The $Pb(Zr_{0.8}Ti_{0.2})O_3$ system was originally set up with two 'a' domains and then equilibrated at 300 K for 50 ps, followed by production of 200 ps. Interestingly, this large scale system took a very long time (about 150 ps) to relax and form a stable, non-moving domain pattern.

The domain pattern in the yz-plane averaged over the last 20 ps of the production run is shown in Fig. 4.17. Two 'a' domains (blue) are clearly visible in a background of 'c' domains (red). The 'a' domains emerge from the STO substrate and narrow through the film, where they terminate near the surface. Generally, the simulated domain pattern is very similar to the TEM image in Fig. 4.15, with both images showing angled 'a' domains. However, the 'a' domains in the simulated PZT are less angled than the experimental domains. Furthermore, during the MD run the inner part of the domains polarised slightly along the c axis, forming another small 'c' domain. This is probably an effect of the strain condition, which matches the experimental set up, but might have a slightly different manifestation in the force field simulation. Lastly, the simulated domains terminate near the Pt electrode, while the experimental ones terminate near the STO. This inversion is most likely due the approximate screening model applied in this simulation. The STO layer only screens as a

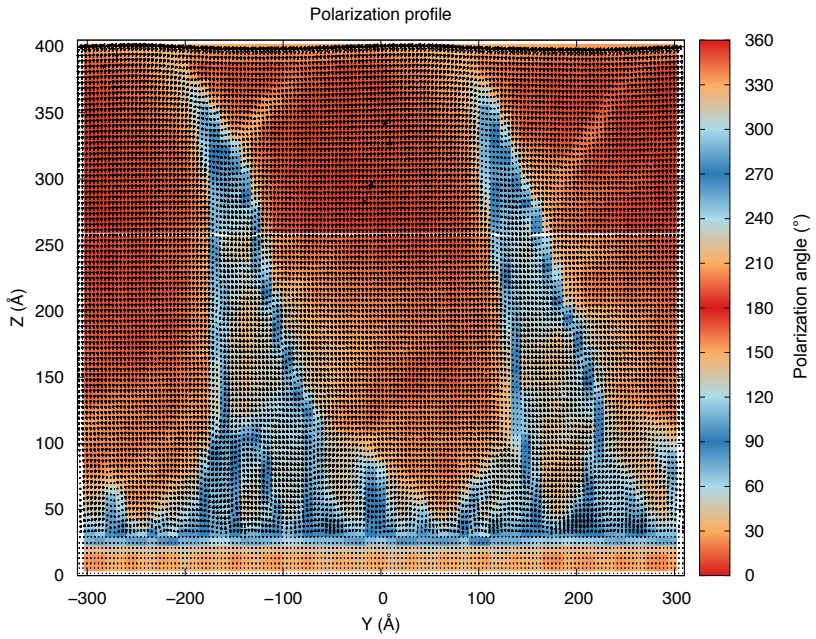

Figure 4.17: Domain structure of a $Pb(Zr_{0.8}Ti_{0.2})O_3$ thin film on $SrTiO_3$ (STO) with a top Pt electrode simulated with molecular dynamics. The large scale system with dimensions of about 2.4 nm $\times$ 63 nm $\times$ 40 nm shows an a/c domain pattern emerging from the substrate and terminating near the surface. The color denotes the angle of the polarisation (see color bar), where 'a' domains are blue and 'c' domains are red.

dielectric, while the Pt shows much better screening but has no actual metallic (electronic) properties. In the actual thin film both interfaces have metallic screening, although probably also imperfectly. The screening conditions of the model seemed to create the asymmetric domains seen in the thin film, but the interfaces had the exact opposite effect.

Nevertheless, I successfully ran a large scale MD simulation with experimental dimensions with the PZT force field. The polarisation screening of an actual PZT thin film was approximated, which lead to an a/c domain pattern which is very similar to the experimental results. Even though the strain and the screening conditions differ from the experiment, the produced domain structure is promising. Further improvements, especially on the Pt/PZT interface are needed in order to model a PZT ultra thin film in more detail.

4.5 Conclusions

In this chapter, I have developed a shell-model force field that incorporates the important features of PZT solid solutions, such as compositional and temperature induced phase transitions. The potential parameters were fitted to the results of *ab initio* calculations. The

force field reproduces the structural parameters and phase stability of both end members of PZT phase diagram (PZO and PTO) and the low energy *P4mm* phase of PZT with high accuracy. The force field supports temperature induced phase transitions from low symmetry (tetragonal) to the cubic phase, together with correct behaviour of polarisation. Remarkably, the force field also reproduces the details of the phase diagram of PZT with a good agreement to the experimental data [35, 9]. Indeed, with the increase of Ti content the system undergoes a sequence of phase transitions from rhombohedral to tetragonal symmetry, mediated by a monoclinic phase that is associated with the MPB.

Furthermore, the force field produces domain wall energies and atomic forces in good agreement with DFT results. I report that 90° domain walls are about 5 times more stable than the 180° in PZT which is in line with findings for PTO [84]. Besides domain walls, the potential also qualitatively replicates the potential well of the polar mode in *P4mm* $Pb(Zr_{0.5}Ti_{0.5})O_3$ obtained by DFT. These are important characteristics and allow the force field to be used in large scale MD simulations to study domain patterns and their dynamics in PZT.

In a first application, the potential was used to study $PbZr_{0.5}Ti_{0.5}O_3$ under biaxial strain, where I found a strong influence of the strain on the domain pattern. Most importantly, 90° domain walls enhance the strain polarisation coupling in PZT compared to a single domain state. Moreover, large tensile strains completely eliminate 180° and 90° domain walls, by enforcing a mono domain state in the materials.

In a second case study, I demonstrated the applicability of the force field to simulate the domain pattern in PZT ultrathin films by using large scale MD simulation containing close to 500,000 atoms. Although I only approximated the polarisation screening in the film, the simulated domain pattern showed a striking similarity to experimental domain structures. I conclude that the shell model force field reproduces the main characteristics of ferroelectric PZT and can be used to study the material in systems large enough to replicate experimental conditions.

Chapter 5

Ferroelectric Characteristics of $Pb(Zr_{1-x}Ti_x)O_3$ Under Applied Electric Fields

High performance piezoelectric materials such as PZT have been widely used in a variety of electrical applications, such as actuators, sensors or MEMS devices (for more details see section 2.6). The working principle of many of those applications is based on applying an electric field to the piezoelectric material in order to generate a mechanical response. It is, therefore, important to understand the effects of the electric field on the material, especially in a structurally challenging compound, such as PZT. Polarisation switching induced by varying electric fields has been previously studied in ferroelectrics [103, 104, 105, 106, 107], but here I use atomistic simulations to investigate PZT, which gives us a different angle than the experimental studies.

Ferroelectric properties can be studied with molecular dynamics (MD) by applying an electric field (E) to a simulation cell and calculating the polarisation of each unit cell from the atomic displacements [68, 108, 109, 71, 110]. Use of this method together with large scale calculations allows the modelling of bulk ferroelectrics and the evolution of their domain structure with time. Besides tracing the local polarisation, the macroscopic polarisation (P) of the material can also be calculated from spatial and temporal averages.

In this chapter this technique was used together with the force field developed in chapter 4, to investigate several different aspects of PZT's response to an external electric field. First, I analysed the change of the macroscopic polarisation and the change of the local atomic structure with static electric fields. In a second study the temperature dependent behaviour of the P-E loops of PZT has been explored. I especially considered the low tem-

perature regime, since PZT and other ferroelectrics have been used in aircraft, space and military engineering for decades [111, 112, 113], where they are used in low temperature conditions. Although many studies have been performed at room temperature and above, the low temperature (T<200K) properties of PZT are not well characterised. To overcome this, I employed MD simulations to calculate hysteresis (P-E) loops for a range of temperatures and noted the variation in the coercive field (E_C) and saturation polarisation with temperature. The calculated temperature variation of the coercive field displayed qualitatively similar behaviour to experimentally measured temperature variation.

The third part of the chapter analyses the dynamics of the polarisation reversal in more detail, where the effects of the temperature, B-cations, and electric fields on the switching speed are investigated independently. Here MD simulations were used to track the polarisation in real time as the sample repoled with an applied electric field.

5.1 Structure and Polarisation of PZT under Applied Electric Fields

In piezoelectrics the strain and the polarisation are strongly coupled so that an applied electric field will certainly induce a change in the material's structure. In this section I start quantifying the effects of the electric field by applying external fields to morphotropic PZT, where tetragonal, monoclinic and rhombohedral phases coexist [30], while monitoring the changes to the lattice and the symmetry.

5.1.1 Structure and Polarisation

For the MD simulations a $20 \times 20 \times 20$ supercell of $PbZr_{0.5}Ti_{0.5}O_3$ was used, which lies at the morphotropic composition of the modelled ferroelectric. The system contains 40'000 atoms and the two types of B-cations (Ti and Zr) were randomly distributed over the B-sites, so that the stoichiometry of $PbZr_{0.5}Ti_{0.5}O_3$ was ensured. The simulations were performed at 200 K which corresponds to room temperature in reduced units of the force field, which underestimates the Curie temperature of PZT (see section 4.2.3). A relatively small timestep of 0.2 fs was chosen and the shell particles were treated adiabatically. The Nosé-Hoover thermostat (0.01 ps) and barostat (0.1 ps) in the NST ensemble was used and the system was equilibrated for 20 ps, followed by 20 ps production for each value of the electric field. Uniform electric fields were applied with the external field option in DL_POLY_4, which adds a constant force to each particle. These calculation details were used for the whole chapter unless otherwise mentioned.

The MD simulations at zero field produce a rombohedral $PbZr_{0.5}Ti_{0.5}O_3$ phase with a polarisation (P) of 33.5 μC/cm^2 and equal lattice parameters ($a = b = c = 4.048$ Å). This zero field ground state was taken as the reference to calculate the strain (η) with applied field, as seen in Fig. 5.1a. The polar axis is along [111], as indicated by the equal amount of polarisation ($P_x = P_x = P_z$) in Fig. 5.1b. As an electric field is applied along the [111] direction, the strain and the polarisation components change depending on the field strength. For values up to 14 MV/m, η_z increases linearly while n_x and n_y decrease linearly, which is shown in Fig. 5.1a. At the critical field of 15 MV/m there is a jump in all strain components which further increases the η_z to η_x/η_y splitting. The lattice parameters of PZT at 15 MV/m are $a = b = 4.021$ Å and $c = 4.102$ Å, corresponding to a tetragonal symmetry. The behaviour of the polarisation follows the nature of the strain as shown in Fig. 5.1b. A linear increase of the P_z values together with a linear decrease of P_x and P_y is observed up to a field

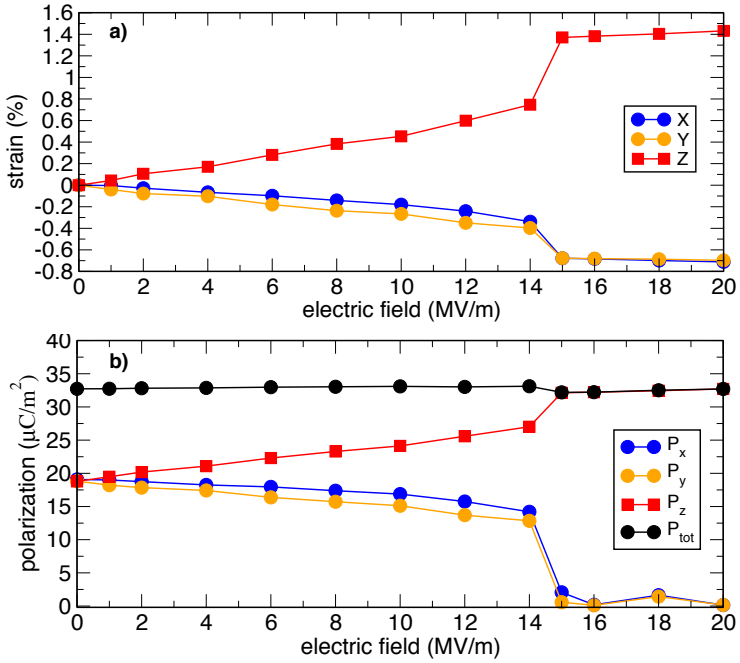

Figure 5.1: (a) Strain and (b) polarisation of $PbZr_{0.5}Ti_{0.5}O_3$ with applied electric field. For low fields the strain and the polarisation evolve linearly with the electric field. At 15 MV/m (critical field) there is a jump for both strain and polarisation due to the change in symmetry from rhombohedral to tetragonal.

of 14 MV/m, where the the values of the polarisation components are $P_z = 27.01\ \mu C/cm^2$, $P_x = 14.21\ \mu C/cm^2$ and $P_y = 12.85\ \mu C/cm^2$. As for the strain, the P values change discontinuously at 15 MV/m, with a further increase in P_z to $32.12\ \mu C/cm^2$, while P_x and P_y drop to almost zero. Over the whole range of electric fields the total polarisation (P_{tot}) stays almost constant, except at the critical field (15 MV/m) where P_{tot} decreases by about 1μ C/cm^2. The jump at 15 MV/m signifies the phase transition from rhombohedral to tetragonal with electric field in PZT. Below the critical value, the applied field induces a small amount of tetragonality as seen by the splitting of the η and P values. However, only above the critical field the system fully adopts the tetragonal phase, where the contributions of P_x and P_y vanish.

Further, the change in volume of the conventional unit cells V_{loc} defined by eq. 3.14 was analysed across the phase transition. Distinguishing between Zr and Ti based unit cells, I find that the Zr centred cells increase in volume by about 0.015 % while the Ti centred cells decrease by about 0.015 % from 14 MV/m to 15 MV/m as seen in Fig. 5.2b. This marks a difference in the response of the local environment of the two B-cations during the

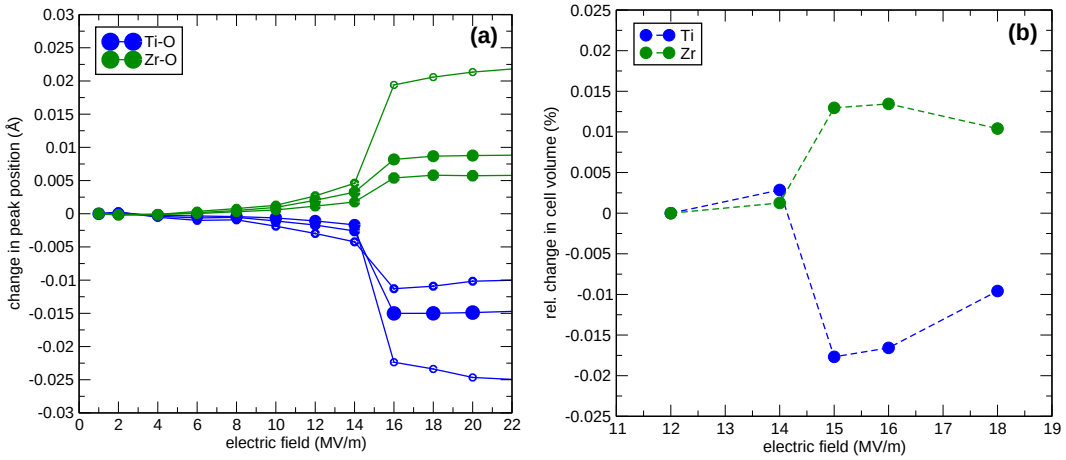

Figure 5.2: (a) Change of the RDF peak positions for Ti-O and Zr-O with electric field. The size of the circles corresponds to the height of the Gaussian function used two fit the peaks (3 Gaussians were used). The peaks shifts to longer bond lengths for Zr and smaller bond lengths for Ti at the phase transition at 14MV/m. (b) Change of the Ti (blue) and Zr (green) based unit cells with electric fields. At the phase transition at 14 MV/m the Ti based unit cells decrease in size, while the Zr based unit cells increase.

phase transition.

More details of the local structure and the bond lengths are obtained by analysing the radial distributions functions (RDF) for the Zr-O and the Zr-O pairs. The RDFs have been calculated for the different electric fields and the 2 Å B-O peaks were fitted with three Gaussian functions in order to accommodate a threefold peak splitting in the tetragonal symmetry. The change in the peak positions (Gaussians) relative to the zero field values are plotted in Fig. 5.2a. Here, I find that the Zr-O bond lengths increase, while the Ti-O decrease through the change of symmetry at 14 MV/m, which agrees with the volume change in Fig. 5.2b. Additionally, the jump in B-O bond lengths is accompanied by a splitting of the RDF peak, which is indicative of the transition to the tetragonal symmetry. Both, the V_{loc} and the B-O bond lengths are relatively unchanged above and below the phase transition. It is across the phase transition, however, where the Ti and Zr sublattices display opposite behaviour and where large changes in bond-lengths are seen. Overall, the macroscopic and the local parameters are relatively stable within a selected phase. Inducing a phase transition on the other hand, has a large effect on the bond lengths and strain, resulting in a large electromechanical coupling.

5.1.2 Polarisation Distribution

Plotting the distribution of P_z in Fig. 5.3, we see that the applied electric field shifts the distributions to larger values. This agrees with Fig. 5.3b where P_z increases, which is the average over the polarisation distribution. At the critical field, the polarisation distribution splits visibly into two subpeaks, meaning that in the tetragonal state there are two distinct contributions to P_z (see next paragraph). For electric fields above the critical field, I find only a small change in the distribution curves for P_z and no significant shift to higher values.

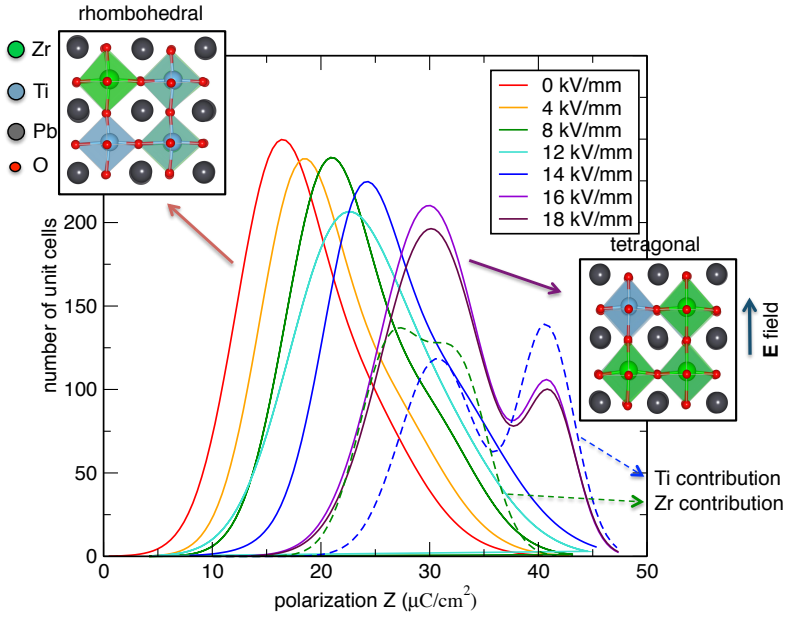

Figure 5.3: Distributions of the z component of the polarisation values (P_z) calculated for each B-cation centred unit cell for different electric fields (along [001]). Above a critical field (15 kV/mm) the polarisation distribution splits into two peaks, which is related to the change in symmetry from rhombohedral to tetragonal.

Fig. 5.4 shows the distribution P_z for zero field (rhombohedral) and 18 MV/m (tetragonal). The plots additionally show the contribution of the Zr based unit cells in green and the Ti based unit cells in blue. In both cases, zero field and 18 MV/m, the Ti based unit cells are more polarisable, as they solely cover the higher P_z values above 30 μC/cm^2 and 40 μC/cm^2, respectively. This agrees with earlier studies on PZT claiming that Ti is the ferroelectrically more active ion [30]. Moreover, I find that at zero field, the Zr contribution is much narrower and more Gaussian shaped than the Ti distribution. At 18 MV/m both, the Zr and the Ti P_z distribution splits into two subpeaks, with the separation being more pronounced for Ti. Here, the Ti peak at 32 μC/cm^2 overlaps largely with the Zr curve, while

there is a second peak at 42 μC/cm^2 only occupied by Ti. This explains the peak splitting of the total P_z distributions in Fig. 5.3, which is due to the Ti sublattice being separated into higher and lower polarised states.

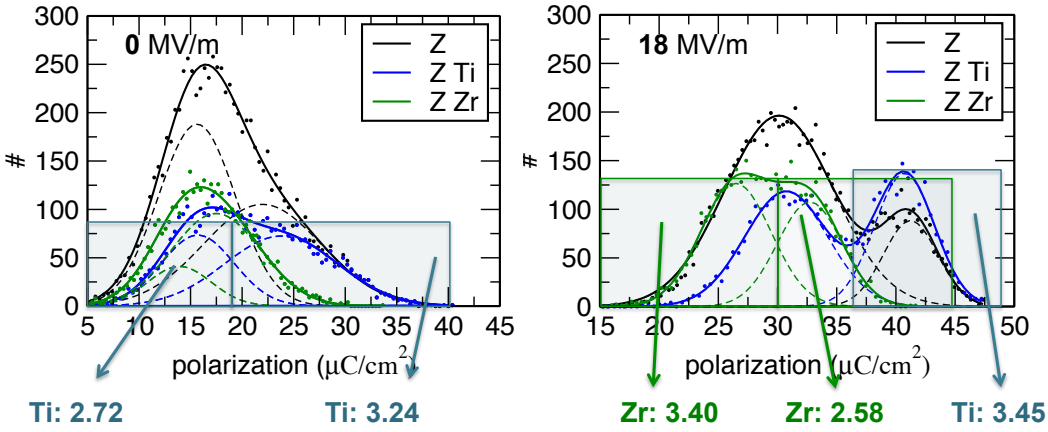

Figure 5.4: Polarisation distributions for the Zr (green) and Ti (blue) contributions at 0 MV/m (left) and 18 MV/m (right). The number corresponding to the coloured boxes denotes the number of nearest B-cation neighbours of each species for a given B-cation within the highlighted part of the distribution. For both, 0 MV/m and 18 MV/m the parts of the polarisation distributions covering the larger polarisation values are Ti rich (average number of Ti nearest neighbours > 3), while the lower polarisation values are positioned in a Zr rich environment (average number of Zr nearest neighbours > 3).

In a further step, I investigated the influence of the local environment on the polarisation of the B-cations. For this, I calculated the number of nearest B-cation neighbours of each species for a given B-cation (see Fig. 5.4). This measure serves as an indicator of how many Ti or Zr atoms there are in the immediate neighbourhood of a B-cation out of the total 6 nearest neighbours. I report, that at zero field the higher polarised unit cells ($P_z > 18\ \mu C/cm^2$) have 3.24 Ti atoms (2.76 Zr) as nearest neighbours on average. This means that locally, the unit cells occupying high polarisation values are positioned in a Ti rich environment. The reverse is true for the low polarised unit cells ($P_z < 18\ \mu C/cm^2$), where I find an average of 2.72 Ti atoms (3.28 Zr) surrounding the unit cells, making the neighbourhood Zr rich. The amount of P for a unit cell is therefore determined by its local environment, specifically by the amount of Ti or Zr as its B-cation neighbours. Similar conclusions can be drawn from the 18 MV/m results where the large P_z values are occupied by unit cells surrounded by predominantly Ti. Note, that the B-cations were randomly placed in the simulation cell. For a system with long range chemical order, as for example PZT

P4mm, I would therefore expect a very narrow distribution of P_z, since all the unit cells see the same B-cation neighbourhood. This means, that the B-cation distribution can have effects not only on the structural, but also on the polarisation homogeneity in PZT, which in turn could influence its domain arrangement.

5.2 Low Temperature Polarisation Switching in $Pb(Zr_{0.5}Ti_{0.5})O_3$

To understand the effect of temperature on the performance of PZT, our collaborators carried out a series of experimental measurements of P-E loops in PZT ($x \sim 0.47$). In addition to the experiments, the ferroelectric response of PZT was modelled using classical MD simulations at a wide range of temperatures. MD simulations were employed to calculate hysteresis (P-E) loops for a range of temperatures and noted the variation in the coercive field (E_C) and saturation polarisation with temperature. The calculated temperature variation of the coercive field displayed qualitatively similar behaviour to the measured temperature variation.

5.2.1 Electrical Measurements of $PbZr_{0.53}Ti_{0.47}O_3$

Our collaborators under the lead of C. Veccini performed electrical measurements of ceramic PZT samples (x=0.47) on the XMaS beam-line at the European Synchrotron Radiation Facility (ESRF). They used a method to measure P-E loops on the beam-line which has been previously described in ref. [114]. A similar setup has been used recently to measure P-E loops of PZT in-situ during an X-ray diffraction experiment by Ryding et al. [115].

This section presents the measured polarisation loops of a commercial pressed pellet of PZT ceramic PZT-5H (Morgan Electroceramics), with the exact composition being proprietary information. Earlier reports found the material to be $PbZr_{0.53}Ti_{0.47}O_3$ with a rhombohedral crystal structure at room temperature [116].

The experimental P-E curves (Fig. 5.5a) display the expected hysteretic behaviour with low losses. Cooling the sample from room temperature to 250 K shows a slight increase of E_C. Further lowering of the temperature to 200 K is accompanied by a widening of the P-E loop that results in lower saturation polarisation values P_S and the increase of E_C. This is typical for ferroelectric materials, as shown earlier for PZT [117], $BiFeO_3$ [118], $SrBi_2Ta_2O_9$ [119] and ferroelectric polymers [120]. Although P-E loops in PZT for different temperatures have been measured before [117], the temperature dependence of E_C and its implications have not been discussed. Interestingly, I observed that below 160 K the P-E loops

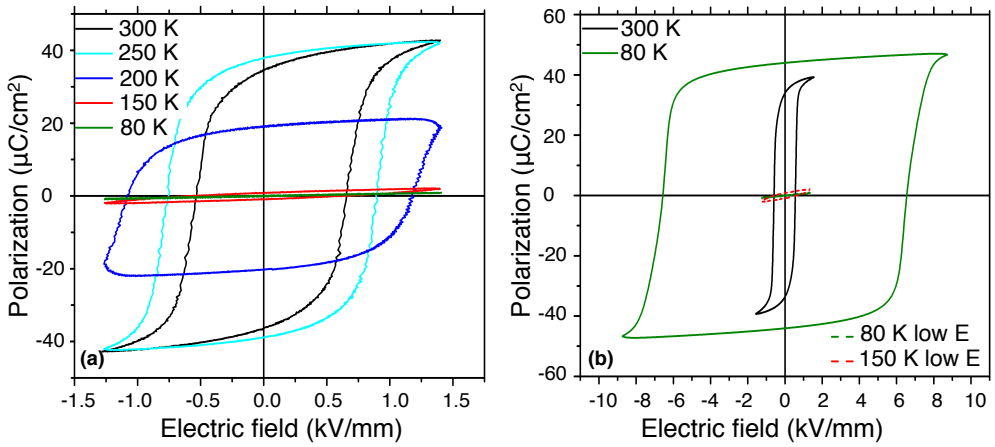

Figure 5.5: (a) Measured P-E loops of PZT sample at different temperatures. With the temperature decrease the ferroelectric loops reduce their area demonstrating a dielectric-like response. (b) A comparison of 150 K and 80 K loops measured high (9kV/m) and low (1.5 kV/m) electric fields. The higher 9 kV/m fields restore the square shaped hysteresis loop in PZT.

exhibit a very narrow hysteresis and low polarisation, akin to curves of leaky dielectrics. The low temperature behaviour observed here is similar to the results of an earlier NASA study on PZT [117]. The narrow loops and low coercive field observed at low temperature behaviour are a direct result of E_C becoming larger than the applied field of 1.5 kV/mm. This was confirmed by further experiments with an applied field of 9 kV/mm, which displayed a large, square hysteresis loop (Fig. 5.5b). The E_C values for different temperatures (T) are fitted well with an exponential function ($E_C = 0.528 * exp(-T/60.0) + 0.508$). The implication of this exponential increase is that it will be necessary to use high fields to employ switchable ferroelectric devices at low temperatures.

5.2.2 Modelling of P-E Loops

To gain further insight into the temperature behaviour of the coercive field, MD simulations of P-E loops in $PbZr_{0.5}Ti_{0.5}O_3$were performed. As in the previous section I used the *NST* ensemble and a Nosé-Hoover thermostat (0.01 ps) and barostat (0.1 ps). A time step of 0.2 fs was selected, along with the Ewald sum method to calculate electrostatics. A $20 \times 20 \times 20$ supercell of $PbZr_{0.5}Ti_{0.5}O_3$ containing 40'000 atoms was used. The two types of B-cations (Ti and Zr) were randomly distributed over the B-sites to obtain the stoichiometry of $PbZr_{0.5}Ti_{0.5}O_3$. The zero field structure was found to be monoclinic below 100 K ($a = 4.043$ Å, $b = 4.044$ Å, $c = 4.045$ Å), rhombohedral at 200 K ($a = b = c = 4.047$ Å) and tetragonal

at 300 K ($a = b = 4.036$ Å, $c = 4.078$ Å). P-E loop calculations were then performed by ramping the electric field along [001] in 1 kV/m steps in a range from -30 kV/m to +30 kV/m. The system was equilibrated for 4 ps at each value of the electric field and the polarisation was calculated during a subsequent production run of 6 ps.

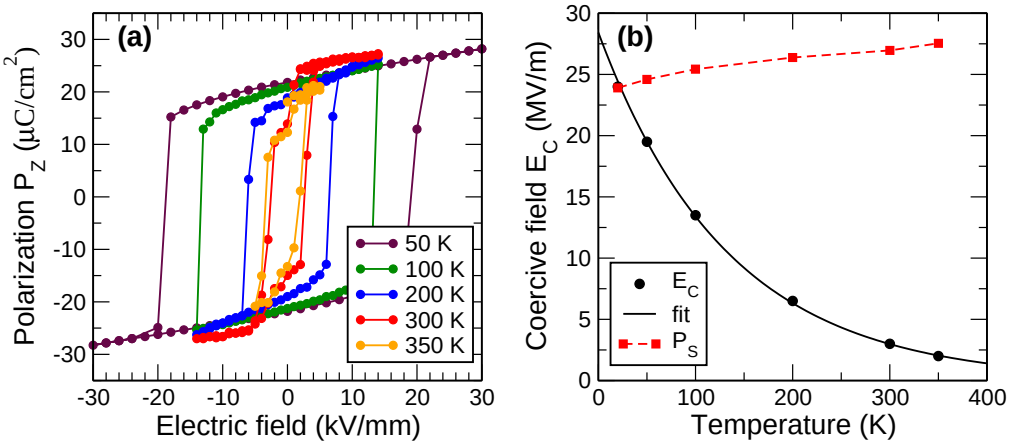

Figure 5.6: (a) Temperature dependence of the z-component of polarisation (P_Z) with respect to the applied electric field E (P-E loops) performed with MD for $PbZr_{0.5}Ti_{0.5}O_3$. With the temperature rise, the shape of P-E loops evolves from square-like to complex shapes due to increased polarisation fluctuation at high temperatures. (b) Temperature dependence of E_C (black dots) and P_S (red squares), both inferred from the P-E loops in (a). The values of E_C drop exponentially with temperature (black line).

The MD simulations reproduced the polarisation hysteresis in PZT very well. Indeed, through the cycling of the electric field in the quasi-static simulations I have calculated P-E loops (Fig. 5.6a) for $PbZr_{0.5}Ti_{0.5}O_3$ that show the characteristic square shaped loops of the ferroelectric system. As the temperature increased, the P-E loops became narrower and less square shaped, signifying that the switching process occurs via a series of multiple events. For the temperatures above 300 K the shape of P-E loops becomes more complex because of increasing polarisation fluctuations in the system. At high temperatures a small amount of in-plane polarisation along x and y develops spontaneously, which reduces the z-component (P_Z), as the total polarisation is unchanged. This effect is most prominent around zero field. The value of E_C, the critical switching field, and the saturation polarisation (P_S) was obtained from the modelled P-E loops. The temperature behaviour of P_S shows a monotonic increase, while E_C exhibits an exponential decrease with the temperature rise (Fig. 5.6b). Thus, at low temperatures (< 200 K) the values of E_C exceed the fields of several kV/mm

usually applied in experiments and devices. The E_C in Fig. Fig. 5.6b is about an order of magnitude lower than the E_C value calculated from first-principles for switching through the polar ferroelectric mode in PZT by Beckman et al. [93]. The lower E_C found in the simulations suggests that the actual polarization switching in PZT follows a lower energy path than the polar mode, such as through polarization rotation or domain wall motion after domain nucleation, which are two intrinsic mechanisms that could lower the repolarization barrier [121].

The measurements and the modelling results, therefore, demonstrate a good qualitative agreement - the temperature dependence of the coercive field exhibits an exponential dependence. Quantitatively, I have found different exponential parameters for the modelled and experimental dependences. Indeed, the experimental exponential factor is half that found for the MD curve. The lower E_C value measured in the experiments is probably due to the presence of domain walls in the experimental samples. The walls introduce the possibility of switching via domain wall motion at lower electric fields. Note, that the simulated bulk PZT was initially a monodomain where domain wall motion is possible only after domain nucleation. Nevertheless, the exponential behaviour we find in experiments and simulations highlights the importance of temperature on measured material properties, where a small change of temperature affects E_C and related quantities.

5.3 Simulations of Polarisation Switching

The dynamic nature of MD simulations allows us to observe the polarisation switching in PZT in real time, not just as a function of electric field as seen in the two previous sections. During the simulation one can calculate the polarisation components for each timestep and therefore investigate the dynamics of the repolarisation process. In the following three sections I analyse the effect of the temperature, the electric field and the B-cations and to the polarisation switching in PZT.

5.3.1 Effect of the Temperature

To investigate the origin of the low coercive field reported in section 5.2 compared to the E_C along the polar mode [93] and to provide insight into the switching kinetics, I modelled a single polarisation switching event using MD. The initial $PbZr_{0.5}Ti_{0.5}O_3$ system was poled along [001] with a P_Z of 40 μC/cm^2 and negligibly small P_X and P_Y. This first step induces the tetragonal symmetry with a polar axis along [001], as seen in section 5.1.1. An electric

field of 30 MV/m was then applied along [00$\bar{1}$] and calculated the polarisation for each unit cell at each MD timestep until the system completely repoled along [00$\bar{1}$]. I plot the P_Z-component during the switching process in Fig. 5.7a. One can see that, for the considered temperatures (100 K, 200 K and 300 K), P changes sign, indicating the polarisation reversal.

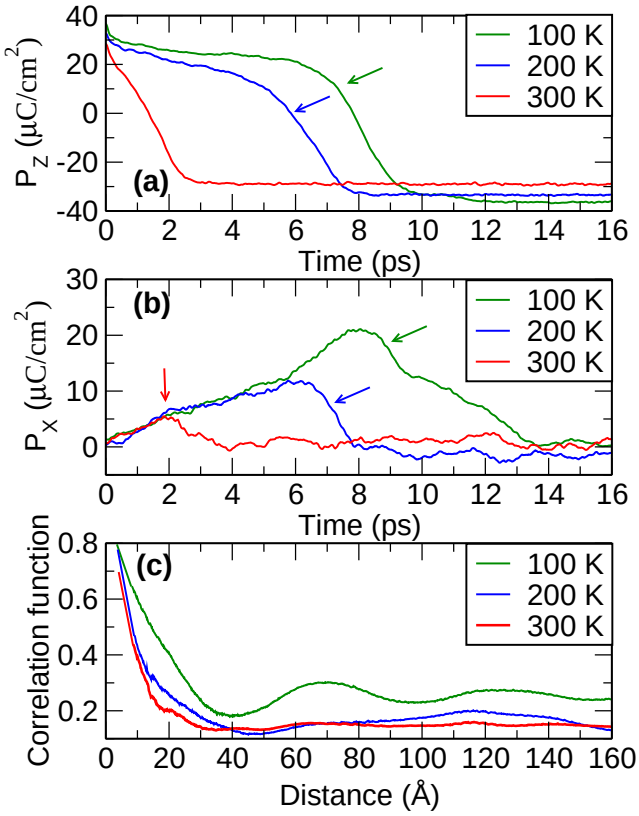

Figure 5.7: The change in the polarisation components during the polarisation reversal. (a) The variation of the z-component (P_Z) with time for different temperatures. At 100 K (green) P_Z follows a power-law behaviour compared to a linear curve at 300 K (red). Different switching times were achieved depending on the temperature. (b) The variation of the x-component (P_X) of the polarisation with time for different temperatures. Lower temperatures (green) result in much larger P_X contributions during the switching then higher temperatures (red). (c) The correlation between the local dipole moment of the unit cells with distance, at the time of polarisation reversal ($P_Z = 0$). At low temperature (green) the local polarisation remains much more correlated over larger separations than at higher temperatures (red).

I registered very different switching times for different temperatures. The switching time for room temperature (T=300 K) is 2 ps and it increases to 8 ps for low temperatures (T=100 K). This behaviour agrees qualitatively with previous experiments on PZT [107], where the switching times decrease with increasing temperature. The analysis of polarisa-

tion dynamics demonstrates that, for the room temperature regime (T=300 K), the values of P_Z drop almost linearly with time during the switching (Fig. 5.7a red line). In contrast, at lower temperatures P exhibits different dynamics, as it follows a power law (Fig. 5.7a green and blue lines). This difference is underlined by a large build up of in-plane components of P (Fig. 5.7b green and blue lines). The latter indicates that the system responds to the applied $[00\bar{1}]$ electric field through the reduction of the P_Z component and simultaneously maintains its in-plane components, P_X (see Fig. 5.7b solid red line). As soon as P_X (or P_Y) is large enough, the polarisation can rotate, which results in the system repoling homogeneously. This switching mechanism is similar to that found in MD simulations on $PbTiO_3$ [110].

The local dipole correlation function was calculated as $\rho(d) = \sum_{i,j} \frac{<P_i \cdot P_j>}{\sigma_i, \sigma_j}$, where i and j are unit cells separated by d, P_i the dipole vector (polarisation vector) of cell i and σ_i its standard deviation. Fig. 5.7c shows the correlation of the polarisation with distance at the polarisation reversal when $P_Z = 0$. For all temperatures the correlation drops rapidly with distance, yet at 100 K the system retains some correlation for separations over 60 Å. This signifies that the PZT forms large domains where the dipole moments are correlated. At higher temperatures (300 K) the correlation at large distances is small and constant (red curve), as a result of the system being split up into many nucleated reversed domains that are not correlated. This nucleation mediated switching at 300 K agrees well with the experimental findings for thin PZT films [122], where the Stolichnov et. al. proposed that at room temperature PZT re-poles through multiple nucleation events, while at lower temperatures domain wall motion dominates the switching kinetics. Here I suggest that, in the absence of domain walls, polarisation rotation governs the low temperature switching.

The difference in switching mechanisms is emphasised in Fig. 5.8, where I present the mechanisms in a schematic sketch together with snapshots of the simulated PZT system at 100 K and 300 K. The snapshots are plotted as 2D slices in the x-z plane in (b) and (c), demonstrating the distinct domain structures related to the switching process. The figures show the local dipole moments, for the system switching from P_Z to -P_Z at the state where $P_Z = 0$, e.g halfway through the polarisation reversal. One can see that at 100 K (Fig. 5.8b) the system consists mostly of one large domain which is polarised along x with $P_Z \sim 0$. This agrees with Fig. 5.7, which shows a large contribution of the x-component of polarisation during the switching. In contrast, the system at 300 K (Fig. 5.8c) exhibits a much denser

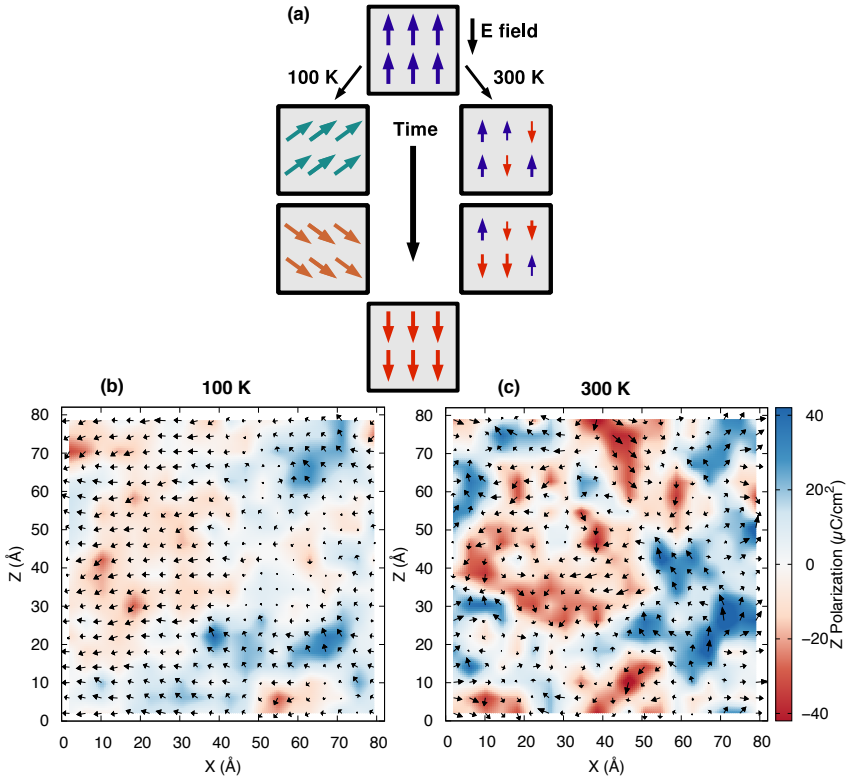

Figure 5.8: (a) Schematic representation of the different polarisation switching mechanisms: polarisation rotation at lower temperature (left) and nucleation of reversed domains at higher temperature (right). The arrows correspond to the local dipole moments. (b) and (c) Snapshots of the local dipoles in PZT during MD simulated polarisation switching at 100 K and at 300 K. The snapshots were taken halfway through the polarisation reversal (total $P_Z = 0$) and each arrow corresponds to the local dipole moment of a conventional unit cell (defined in eq. I). The colour gradient represents the magnitude of P_Z. (b) The low temperature system (T=100 K) exhibits a homogeneous domain pattern during the switching process with well-defined in-plane contribution where P_Z is small and P_X is large. (c) At high temperature (T=300 K) PZT breaks up into multiple reversed domains, as seen by the many up (blue) and down (red) polarised parts.

domain pattern with small domains polarised along +z or -z and much less in-plane polarisation along x. Overall, the 100 K domain structure is more homogeneous than the 300 K one.

Note, that at zero field the force field supports the multiple phases of $PbZr_{0.5}Ti_{0.5}O_3$: monoclinic symmetry at 100 K, rhombohedral symmetry at 200 K and tetragonal symmetry at 300 K (see section 4.2.3). The monoclinic and rhombohedral phases could, therefore, be the origin of the the observed rotational mode, by facilitating the polarisation rotation. To rule out the correlation of the rotational switching mode with the low temperature symme-

tries, I modelled a strictly tetragonal PZT composition. I carried out similar calculations of polarisation switching events as described above, for tetragonal *P4mm* $PbZr_{0.2}Ti_{0.8}O_3$ at a field of 80 MV/m. Remarkably, I found that at low temperatures (100K) the tetragonal $PbZr_{0.2}Ti_{0.8}O_3$ also exhibits rotational polarisation switching, while at high temperatures (300 K) the nucleation mechanism prevails. Thus, the coexistence of the two switching mechanisms, rotation and nucleation, appears to be a general phenomenon that is generic for ferroelectric perovskite compounds. However, presence of defects or free surfaces in ferroelectric materials may significantly affect the polarisation rotation mechanism due to strain, interfaces or the direction of growth in thin films. On the other side, the presence of some defects such as oxygen vacancies strongly reduce the barrier for polarisation rotation [123].

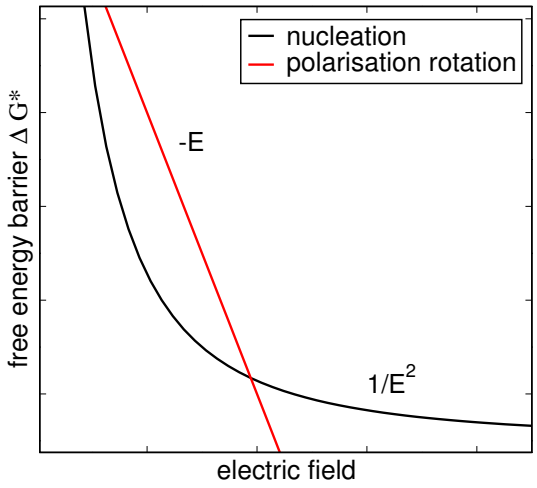

Figure 5.9: Free energy barrier (ΔG^*) vs. electric field for the nucleation (black) and polarisation rotation (red) mechanisms.

Further, I apply classical nucleation theory to explain the temperature and the field dependence of the polarisation switching mechanism. Assuming that the energy gain of the volume term is proportional to $E \cdot P$ the energy barrier for nucleation (ΔG^*) decreases with the inverse of the electric field squared ($\Delta G^* \propto \frac{1}{E^2}$). For the rotational switching I expect the energy barrier to decrease linearly with field ($\Delta G^* \propto A - B \cdot E$, where A and B are constants). For both mechanisms the height of the energy barrier decreases with increasing applied field, however, the different electric field dependencies of ΔG^* mean there is a crossover between the two switching mechanisms, as seen in Fig. 5.9. At high temperatures switching occurs at low fields where the linear relationship ensures that the barrier for rotation is

higher than the barrier for nucleation. At low temperatures, on the other hand, high fields are required for switching and in this regime the barrier for nucleation is lower than the barrier for rotation. These arguments explain the similar polarisation switching behaviour found in the structurally different compounds $PbZr_{0.5}Ti_{0.5}O_3$ and $PbZr_{0.2}Ti_{0.8}O_3$.

5.3.2 Effect of the Electric Field

The previous section showed differences in the switching behaviour of $PbZr_{0.5}Ti_{0.5}O_3$ depending on the temperature. In this section I inspect the switching dynamics further, by examining different electric field strengths and different compositions of PZT.

The effect of the electric field strength on the switching time has been studied with MD simulations similar to the previous section (5.3.1). Three different $20 \times 20 \times 20$ supercells have been considered: rhombohedral $PbZr_{0.5}Ti_{0.5}O_3$, prepoled tetragonal $PbZr_{0.5}Ti_{0.5}O_3$ and tetragonal $PbZr_{0.2}Ti_{0.8}O_3$. The tetragonal $PbZr_{0.5}Ti_{0.5}O_3$ was produced by applying an electric field of 30 MV/m along $[00\bar{1}]$ to prepole it along the c-axis. All systems were equilibrated at 200 K and zero field for 20 ps. To induce the polarisation reversal, I then applied electric fields of different magnitudes from 10 MV/m to 500 MV/m along [001].

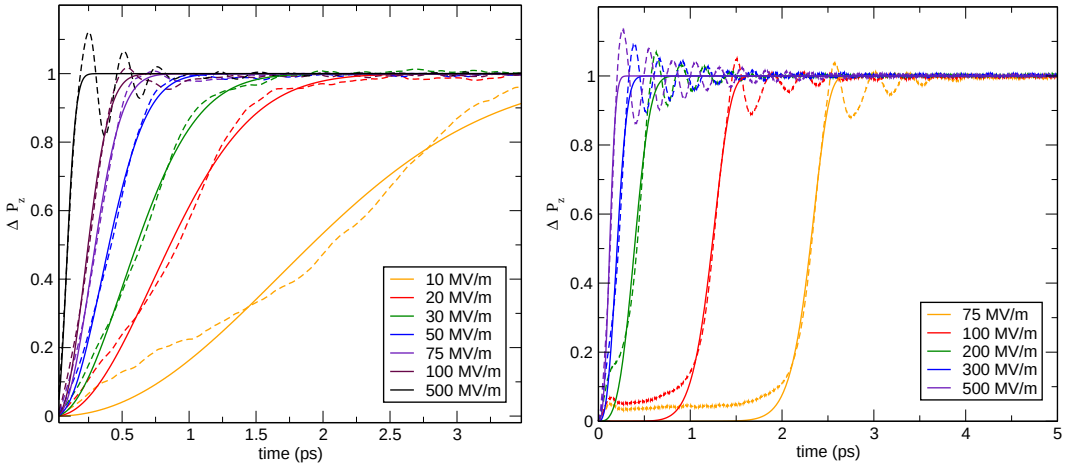

Figure 5.10: Change of the z component of the polarisation (ΔP_z) for rhombohedral $PbZr_{0.5}Ti_{0.5}O_3$ (left) and tetragonal $PbZr_{0.2}Ti_{0.8}O_3$ (right) for different electric fields. The dotted lines represent the calculated values, while the solid lines are the fit to the KAI model (eq. 5.1).

Fig. 5.10 shows the change in polarisation (ΔP) with time for the z component of rhombohedral $PbZr_{0.5}Ti_{0.5}O_3$ (left) and tetragonal $PbZr_{0.2}Ti_{0.8}O_3$ (right) as dotted lines. The switching time is strongly field dependent and follows a power law in both cases, agree-

ing with the 200 K curve in Fig. 5.7a. An increase in applied field reduces the switching time, analogous to the temperature behaviour in section 5.3.1. Comparing the two different structures, I find that the switching of $PbZr_{0.5}Ti_{0.5}O_3$ is significantly faster than for $PbZr_{0.2}Ti_{0.8}O_3$. Moreover, a much larger field of 75 MV/m has to be applied to successfully reverse the polarisation in $PbZr_{0.2}Ti_{0.8}O_3$, compared to 10 MV/m for $PbZr_{0.5}Ti_{0.5}O_3$. This is likely due to the underlying symmetries of the supercells: At 200 K part of the polarisation switching will occur through nucleation and part through polarisation rotation, as discussed in section 5.3.1. $PbZr_{0.5}Ti_{0.5}O_3$ is rhombohedral which will facilitate polarisation rotation, since it has large (equal to P_Z) P_X and P_Y contributions, while $PbZr_{0.2}Ti_{0.8}O_3$ is tetragonal which requires a build up of P_X or P_Y for rotation (see Fig. 5.12). The composition of PZT and thereby the phase of the material has a large influence on the switching time. Note, that the structure of the ferroelectric can also be influenced by external electric fields, as I demonstrated in section 5.1.1.

The time dependence of the polarisation switching can be analytically described by the KAI model [107, 124]:

$$\Delta P(t) = 2P_s\left[1 - exp\left(-\frac{t}{t_0}\right)^n\right], \tag{5.1}$$

where ΔP is the change in polarisation, P_s is the saturation polarisation, t is the time, t_0 is the characteristic switching time and n is the dimension of domain growth. The KAI model, named after its authors Kolmogorov-Avrami-Ishibashi [125, 107], is a statistical model based on nucleation and domain growth. It includes the t_0 parameter as the switching time of the sample and the parameter n, describing an effective dimension of domain growth. The domain growth dimension is usually around 3 for bulk ceramics and close to 2 for thin films [107], therefore matching the physical dimensions in which the domains grow.

The simulation results can be fitted to the KAI model, as the solid lines in Fig. 5.10 show. The switching time (t_0) is captured well by the model, in contrast to the oscillations after the repoling. These ΔP oscillations around $\Delta P = 1$ are more pronounced for larger fields and are a result of the small system size and the barostat: After the repoling the system takes a certain time (depending on the barostat) to relax to its new configuration. Nevertheless, the KAI model seems to fit the actual process of repoling during the MD simulations, even though the model is solely based on nucleation. This is further indication, that nucleation events occur in the MD simulations during switching and that polarisation

rotation is not dominant at 200 K.

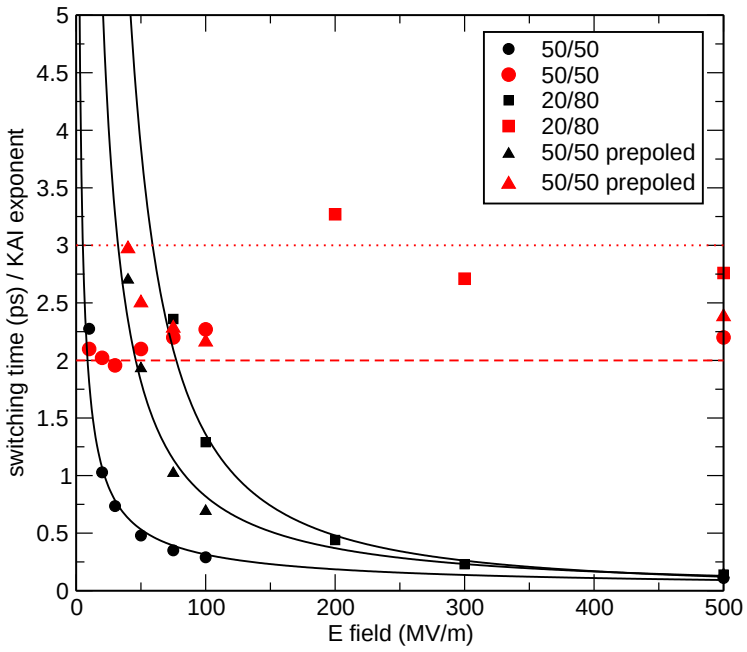

Figure 5.11: Switching time (black) and KAI domain growth exponent (red) at different electric fields for rhombohedral $PbZr_{0.5}Ti_{0.5}O_3$ (circles), tetragonal $PbZr_{0.5}Ti_{0.5}O_3$ (triangles) and tetragonal $PbZr_{0.2}Ti_{0.8}O_3$ (squares).

In Fig. 5.11 I compare the switching times (black lines, fitted to a power law) and the effective dimensions (red) from the KAI model for rhombohedral $PbZr_{0.5}Ti_{0.5}O_3$, tetragonal $PbZr_{0.5}Ti_{0.5}O_3$ and tetragonal $PbZr_{0.2}Ti_{0.8}O_3$. I confirm that $PbZr_{0.5}Ti_{0.5}O_3$ exhibits shorter switching times than $PbZr_{0.2}Ti_{0.8}O_3$, while the prepoled tetragonal $PbZr_{0.5}Ti_{0.5}O_3$ lies in-between. The phase of PZT seems to be an important factor to the switching time. The two tetragonal samples switch significantly slower than the rhombohedral system, for the same applied fields. Nevertheless, the prepoled (induced tetragonal) $PbZr_{0.5}Ti_{0.5}O_3$ still switches faster than the tetragonal $PbZr_{0.2}Ti_{0.8}O_3$, despite them having the same symmetry at the start of the simulations. This is most likely due to $PbZr_{0.5}Ti_{0.5}O_3$ having a rhombohedral phase as its ground state at 200 K, which will facilitate the fast polarisation rotation route of switching.

Regarding the dimension of domain growth, I find that for $PbZr_{0.5}Ti_{0.5}O_3$ n is close to 2 for all applied fields. Although, the system represented a 3D bulk material, its effective dimension of domain growth is reduced. Tetragonal $PbZr_{0.5}Ti_{0.5}O_3$ and $PbZr_{0.2}Ti_{0.8}O_3$ show larger n which vary will field strength from over 3 at low fields and approach 2 at

high fields. Observing the domain nucleation and growth during switching (see Fig. 5.8), I do not find any preferred direction or any apparent reduced dimensions of domain nucleation and growth. The low and varying values of n might stem from the fact that the KAI model is not completely applicable in a switching scenario where polarisation rotation contributes significantly to the P reversal. The n values have to be regarded with caution, since they may not represent any physical quantity in these MD simulations. However, the KAI model is still a useful approximation, because the fit gives reasonable switching times. Moreover, the n parameter still reflects some aspects of the polarisation switching, since I find different values for the rhombohedral and the tetragonal systems. For rhombohedral $PbZr_{0.5}Ti_{0.5}O_3$ I find consistent values around 2, while the tetragonal systems display larger numbers. Clearly, the symmetry of PZT influences the switching mechanism greatly, as I have seen for switching time t_0 and as I see in the manifestation of different n for different PZT phases.

5.3.3 Effect of the B-cations

Extending the investigation of the effect of the B-cations on the polarisation in PZT (section 5.1.1), I looked a the polarisation switching dynamically. For this the change of P during the poling at 30 MV/m and at 200 K was analysed. A rhombohedral and a prepoled tetragonal system were used where I applied a field of 30 MV/m along $[00\bar{1}]$ before poling the systems along [001].

Fig. 5.12 shows the change in polarisation (ΔP) with time for the z and the x component (y component behaves similarly to x). ΔP is plotted separately for the Zr (green) and the Ti (blue) subsystem. The rhombohedral system switches in about 3 ps and there is no difference in switching time between Zr or Ti. Both, the Zr and the Ti curve for ΔP_x and ΔP_z follow the same shape, meaning that the two B-cations dynamically respond in a similar way to an applied electric field. Although the polarisation switching is much slower for the tetragonal system (8 ps) there is no difference in switching dynamics of Zr and Ti. Contrary to the static results of section 5.1.1, the Ti and Zr sublattices behave identically in dynamic simulations, for both the tetragonal and the rhombohedral case. These results, however cannot rule out that locally some Zr or Ti rich regions have different switching speeds, e.g. regions where some reversed domains nucleate earlier than others. Averaged over the whole sample, however, there is a strong coupling between the two B-cation based unit cells which makes them switch synchronously.

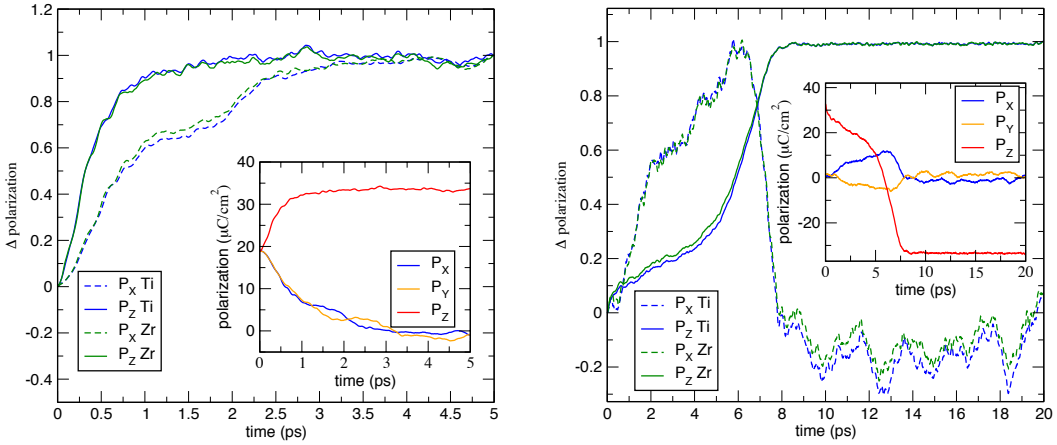

Figure 5.12: Change of polarisation (ΔP_x and ΔP_z) during the switching process for a rhombohedral (left) and prepoled tetragonal (right) system. Green lines denote the contribution from Zr while the blue lines denote the Ti polarisation. Although overall switching times differ between left and right the Ti and the Zr sublattices switch synchronously for both systems left and right. Insets show the absolute polarisation components during the switching.

5.4 Conclusions

In this chapter the effect of electric fields on ferroelectric PZT was studied, where MD simulations under static electric fields show that the strain and the polarisation components vary linearly for small electric fields, while the total polarisation is almost independent of the field. For fields above 14 MV/m, I find that PZT goes through a phase transition from rhombohedral to tetragonal. Through this change in symmetry, Zr based unit cells increase in volume while Ti based unit cells decrease. This difference in behaviour of the B-cation is further seen in the polarisation distributions in PZT where I show that Ti based unit cells adopt high polarisation values and Zr based unit cells are less polarised. This confirms that Ti is the ferroelectrically active cation providing most of the contribution to the total polarisation, which is in excellent agreement with conclusions based on recent neutron scattering experiments [30]. Furthermore, I report that the local environment of the unit cell influences its polarisation: A Ti rich neighbourhood results in large polarisation, while a Zr rich neighbourhood leads to low polarisation values. Overall, I find that response of the local structure of PZT to an electric field is therefore not uniform throughout the material and strongly depends on the type of B-cation and its local environment.

Investigating the temperature behaviour, I report P-E loops in ceramic PZT samples, which display an exponential increase of E_C with decreasing temperature, making the use

of high fields necessary to switch PZT at low temperatures. Additionally, I have performed classical MD simulations of polarisation switching dynamics in near-morphotropic PZT. I have successfully reproduced the hysteretic behaviour of the polarisation with applied electric field for different temperatures. As seen in the experimental results, I have found that the shape of the P-E loops is temperature dependent and exhibits narrowing towards high temperatures. The exponential temperature dependence of E_C appears to be generic for ferroelectric materials and independent of the actual switching process, since experiments on polycrystalline ceramics and simulations on domain wall free single crystals exhibit similar behaviour. These findings are important for aeronautical and space applications as they provide guidance on operational temperature/voltage regimes for ferroelectric-based devices that will be exposed to a wide range of operating temperatures.

Lastly, studying the switching dynamics in PZT, I considered the effect of temperature, electric field and the B-cations on the polarisation reversal. I find that the nature of the switching mechanism, observed from simulations at room temperature, was in very good agreement with earlier experimental studies on PLZT thin films [122], where nucleation was found to be the dominating switching process. I predict, however, that at low temperatures nucleation is inhibited and single domain systems will switch through a polarisation rotation mechanism. This rotation of the polarisation has the effect of reducing the switching barrier compared to nucleation induced switching at larger fields.

Moreover, the switching time is largely influenced by the applied electric field and by the phase of the PZT system. I report that rhombohedral PZT, where the polarisation rotation route is facilitated, switches faster than tetragonal PZT. Importantly, even imposing a tetragonal symmetry by prepoling an originally rhombohedral sample slows down the P switching. In contrast to the large effects of the temperature, the electric fields and notably the symmetry, I do not find any influence of the two different B-cations on the switching speed in PZT. With this exception, the structure of PZT and its dependence on the temperature (especially at the MPB) and electric fields, heavily affects the switching mechanism and the switching time. Careful manufacturing and deliberately choosing the working conditions can, therefore, add control and performance to PZT based piezoelectric devices.

Chapter 6

The Effect of B-Cation Disorder in $Pb(Zr_{1-x}Ti_x)O_3$

Lead zirconate titanate $Pb(Zr_{1-x}Ti_x)O_3$ (PZT), is a technologically important piezoelectric due to its excellent electromechanical properties, which are highest at the specific composition of x=0.48 denoted as the Morphotropic Phase Boundary (MPB). Structurally PZT is a homovalent solid solution perovskite, where the B-cations were conventionally considered to be randomly distributed [41]. The two B-cations in PZT (Ti and Zr) carry the same ionic charge of 4+, so there is no apparent driving force for chemical order due to electrostatic effects. However, over the last two decades, a number of theoretical and experimental studies of PZT indicate that the B-cations preserve a certain degree of order and clustering:

Saghi-Szabo and Cohen showed in an early LDA DFT paper that PZT exhibits a favourable long-range [111] (rocksalt) ordering. However, no long-range order of B-cations in PZT was found experimentally until 2008 [42]. It was Zhang et al's work, which first proved the existence of [001] chemical order in epitaxial thin films of $PbZr_{0.2}Ti_{0.8}O_3$ on $SrTiO_3$ via TEM diffraction [42]. Interestingly, the previously mentioned DFT study reports the [111] ordering to be more stable than order along [001], yet an in-plane cation arrangement was found in the thin-film, which is attributed to the misfit strain between the film and the substrate. Furthermore, a more recent study found 5-10 nm sized clusters of segregated B-cations in PZT via atom probe tomography [43]. Notably, these clusters were only found in ceramics of morphotropic PZT, but not in thin films of the same composition. This indicates that the clustering is mainly determined by the manufacturing method.

Although the evidence of order and segregation in the B-cation in PZT is scarce, such structural arrangements could have important effects on the performance and the properties

of PZT based ceramics [41]. Experimentally, it is very challenging to distinguish between the two B-cations with standard methods such as AFM, TEM or XRD. Novel techniques such as the atom probe tomography [43], could help to analyse the B-cation homogeneity in PZT, as can atomistic simulations with large supercells.

In this chapter the effect of order and clustering of B-cations in PZT at morphotropic compositions was studied, using large scale molecular dynamics (MD) simulations. In sections 5.1.1 and 5.1.2 we saw that the B-cation environment influences the local structure and the polarisation distribution in $PbZr_{0.5}Ti_{0.5}O_3$. Here, I calculated energetics and piezoelectric properties for various types of B-cation order, from which I report a large improvement of the piezoelectric properties of PZT when small B-cation clusters are introduced into the material.

6.1 Modelling

Different amounts of B-cation order and clustering were introduced in $40 \times 40 \times 40$ supercells of morphotropic $PbZr_{0.5}Ti_{0.5}O_3$. In all systems the stoichiometry of $PbZr_{0.5}Ti_{0.5}O_3$ was kept and the B-cations were arranged as described in section 6.1.2. The induced order and the B-cation clusters varied in size since the procedure that generated the B-cation distributions was based on a random process (see section 6.1.2). This meant that locally many different configurations of B-cations occurred in the supercell for each studied system. In order to sample enough of these possible local configurations the large supersell size with 320,000 atoms ($40 \times 40 \times 40$) was used for each specific B-cation distribution. The MD simulations were then performed at 200 K, which corresponds to room temperature in the reduced units of the force field, which underestimates the Curie temperature of PZT (see section 4.2.3). A relatively small timestep of 0.2 fs was chosen and the shell particles were treated adiabatically. The Nosé-Hoover thermostat (0.01 ps) and barostat (0.1 ps) in the NST ensemble was used and the system was equilibrated for 50 ps, followed by 250 ps production. Note that these simulation details were used for the whole chapter unless stated otherwise.

6.1.1 Dielectric and Piezoelectric Tensors

Piezoelectric and dielectric tensors can be calculated from MD simulations as described in section 3.4.2. The differential approach and the covariance approach are two methods to calculate such tensors and they both require different sets of simulations: For the differential approach, relatively short simulations (20 ps) have to be performed for several different values of the electric field, in order to obtain the linear relationship between the strain and the field, which gives the piezoelectric coefficient. To obtain all tensor components the electric field has to be applied along all the relevant directions. An advantage of this method is that all these calculations are independent and can be performed in parallel. The covariance method, on the other hand, needs very long runtimes [71], but the full tensor is obtained from just one simulation.

Table 6.1 compares the differential and the covariance approach for $12 \times 12 \times 12$ supercells of $PbTiO_3$ (PTO) and ordered *P4mm* $PbZr_{0.5}Ti_{0.5}O_3$ (PZT) (see Fig. 4.2). As a reference I used single unit cell calculations done in GULP [73], which readily outputs the piezoelectric tensor. For PTO, the three methods agree rather well with the biggest discrepancy being the $d_{31} = -17.319$ pC/N for the covariance approach and $d_{31} = -14.862$ pC/N

Table 6.1: Comparison of the components of the piezoelectric tensor calculated wth the derivative and the covariance methods. For further comparison, the single unit cell values calculated with GULP are given for $PbTiO_3$ (PTO) and ordered *P4mm* $PbZr_{0.5}Ti_{0.5}O_3$ (PZT).

	PTO			PZT		
	derivative approach	covariance approach	GULP	derivative approach	covariance approach	GULP
d_{31} (pC/N)	-15.07	-17.32	-14.86	-61.06	-12.04	-10.46
d_{33} (pC/N)	48.56	53.13	52.02	193.48	37.52	37.07

for GULP. On the other hand, the results for PZT demonstrate a large difference between the derivative method ($d_{31} = -61.059$ pC/N) and GULP ($d_{31} = -10.458$ pC/N), whereas the covariance method ($d_{31} = -12.037$ pC/N) is in agreement with the GULP result. Here, I observe an issue with the derivative approach, which is further highlighted in Fig. 6.1.

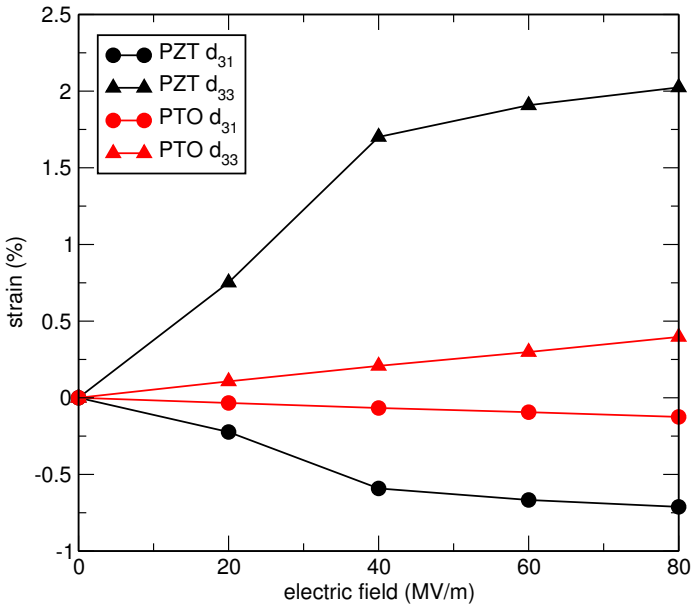

Figure 6.1: Strain versus electric field behaviour for $PbTiO_3$ (PTO) and ordered *P4mm* $PbZr_{0.5}Ti_{0.5}O_3$ (PZT).

In Fig. 6.1 the strain (η) versus electric field (E) behaviour is plotted for PTO and PZT, from which the piezoelectric tensor components can be derived. The PTO curve displays a linear behaviour and therefore leads to a good quality linear fit. In contrast, the PZT behaviour is largely non linear and the derivative of the curve depends on the electric field.

This is an effect of the coupling of the structure of PZT with the electric field, which was studied in section 5.1. As a result, the linear strain field relationship is not strictly valid for large fields in morphotropic PZT and the calculation of the piezoelectric tensor from a linear fit is, therefore, ambiguous. Interestingly, the covariance approach leads to good agreement with the GULP values even for $PbZr_{0.5}Ti_{0.5}O_3$. Since no external field is applied in this method, the structure of PZT is not perturbed by the field. Because of its good agreement with GULP values, and the fact that a single calculation yields the piezoelectric and the dielectric tensors simultaneously, I choose the covariance approach to calculate the piezoelectric properties of PZT in the following sections.

6.1.2 Cluster Factor

The B-cation order and the clustering in the PZT supercells was introduced by selectively placing the B-cations (Ti and Zr) according to the so-called cluster factor (CF). The cluster factor is a measure of the order and the clustering simultaneously, that acts as a bias on the placements of the cations on the B-sites. For a zero CF, no bias on the B-cation placement was added and both ions were placed randomly in the supercell, e.g. with 50% probability of finding a Zr or a Ti on the B-site. Applying a non-zero cluster factor then means revisiting each B-site randomly and update the placement probability according to the CF and the type of the nearest neighbour (NN) B-cations. This means that for each NN of the same type as the current B-site ion, the value of the cluster factor is added to the probability of placing the B-cation. For each NN B-cation of the other type as the current B-site ion the CF is subtracted from the placement probability of that B-cation. The B-cation type on the current B-site is then updated according the newly determined probability P:

$$P = 0.5 + n_{same\ type}\, CF - n_{other\ type}\, CF, \tag{6.1}$$

where $n_{same\ type}$ is the number of nearest neighbour B-cations of the same type, $n_{other\ type}$ is the number of nearest neighbour B-cations of the other type and CF is the cluster factor. This update of the B-cations, which incorporates the CF, was performed until every B-site was randomly visited twice.

In other words, a positive cluster factor increases the likelihood of finding an ion next to an ion of the same species, thereby grouping up ions of the same kind. A positive cluster factor leads to clusters whose sizes will depend on the cluster factor (larger CF = larger clusters). A negative cluster factor will reduce the chance of finding an ion of the same species

as a neighbour, thereby introducing short ranged structures with alternating B-cations. Fig. 6.2 shows the effect of the cluster factor on some sample cells. One can see that positive cluster factors lead to aggregates of the same type of ions, effectively resulting in phase segregation for large values. On the other side, negative cluster factors introduce chemical order into the sample, leading to a rocksalt type [111] ordering for very large negative values.

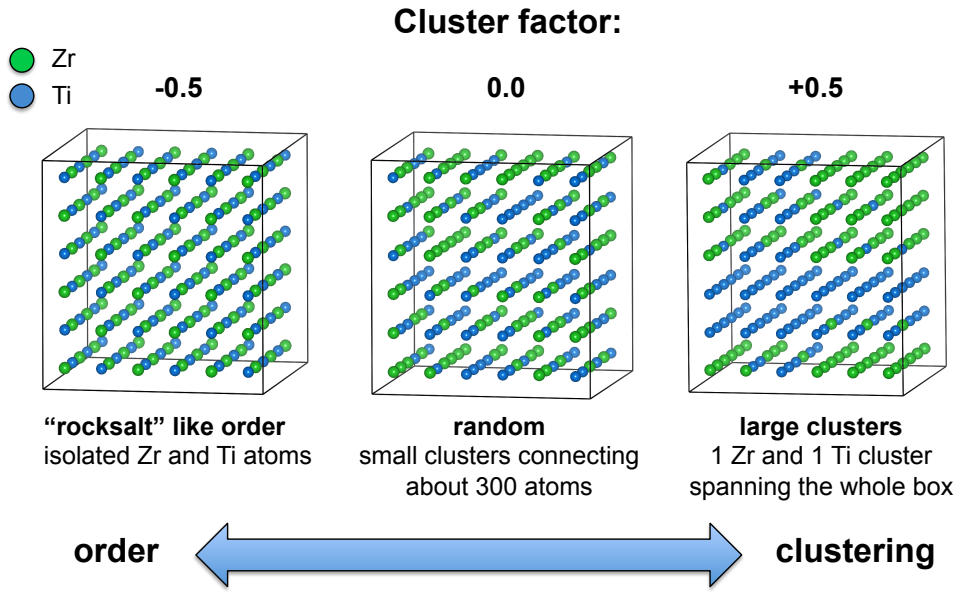

Figure 6.2: B-cation distribution for different cluster factors. The cluster factor determines the amount of order (negative values) or clustering (positive values) of the simulations cells. At a cluster factor of 0 the atoms are randomly placed. Applying the cluster factor then acts as a bias to place neighbouring atoms. A positive cluster factor increases the likelihood of finding an ion next to an ion of the same species, while a negative cluster factor decreases this chance, making it more likely to find an ion next to an ion of the other species.

6.2 Total Energy for Different Cluster Factors

Fig. 6.3 shows the the total energy per formula unit for different cluster factors with respect to the completely random sample (cluster factor = 0). For ordered systems with negative cluster factors the total energy of the morphotropic PZT decreases up to 22 meV per formula unit. There is a monotonic decrease in total energy with increasing the B-cation order, which indicates that chemical order is energetically preferred for this solid solution. The rocksalt type [111] ordering, which is achieved for a cluster factor of -0.5, has the lowest energy and is therefore most stable for all tested configurations.

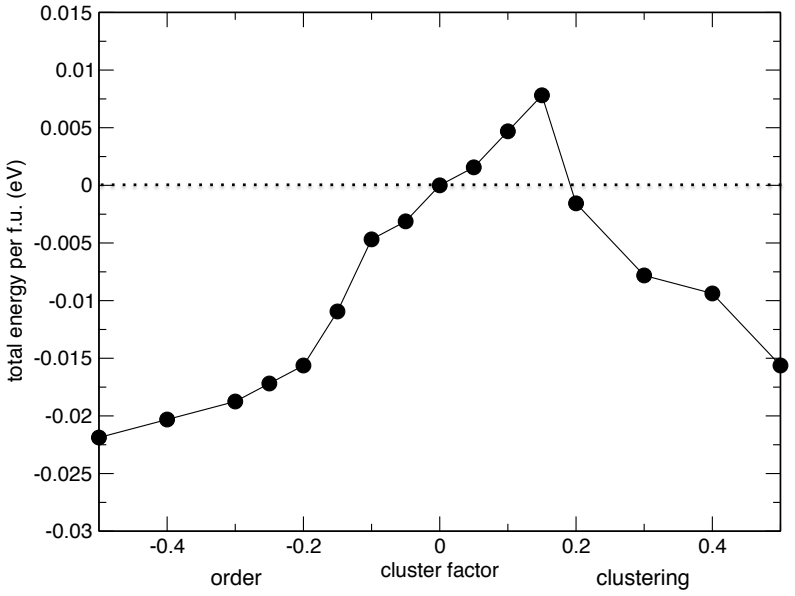

Figure 6.3: Total energy per formula unit with respect to the zero cluster factor value for different cluster factors.

For positive cluster factors, small agglomerates of the same B-cations tend to increase the total energy up to 0.07 meV, making these systems less stable. Regarding larger clusters (cluster factor >= 0.2), the total energy again decreases up to 16 meV for the purely segregated system with a cluster factor of +0.5. Large clusters are therefore energetically more stable than the randomly mixed systems which agrees with the positive mixing enthalpy reported by Rane et al. [126]. Note, that I only considered the enthalpy and not the free energy of the configurations, as these calculations did not include entropic contributions. However, the entropy of mixing will favour B-cation disorder, e.g. a cluster factor around zero where the B-cations were placed randomly, and it will be an important contribution at higher temperatures.

Regarding the enthalpy, I conclude that order, as in alternating B-cation structures, and large clusters are both favourable in PZT. It is the small clusters and nearly random B-cation distributions that are unstable, which conflicts which the conventional belief that there is chemical order found in this solid solution [41].

6.3 Polarisation for Different Cluster Factors

The polarisation behaviour of PZT for different cluster factors is shown in Fig. 6.4, together with an inset displaying the Curie temperature (T_C). To calculate T_C I performed step-wise

annealing of the different PZT configurations, from 300 K to 500 K, in steps of 20 K. At each temperature step the system was equilibrated for 20 ps followed by 40 ps of production.

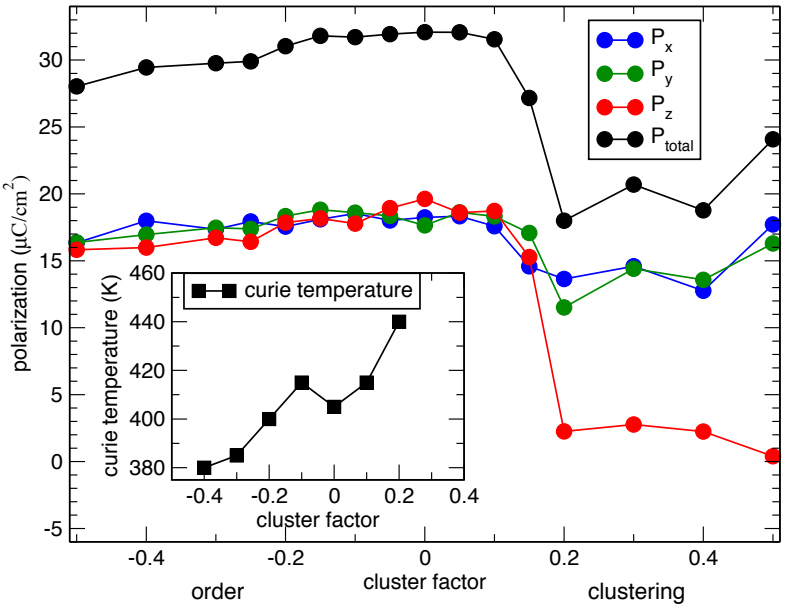

Figure 6.4: Components of polarisation and total magnitude of polarisation for different cluster factors. The inset shows the dependence of the Curie temperature (T_C) with respect to the cluster factor.

Remarkably, the random system with a cluster factor (CF) of 0 has the highest total polarisation. With increasing order, the total polarisation drops slightly from 33 $\mu C/cm^2$ to 28 $\mu C/cm^2$ (-15%) at a cluster factor of -0.5. However, the polarisation is relatively stable (-6%) up to a cluster factor of -0.2. The individual components of the polarisation stay roughly equal for all negative cluster factors, while the rhombohedral symmetry of $PbZr_{0.5}Ti_{0.5}O_3$ at 200 K is preserved.

Introducing small clusters up to a CF of +0.1 does not change any of the polarisation components. Conversely, higher cluster factors (CF>0.2) decrease the polarisation significantly. Here the z-component of the polarisation vanishes with increasing clustering, which reduces the total polarisation magnitude by about 30%. This coincides with the energy lowering above a CF of +0.2 as seen in Fig. 6.3. The decrease of the polarisation is most likely the result of the emergence of large antiferroelectric PZO agglomerates which decrease the average total polarisation. Moreover, the antiferroelectric clusters of PZO induce local strain into the system, because PZO unit cells are larger than PTO unit cells (section 2.5.2). As a result, the PZO clusters will stretch the lattice locally, forcing the PTO to polarise in

the xy-plane which reduces P_Z to almost zero. For a CF of +0.5 the total segregation of the two phases, leads to a recovery of the total polarisation of 24 $\mu C/cm^2$, which is completely in-plane.

The Curie temperature increases with increasing cluster factor with a small jump at CF=0, where T_C is briefly lowered (see inset of Fig. 6.4) . This shift of the phase transition temperature is a result of the local PTO clusters that have a higher T_C than PZT (see section 4.2.3). Therefore, the Ti rich parts of the system will remain ferroelectric up to higher temperatures, raising T_C for the whole system.

The polarisation and T_C behaviour is very distinct for ordered systems and systems with clusters: The highest polarisation in PZT is achieved for a purely random B-cation arrangement, while introducing order lowers P_{tot} slightly. Clustering of B-cations, on the other hand, is accompanied by a large decrease of the polarisation. The presence of clusters and phase segregation therefore strongly affects the properties of the material, which is also evidenced by the increase of T_C with increasing cluster factor.

6.4 Dielectric and Piezoelectric Tensors for Different Cluster Factors

Using the covariance method tested in section 6.1.1 the components of the piezoelectric and dielectric tensors in PZT were calculated for different cluster factors. The piezoelectric constants are plotted in Fig. 6.5, where the dotted lines represent the values at CF=0. The initial values at CF=0 of $d_{31} = -210$ pC/N and $d_{33} = 429$ pC/N agree with the specifications of a manufacturer of morphotropic PZT ceramics ($d_{31} = -200$ pC/N, $d_{33} = 480$ pC/N) [127]. Changing the B-cation arrangement we see that a small degree of chemical order increases the piezoelectric constants in PZT slightly. For cluster factors lower than -0.1 the piezoelectric coefficients drop below the values for purely random systems and continue to decrease with further ordering of the B-cations. Interestingly, the piezoelectric coefficients of random $PbZr_{0.5}Ti_{0.5}O_3$ are much larger than the values of ordered *P4mm* $PbZr_{0.5}Ti_{0.5}O_3$ (see table 6.1). This can be explained by the coexistence of multiple phases in random $PbZr_{0.5}Ti_{0.5}O_3$, which facilitates polarisation rotation and increases the piezoelectric response, compared to the single phase *P4mm* PZT. Furthermore, highly ordered systems with small cluster factors also display much larger piezoelectric constants than the ordered *P4mm* $PbZr_{0.5}Ti_{0.5}O_3$. This suggests that even a small amount of randomness in

the B-cation ordering increases the electromechanical coupling in PZT and that the specific ordering in *P4mm* $PbZr_{0.5}Ti_{0.5}O_3$ leads to poor performance.

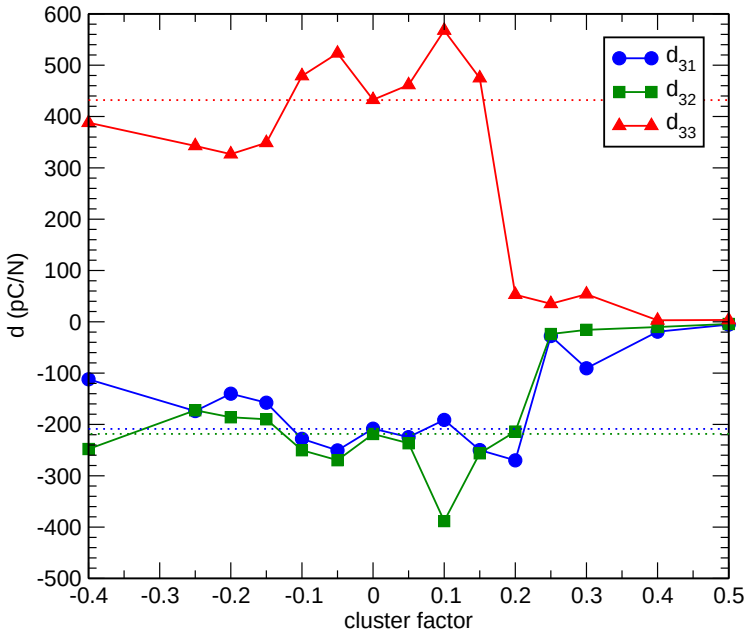

Figure 6.5: Magnitude of the piezoelectric tensor components for different cluster factors. Dotted lines represent the values at 0 cluster factor.

Small values of clustering display an increase in piezoelectric values at a cluster factor of +0.1, which in fact produces the highest d components of all the configurations with an increase of 31%. Increasing the cluster factor beyond +0.2 lowers the piezoelectric tensor to very small values (30 pC/N for d_{33} at a CF of 0.5), reducing the piezoelectric performance of PZT dramatically. This is most likely due to the complete phase separation, where antiferroelectric PZO clusters with almost zero d exist together with PTO clusters with rather small d components (see table 6.1). The piezoelectric coefficients averaged over the whole system are then even lower than the pure PTO values.

Fig. 6.6 shows the dielectric constants of PZT for different cluster factors, with the zero CF values plotted as guidance (dotted lines). The random PZT systems exhibits a ε_{33} value of 660 which overestimates the value of 450 found in morphotropic PZT thick films by experiment [128]. For small positive and negative values of the cluster factor, the behaviour is very similar to the piezoelectric tensor above, where all the components increase simultaneously. Lowering the CF below -0.1 results in a drop of the dielectric response which is recovered for more negative cluster factors (CF<0.25). In contrast to the d tensor, all dielectric coefficients in PZT with [111] ordering (CF=-0.5) are larger than

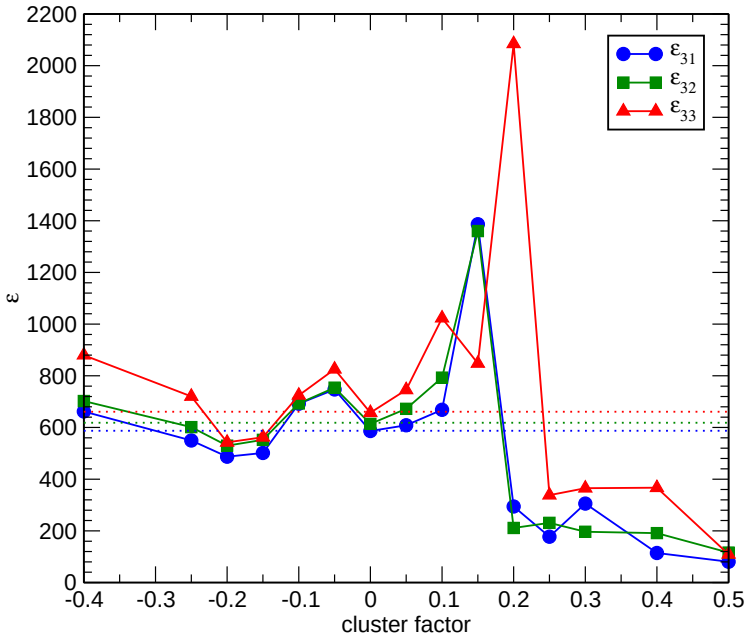

Figure 6.6: Magnitude of the dielectric tensor components for different cluster factors. Dotted lines represent the values at 0 cluster factor.

PZT with no B-cation ordering. For large positive cluster factors, ε also reproduces the significant drop in magnitude seen in the polarisation and d values. The reason, again, is the emergence of large antiferroelectric PZO clusters with a very low dielectric response. Remarkably, there is a large increase in the dielectric functions for cluster factors of 0.15 and 0.2 where ε_{33} reaches 2100, effectively tripling in value compared to the random system. This giant response induced by the small clusters is related to the change in polarisation as seen in Fig. 6.4, where P_Z vanishes and the polarisation is confined in the xy-plane.

6.5 Conclusions

Summarizing, the influence of B-cation ordering and clusters of B-cations on the stability, polarisation and the piezoelectric tensor in morphotropic PZT has been studied via MD simulations. The ordering and clustering has been introduced by biasing the placement of B-cations in MD simulations cells, so that the same ions group up (clusters) or different ions are placed as direct neighbours (ordered). The so-called cluster factor acts as a measure of this bias and helps to quantify the amount of order (negative values) and clustering (positive values).

In terms of stability, I report that both B-cation order and large clusters (segregation of PTO and PZO phases) are enthalphically favourable in the PZT solid solution. Furthermore,

B-cation order slightly decreases the magnitude of the polarisation, while large clusters decrease the polarisation by up to 30%. This structural change, depending on the cluster factor, is also reflected in the Curie temperature (T_C), which increases with increasing cluster factor, as a result of Ti rich high T_C regions.

In order to study the piezoelectric and dielectric tensors via MD simulations I evaluated that the covariance method is a suitable approach to calculate these properties during runtime. Here, I find that small amounts of B-cation ordering and clustering enhance the piezoelectric and dielectric properties of PZT. However, for larger clusters the piezo- and dielectric response drops significantly.

I conclude that avoiding the formation of large Ti and Zr clusters during synthesis of the materials retains the good overall piezoelectric and ferroelectric properties at the cost of a slightly lower T_C. Moreover, inducing small B-cation clusters or slight chemical ordering in PZT increases the piezoelectric and dielectric response while maintaining the high polarisation. The results show that the formation of clusters in $PbZr_{0.5}Ti_{0.5}O_3$ heavily influences the properties of the material. The control of the B-cation arrangement could therefore provide new pathways to control the piezoelectric performance of ceramic samples, especially in thin films, where the chemical order is driven by film- substrate interactions.

Chapter 7

Electrocaloric Effect in $Pb(Zr_{1-x}Ti_x)O_3$

The electrocaloric effect (ECE) is the change in temperature (ΔT) in a material under adiabatic conditions, when an electric field is applied (see section 2.4). Since this effect can be used to cool materials, the ECE is a promising candidate for solid state refrigeration and has been studied since the 1960's [129]. It was not until 2006, however, that Mischenko et. al [26] discovered a giant ECE in $PbZr_{0.95}Ti_{0.05}O_3$. The large ΔT of 12 K found in Zr rich $Pb(Zr_{1-x}Ti_x)O_3$ is a significant improvement over the 1-2 K found previously in ferroelectrics, and it sparked the recent interest in the ECE in ferroelectrics [23]. Subsequently, giant and moderate ECE's have been reported in classical ferroelectrics like $BaTiO_3$ [130], in relaxors [131] (see section 2.5.3) and in ferroelectric polymers [132]. The widely used $Pb(Zr_{1-x}Ti_x)O_3$ (PZT) remained an active area of research of possible ECE materials, where bilayer thin films [133] and strained thin films were also studied [134, 135]. The disorder of the B-cations that is apparent in the PZT system (see chapter 6) could further benefit the ECE, since it shortens the correlation lengths, which could possibly lead to a larger ECE [136].

In order to study the ECE from simulations, molecular dynamics (MD) can be used together with the indirect method of calculating the dependence of the polarisation (P) on the temperature and the electric field. This method, in combination with a shell model potential, has been previously applied to $LiNbO_3$ by Rose and Cohen [137], where a giant ΔT of 23 K was reported. Other theoretical methods, such as Monte Carlo simulations [129] and phenomenological modelling, have also been successfully applied to study the ECE [138].

In this chapter the shell model force field described in chapter 4 was used to study the ECE for the full range of PZT compositions with MD simulations. The end members,

$PbTiO_3$ (PTO) and $PbZrO_3$ (PZO), were included as well as several intermediate compositions of PZT. The results show that the PZT compound displays a large variance in the magnitude of the ECE, that depends on the composition and the Curie temperature.

7.1 Electrocaloric Effect from Molecular Dynamics Simulations

To model the ECE in PZT I performed MD simulations with the shell model force field described in chapter 4. Large $20 \times 20 \times 20$ supercells were used for different Ti compositions of the PZT solid solution. Specifically, I simulated the 0% (PZO), 20%, 30%, 40%, 50%, 80% and 100% (PTO) Ti compositions. For each PZT system the two types of B-cations were placed randomly over all the B-sites. Each composition was equilibrated at 200 K for 40 ps, before applying an electric field along the polar axis of the individual system. The direction of the polar axis depends on the composition and was [001] for PZO, [111] for $20\% <= x <= 50\%$ and [001] for $x >= 60\%$, where x is the amount of Ti. The strength of the applied electric field was varied from 0 to 100 MV/m. For each composition and electric field the temperature was subsequently increased in steps of 50 K to 800 K. I chose an NST ensemble with Nosé-Hoover thermostat (0.01 ps) and barostat (0.5 ps). The individual systems were equilibrated for 8 ps followed by 12 ps production over which the polarisation was calculated.

This set of simulations produces the variation of the polarisation (P) with temperature (T) for different electric fields (see Fig. 7.1), from which the differential $\frac{\partial P}{\partial T}$ can be calculated. This change of macroscopic polarisation with temperature ($\frac{\partial P}{\partial T}$) is the key quantity defining the magnitude of the ECE (change in temperature), as mentioned in section 2.4:

$$\Delta T = -\int_0^E \frac{TV}{C_{p,E}} \left(\frac{\partial P}{\partial T}\right)_E \mathrm{d}E \tag{7.1}$$

Here E is the applied electric field, T is the temperature, V is the volume of the simulation cell and $C_{p,E}$ is the specific heat capacity under constant electric field and pressure. Besides $\frac{\partial P}{\partial T}$, the other quantities can be calculated straight forwardly from the MD simulations: T and E are input parameters for the simulations and V is obtained as the average cell volume over the production run. Finally, $C_{p,E}$ was calculated as the derivative of the total energy with temperature ($\frac{\partial E_{tot}}{\partial T}$) for each electric field in the NST simulations. The derivative was calculated numerically as the slope of the linear fit to the total energy (E_{tot}) versus T data. In order to calculate the change of temperature (ΔT), equation 7.1 was integrated numerically via Simpson's rule.

7.2 $PbTiO_3$

The temperature behaviour of the polarisation for different electric fields is shown in Fig. 7.1. For zero electric field the curve displays a second order phase transition where P vanishes at the Curie temperature. The Curie temperature (T_C) at zero field is around 650 K. Increasing the electric field shifts T_C to higher temperatures as the polarisation in the material is enhanced. For larger fields no ferroelectric to paraelectric phase transition is observed in the plotted temperature range, which agrees with theoretical considerations by Liu et al. [139].

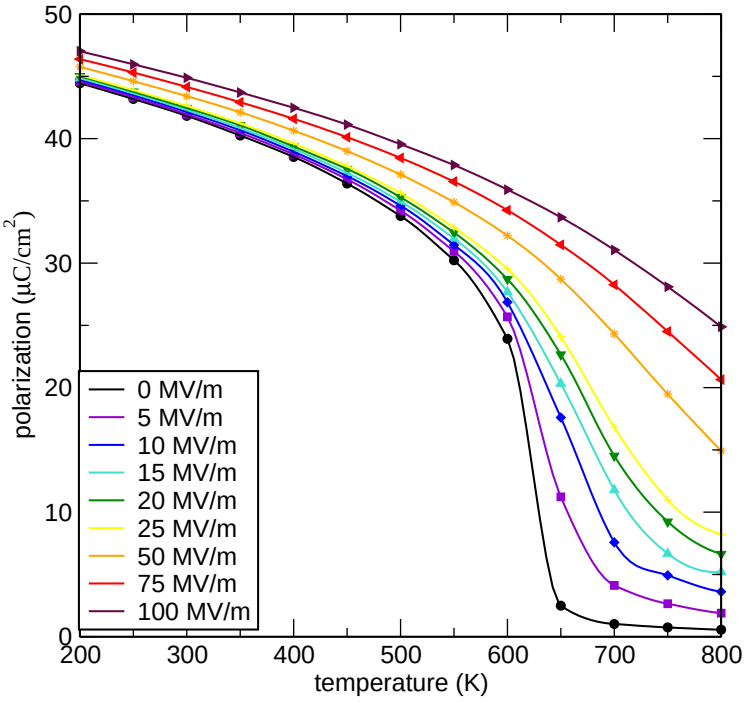

Figure 7.1: Magnitude of polarisation (P) vs. temperature (T) for different applied electric fields in $PbTiO_3$.

From the polarisation data plotted in Fig. 7.1 I calculated the derivative with temperature numerically, obtaining the temperature dependence of $\frac{\partial P}{\partial T}$ shown in Fig. 7.2. The dip in the curves, seen at all temperatures, designates the reduction of the polarisation near T_C. With higher electric fields the curve minimum shifts to higher temperatures and significantly reduces in magnitude. This corresponds to T_C shifting to higher temperatures and the polarisation curve in Fig. 7.1 becoming flatter with higher electric fields.

The change in temperature (magnitude of the ECE), as calculated by equation 7.1, is plotted in Fig. 7.3. For all electric fields there is a dominant peak near T_C, which shifts

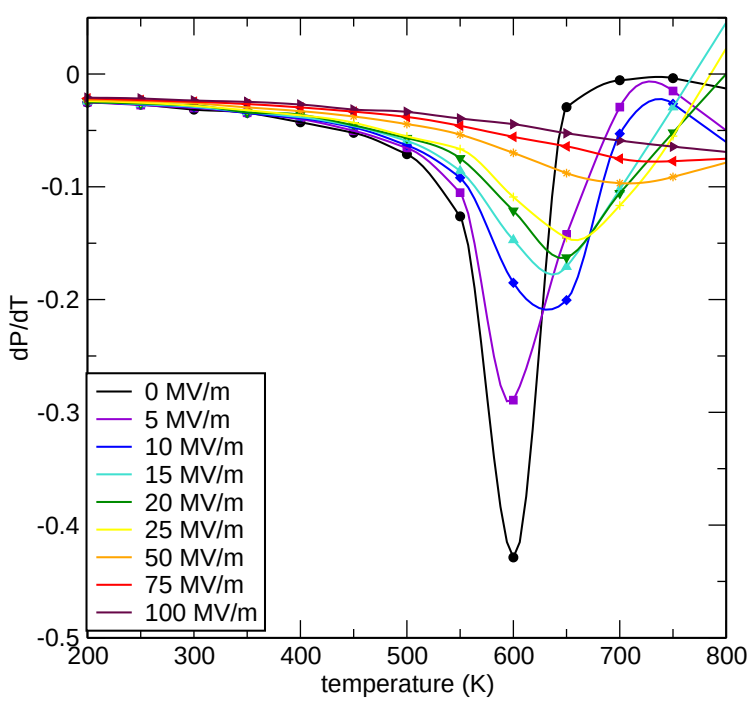

Figure 7.2: The derivative $\frac{dP}{dT}$ of the polarisation (P) with temperature (T) for different applied electric fields in $PbTiO_3$.

to higher temperatures for larger electric fields, reminiscent of the behaviour seen in Figs. 7.1 and 7.2. Clearly, applying higher electric fields leads to a larger ΔT, which is largest for 100 MV/m with a substantial value of 23 K. Even for medium electric fields the ECE is relatively large, 16 K at 50 MV/m, which is close to the giant ΔT in $LiNbO_3$ (17 K at 50 MV/m), also predicted from MD simulations [137]. Compared to $LiNbO_3$ with a T_C of 1480 K [137], the peak in ECE of PTO is at a much more accessible temperature of 650 K. Additionally, the giant ECE of 16 K is in good agreement with the 15 K calculated for PTO thin films by Landau-Devonshire thermodynamic theory at the same field of 50 MV/m [140].

7.3 $PbZr_{0.5}Ti_{0.5}O_3$

Using the same methodology as described above for PTO, I calculated the ECE in morphotropic $PbZr_{0.5}Ti_{0.5}O_3$. The results are shown in Fig. 7.4, which features very broad peaks of ΔT for all electric fields, as a result of the B-cation disorder [136] in the simulated supercell. As in PTO, the peaks shift to higher temperatures with increasing electric fields. Additionally, ΔT increases with electric fields, leading to a maximum of 11 K at 100 MV/m. A medium electric field of 50 MV/m (orange line) gives a ΔT of 6.2 K, significantly

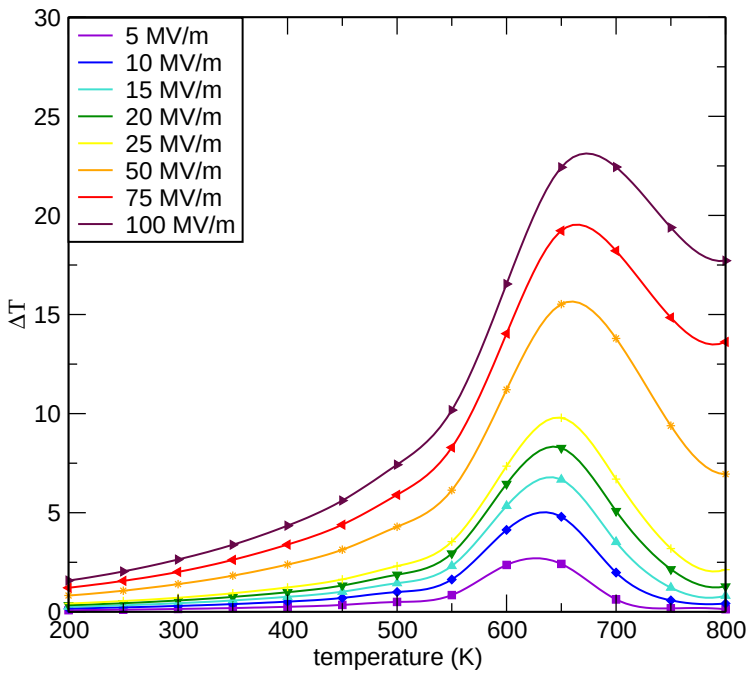

Figure 7.3: The change of temperature (ΔT) from the electrocaloric effect for different applied electric fields in $PbTiO_3$.

lower than the 16 K found in PTO. In comparison to PTO and $LiNbO_3$ [137] the ECE peaks are very broad, covering several hundred K for higher fields. These broad peaks, together with their maximum being at lower T than in PTO, might enable $PbZr_{0.5}Ti_{0.5}O_3$ for ECE applications where the temperature cannot be tightly controlled.

So far the electric field has been applied in the direction of the polarisation, e.g [001] for PTO and [111] for $PbZr_{0.5}Ti_{0.5}O_3$. In order to see whether the direction of field influences the ECE, I applied E along [001] in $PbZr_{0.5}Ti_{0.5}O_3$. For sufficiently large fields this will induce a phase transition to the tetragonal symmetry as seen in section 5.1. The ΔT of $PbZr_{0.5}Ti_{0.5}O_3$ with the external field along [001] is shown in Fig. 7.5, displaying broad peaks as in Fig. 7.4.

Remarkably, the magnitude of the ΔT is reduced compared to the [111] electric field case: At 50 MV/m along [001] I find the maximum ΔT at 5.3 K compared to 6.2 K along [111], which is a reduction of 15%. Applying the field direction along the polarisation axis seems to maximise the magnitude of the ECE in PZT. The direction of the electric field could, therefore, act as a tuning knob for the ECE, at least in the studied mono domain systems with uniform polarisation direction.

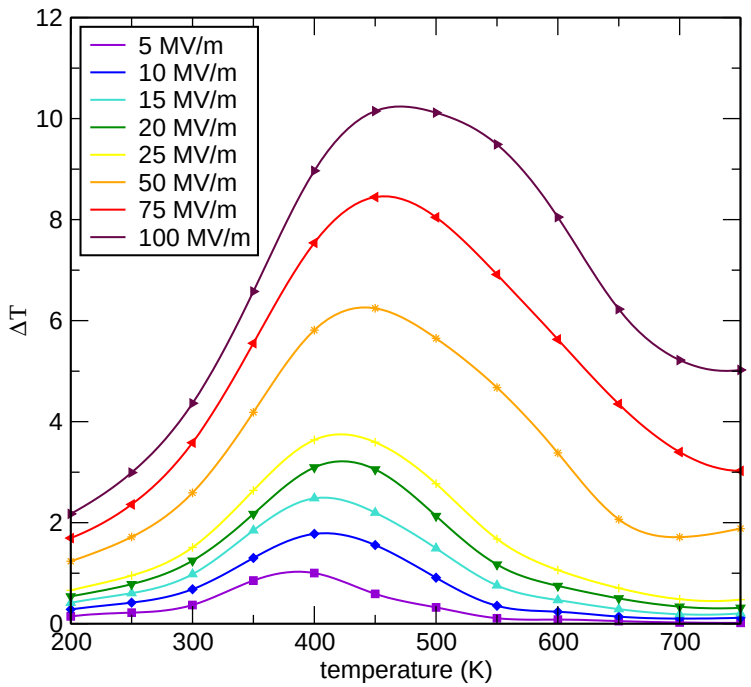

Figure 7.4: The change of temperature (ΔT) from the electrocaloric effect for different applied electric fields (along [111]) in $PbZr_{0.5}Ti_{0.5}O_3$.

7.4 $PbZr_{0.7}Ti_{0.3}O_3$

Besides the morphotropic $PbZr_{0.5}Ti_{0.5}O_3$, I investigated the ECE in the Zr rich parts of the phase diagram of PZT. The ΔT of rhombohedral $PbZr_{0.7}Ti_{0.3}O_3$ is shown in Fig. 7.6, where we see the familiar peaks of ΔT with increasing magnitude, as the electric fields get larger. Compared to PTO in section 7.2, ΔT only drops slowly for higher temperatures above T_C and for higher fields. As in $PbZr_{0.5}Ti_{0.5}O_3$ the area of the large positive ECE is very broad and spans hundreds of Kelvin. The peak ECE is significantly reduced compared to $PbZr_{0.5}Ti_{0.5}O_3$ with 3.5 K at 50 MV/m at a T_C of about 350 K.

7.5 $PbZr_{0.8}Ti_{0.2}O_3$

Increasing the Zr content further to $PbZr_{0.8}Ti_{0.2}O_3$, leads to narrower ECE peaks compared to $PbZr_{0.7}Ti_{0.3}O_3$, as seen in Fig. 7.7. Here, the maximum ECE occurs around the T_C of 350 K and the ΔT drops slowly for temperatures above the Curie temperature.

Noteworthy, I find a distinct behaviour for small electric fields below 50 MV/m: Below T_C the ΔT is negative for these low electric fields. This produces a negative ECE of -0.7 K at around 220 K for 25 MV/m. With higher temperature the negative ECE transitions to a positive effect above T_C, where it has a maximum of 1.7 K for 25 MV/m. This negative

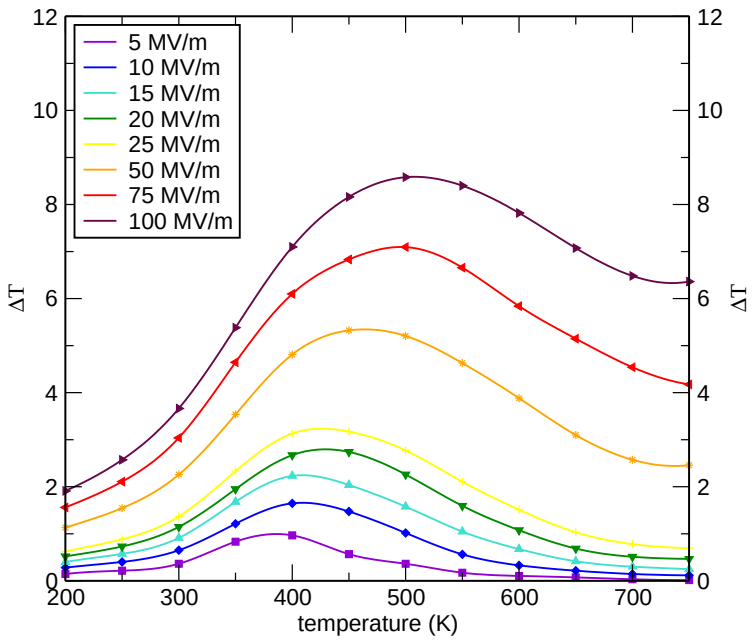

Figure 7.5: The change of temperature (ΔT) from the electrocaloric effect for different applied electric fields in $PbZr_{0.5}Ti_{0.5}O_3$. Here, the electric field is applied along [001], whereas the polarisation direction of $PbZr_{0.5}Ti_{0.5}O_3$ is along [111].

ECE, with its crossover to the conventional positive ΔT, is a result of the antiferroelectric state, which I find at zero field and low temperatures in PZT with a Zr content over 80%. Experimentally, the antiferroelectric phase only exists up to 5% Ti in PZT [33], however, this compositional phase transition is shifted to about 15%-20% Ti in the used shell model potential. This means that the $PbZr_{0.8}Ti_{0.2}O_3$ composition in the simulations corresponds to the experimental $PbZr_{0.95}Ti_{0.05}O_3$, for which the giant ECE of 12 K has been reported [26].

It has been suggested that the reason for the large ΔT was the phase transition with field and temperature between the ferroelectric and the antiferroelectric phases at this composition, leading to a large change in P with those variables (E and T) [26]. In the MD simulations, where I sample the same region of phase coexistence at $PbZr_{0.8}Ti_{0.2}O_3$, I report a moderate value of 3.55 K at 50 MV/m. This is significantly lower than the 12 K at 48 MV/m found in $PbZr_{0.95}Ti_{0.05}O_3$ [26], but only slightly larger than the ECE I find in $PbZr_{0.7}Ti_{0.3}O_3$. The phase coexistence, therefore, does not seem to enhance the ECE. Furthermore, the difference in ΔT between the experiments and the simulations might be overestimated, since the experiments found the maximum response near the T_C of 495 K

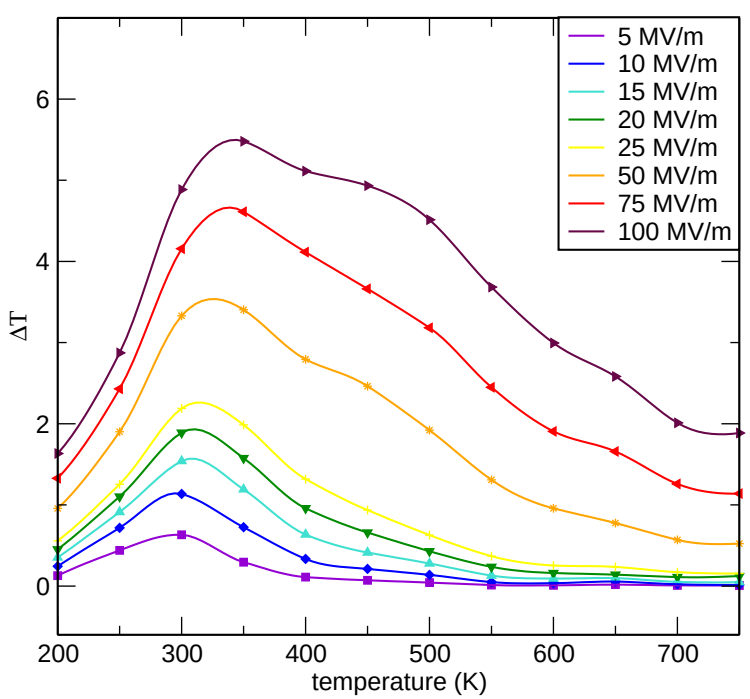

Figure 7.6: The change of temperature (ΔT) from the electrocaloric effect for different applied electric fields in $PbZr_{0.7}Ti_{0.3}O_3$.

[26], while T_C for $PbZr_{0.8}Ti_{0.2}O_3$ in the simulations is much lower with 350 K. The negative change in temperature I report in $PbZr_{0.8}Ti_{0.2}O_3$ at low fields has been recently confirmed experimentally in antiferroelectric [138, 27], and I will discuss this further with the example of PZO in the next section (7.6).

7.6 $PbZrO_3$

The antiferroelectric $PbZrO_3$ (PZO) shows a distinct relationship of the polarisation with temperature (see Fig. 7.8), which contrasts the behaviour seen in ferroelectric PTO and PZT (section 7.2 and 7.3). We see that for zero field orthorhombic PZO has a polarisation very close to 0, as expected for an antiferroelectric (AFE). However, the applied electric fields induce a polarisation in PZO, which peaks around the PZO Curie temperature at 400 K. Clearly, larger fields induce larger P in the material, but interestingly the polarisation peak shifts to lower temperatures with increased fields. This is in opposition to the ferroelectric materials studied above, where larger fields shift T_C to higher temperatures. Here, increasing the field pushes the phase transition to lower temperatures. A second difference to PTO and PZT is evident from Fig. 7.8, in that the slope of $\frac{\partial P}{\partial T}$ changes sign with temperature. For ferroelectrics, P drops monotonically with the temperature, while for PZO the polarisation

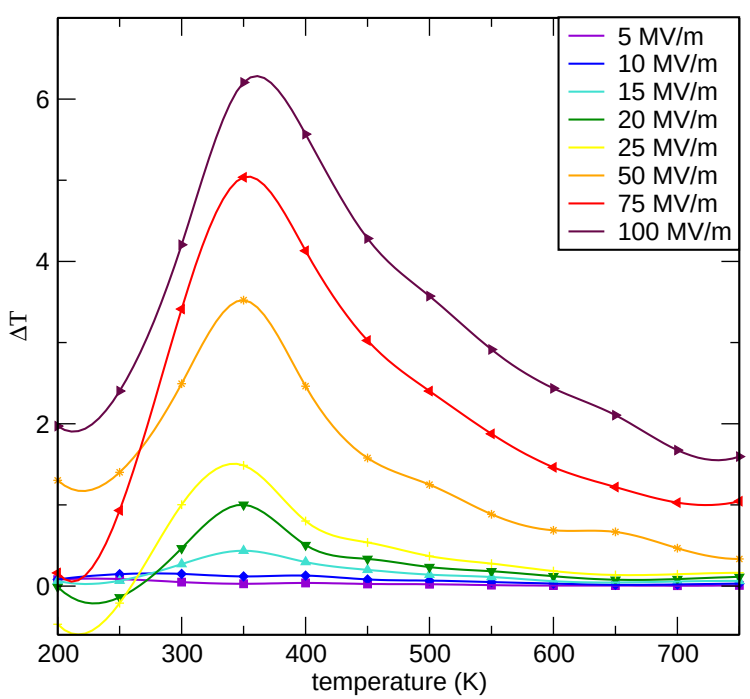

Figure 7.7: The change of temperature (ΔT) from the electrocaloric effect for different applied electric fields in $PbZr_{0.8}Ti_{0.2}O_3$.

increases up to T_C and decreases above. This behaviour is similar to phenomenological calculations based on the Kittel model that have recently been published [138].

Plotting $\frac{\partial P}{\partial T}$ in Fig. 7.8 further highlights the difference between AFE PZO and the ferroelectric materials. Here we see how the differential changes sign around T_C from positive to negative values. Note, that the positive values are larger than the negative ones and that $\frac{\partial P}{\partial T}$ increases with larger applied fields.

The change in temperature (ΔT) for PZO is shown in Fig. 7.10. The ECE for temperatures below T_C is negative and peaks at -0.7 K for the 50 MV/m curve. Above T_C, ΔT is positive everywhere with a maximum of 0.6 K for 50 MV/m (orange curve). Remarkably, ΔT drops only slowly with higher temperature, similar to what we have seen in the disordered PZT (section 7.3). The crossover of the ECE from negative to positive values occurs around T_C and the magnitude of the effect seems to be very similar on either side of the phase transition. The negative ECE reported here, has been modelled and subsequently measured in PZO ceramics [138]. The MD simulations further confirm the crossover from negative to positive ΔT around T_C, which is attributed to the phase change from the AFE to the FE state [138].

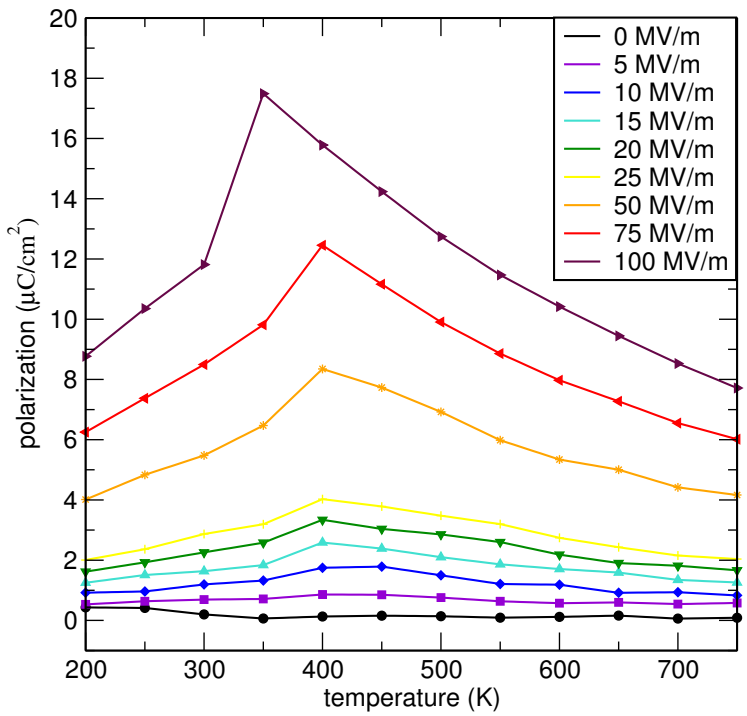

Figure 7.8: Magnitude of polarisation (P) vs. temperature (T) for different applied electric fields in antiferroelectric $PbZrO_3$.

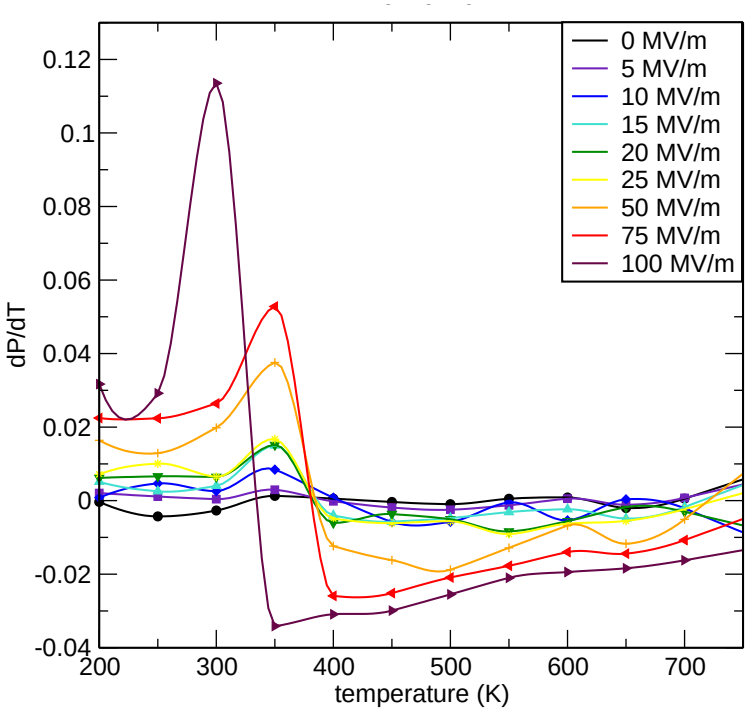

Figure 7.9: The derivative $\frac{dP}{dT}$ of the polarisation (P) with temperature (T) for different applied electric fields in antiferroelectric $PbZrO_3$.

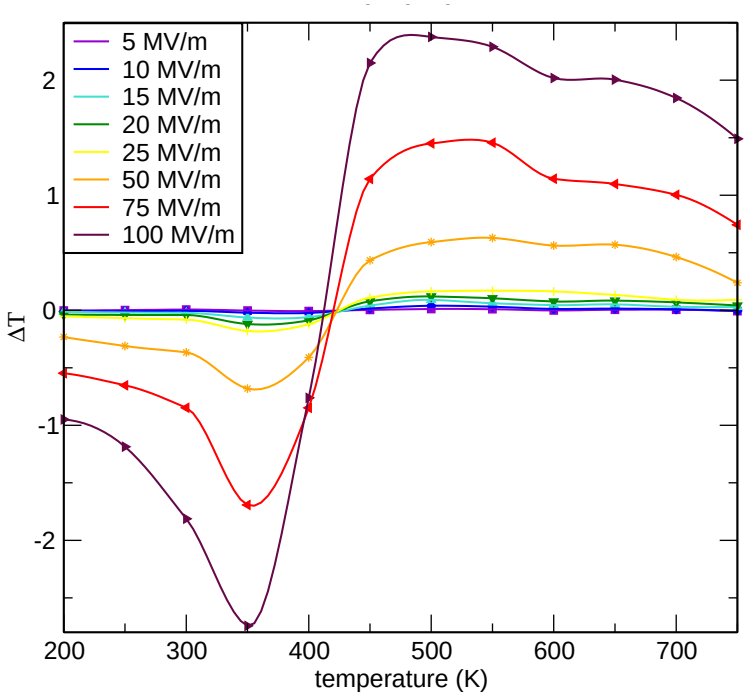

Figure 7.10: The change of temperature (ΔT) from the electrocaloric effect for different applied electric fields in antiferroelectric $PbZrO_3$.

7.7 Compositional Dependence of the Electrocaloric Effect in $Pb(Zr_{1-x}Ti_x)O_3$

Besides the compositions discussed in the previous sections: 0%, 20%, 30%, 50% and 100% Ti, I also studied the ECE in PZT with 40% and 80% Ti. The 40% Ti composition shows a very similar behaviour of ΔT than $PbZr_{0.5}Ti_{0.5}O_3$ with broad peaks. 80% Ti produces a similar ECE behaviour as PTO, although with a lower magnitude of ΔT.

To compare the ECE of the different compositions, the maximum ΔT at 50 MV/m was plotted against the T_C in Fig. 7.11. As seen in section 4.2.3, T_C increases with Ti content across the PZT solid solution. This is reflected in Fig. 7.11: The first two dots (near identical positions) are 20% and 30% Ti. With increasing T_C we then have 40%, 50%, 80% and 100% Ti (PTO), in that order.

Clearly, ΔT increases with increasing T_C and reaches its maximum for PTO. This can be explained with equation 7.1, in which the temperature appears as a linear term. Rose and Cohen [137] suggest that the ECE is highest around T_C, which means that a higher Curie temperature will lead to a higher maximal ΔT (at that T_C). Regarding PZT and Fig. 7.11, we therefore see the Ti rich part of the phase diagram outperforming the Zr rich part with

lower T_C.

Unfortunately, the benefit of the giant ECE of PTO with its high T_C is limited by the high temperatures required to achieve the maximum ΔT (T_C=650 K for the force field and 790 K from experiments [33]). In order to engineer devices using the ECE near room temperature, materials with a lower T_C or a large ΔT at reduced T are more suitable. Comparing the ΔT at a lower temperature of 350 K, I find that $PbZr_{0.8}Ti_{0.2}O_3$ shows the highest magnitude of the ECE for all tested compositions. This is due to ΔT dropping quickly below T_C for all compositions, making the 20/80 composition preferential at lower temperatures with its T_C at 350 K.

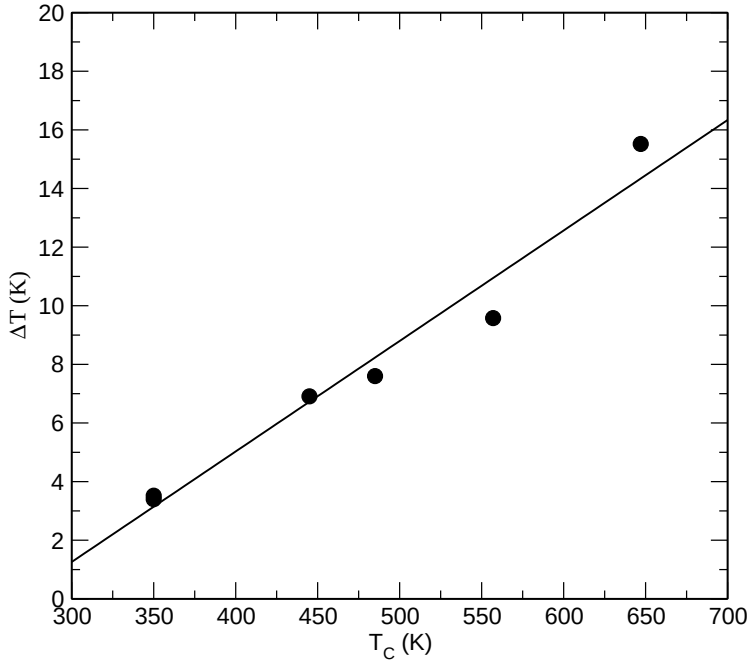

Figure 7.11: The change of temperature (ΔT) from the electrocaloric effect at a field of 50 MV/m versus the Curie temperature (T_C) in $Pb(Zr_{1-x}Ti_x)O_3$.

Note, that the force field underestimates the Curie temperature of PZT and the actual T_C of $PbZr_{0.8}Ti_{0.2}O_3$ is around 520 K [33], therefore far above room temperature. Nevertheless, $PbZr_{0.8}Ti_{0.2}O_3$ seems to be a good candidate for applications of the ECE with its sizeable ΔT at slightly elevated temperatures and the occurrence of a negative ECE below T_C. The coexistence of the antiferroelectric and the ferroelectric phase I report at the 20/80 composition in the force field (see section 7.5) is found experimentally around $PbZr_{0.95}Ti_{0.05}O_3$ and is believed to be the reason of the giant ECE found in Zr rich PZT [26]. Tuning of the composition could, therefore, be beneficial to further increase the ECE in Zr rich PZT and

to match its ΔT peak to the desired temperature.

7.8 Conclusions

In this chapter, the electrocaloric effect in a broad range of PZT compositions was studied with MD simulations. MD simulations can be used to indirectly calculate the change of temperature in the material by an applied electric field. For this I calculated the polarisation as a function of temperature and electric field, which in combination with equation 7.1 was used to quantify the ECE in the ferroelectric and, in the case of PZO, antiferroelectric materials.

First, I quantified the ECE in PTO which shows a second order phase transition with temperature at zero field. Upon application of electric fields along the polar axis, T_C shifts to higher temperatures with increasing fields. Calculating ΔT for different fields, I then found that PTO exhibits a giant ECE of 16 K at an applied field of 50 MV/m, which surpasses the ΔT found experimentally in $PbZr_{0.95}Ti_{0.05}O_3$ (12 K at 48 MV/m) [26] and is comparable to the 17 K found $LiNbO_3$ [137] (17 K at 50 MV/m) from MD simulations. Furthermore, this result also agrees well with the ΔT of 15 K at 50 MV/m calculated by Landau-Devonshire thermodynamic theory [140], which demonstrates that these two theoretical methods deliver comparable results regarding the ECE.

Second, the ECE in $PbZr_{0.5}Ti_{0.5}O_3$ was calculated where I found a ΔT of 6.2 K at 50 MV/m, which is significantly lower than for PTO or for $PbZr_{0.95}Ti_{0.05}O_3$ thin films [26]. The maximum ΔT appears at around the T_C of 450 K, which is 200 K below the highest electrocaloric response in PTO at 650 K. Interestingly, I find that the ΔT peaks are very broad in $PbZr_{0.5}Ti_{0.5}O_3$ compared to PTO, as they span up to 200 K. This broadening of the peaks appears most likely due to the B-cation disorder in PZT, which reduces the dipole correlation length in the material. The fact that the ECE has significant values of several K for a range of over 200 K in $PbZr_{0.5}Ti_{0.5}O_3$ could be exploited in devices that experience large temperature variations.

The Zr rich part of the phase diagram has been sampled with $PbZr_{0.7}Ti_{0.3}O_3$, $PbZr_{0.8}Ti_{0.2}O_3$ and PZO. For $PbZr_{0.7}Ti_{0.3}O_3$ I find broad ECE peaks similar to $PbZr_{0.5}Ti_{0.5}O_3$, albeit with a lower maximum ΔT of 3.5 K at 50 MV/m and 350 K. $PbZr_{0.8}Ti_{0.2}O_3$, which has comparable properties to experimental $PbZr_{0.95}Ti_{0.05}O_3$ thin films, as both materials lie at the curve of coexistence between antiferroelectric and ferroelectric phases, shows only a minute improvement over $PbZr_{0.7}Ti_{0.3}O_3$. This means that

being at a region of phase coexistence in PZT does not increase the ΔT significantly, as suggested by Mischenko et al. [26]. I further investigated the antiferroelectric state by studying PZO, where I find a crossover from a negative ECE at low temperatures to a positive ECE at higher temperatures, which agrees well with recent theoretical and experimental work on PZO [138].

Regarding all the considered PZT compositions together in the last section, I can confirm the findings of Rose et al. [137] that the maximum ΔT is found close to T_C in ferroelectrics. Furthermore, I report that the magnitude of the ECE increases with T_C and therefore with the Ti content in PZT, where PTO shows the largest ECE of all compositions. If one is after an electrocaloric material that performers well at a lower temperature, then $PbZr_{0.8}Ti_{0.2}O_3$ shows the largest ΔT at a temperature of 350 K over the whole PZT solid solution.

To conclude, I find a trade-off in the PZT solid solution, which might be generic for all ferroelectrics, where a large ECE is accompanied with a large T_C and therefore requires high operating temperatures. Nevertheless, $Pb(Zr_{1-x}Ti_x)O_3$ offers a great variability in Curie temperatures and in ECE magnitude, which allows for compositional engineering of materials for electrocaloric applications.

Chapter 8

Charged Domain Walls and Defects in $PbTiO_3$

Piezoelectric materials that couple mechanical strain to electrical polarisation are widely used in transducers, IR-sensors and actuators. Traditionally, efforts to enhance the piezoelectric properties are focused on increasing the intrinsic piezoelectric effect in such ceramics. However, recent research suggests that not only the bulk response, but also the effect of charged domain walls, could offer great potential to improve the piezoelectric response of these materials (see section 2.3). Charged domain walls (DWs) form when two ferroelectric domains meet "head-to-head" or "tail-to-tail", so that the polarisation charge accumulates at the domain wall. Although electrostatically unfavourable, the existence of those walls has been confirmed experimentally [20].

To study charged domain walls with a classical shell model force field is challenging, since there are no electronic degrees of freedom in that model that would allow the accurate simulation of the charge compensation through defects or free carriers. Density functional theory (DFT), on the other hand, has been previously applied to study head-to-head and tail-to-tail walls in the prototypical ferroelectric material $PbTiO_3$ (PTO). In a first paper, Wu and Vanderbilt [141] studied a charged 180° domain wall, which was stabilised by a Sc^{3+}/Nb^{5+} defect pair. More recently, Rahmanizadeh et al. [142] studied a similar system of PTO with DFT+U and included a fluorine impurity. Both studies report that charge compensation via defects is necessary to prevent the system from being metallic and unstable [141, 142].

In this chapter, I further investigate the defect mediated stabilisation of charged domain walls in PTO, by studying 90° domain walls using DFT. First, defect free bulk PTO is characterized via DFT. I then analyse the influence of common point defects in the PTO

ceramic, such as oxygen or lead vacancies, on the structure of bulk PTO. Third, the structure and the stability of 90° and 180° domain walls is discussed. In the last section, I then combine 90° domain walls with point defects to finally create charged 90° domain walls in a ferroelectric.

8.1 *Ab initio* Calculations of Structure and Electronic Properties of $PbTiO_3$

As a first step in the analysis of the properties of domain walls and defects in PTO, bulk PTO was characterised with *ab initio* calculations. All calculations, were performed in CASTEP 8.0 with the Wu-Cohen (WC) GGA functional [1]. The WC functional is known to give good structural results for ferroelectrics but it systematically underestimates the band gap [96]. Too small values of band gaps are a common issue of LDA and GGA functionals and is often referred to as the band gap problem [143]. More accurate methods exist that give improved band gap values, such as hybrid functionals, which combine exact Hartree-Fock exchange with DFT. However, hybrid density functionals are computationally more expensive by about an order of magnitude, which makes calculations of larger systems with domain walls infeasible. Therefore, WC GGA was selected for the calculations, since it provides a good compromise between accuracy and efficiency, as shown by the results in this section.

In more detail, ultra soft pseudo potentials (USPPs) generated on the fly by CASTEP [75] were chosen, together with a plane-wave cut-off of 700 eV. The Brillouin zone was sampled densely with a $8 \times 8 \times 8$ Monkhorst pack k-point grid per conventional unit cell for the structural relaxations. The calculations of the electronic density of states (DOS) was performed with an increased k-point grid of $13\times 13\times 13$ k-points per conventional unit cell. The atomic positions were optimised during the structural relaxations until the Hellmann-Feynman forces were below 0.005 eV/Å. Unless directly specified in the relevant sections, full geometry optimisations were performed. This includes relaxations of the cell vectors until the maximum stress component was below 0.1 GPa.

8.1.1 Cubic $PbTiO_3$

The lattice parameter of cubic PTO (space group $Pm\bar{3}m$) was calculated to be $a = 3.918$ Å, with a cell volume of $V = 60.15$ Å^3. This agrees well with previous all-electron WC calculations on cubic PTO reporting $a = 3.923$ Å [96] and the experimental lattice parameter measured at room temperature of $a = 3.96$ Å [144].

The Born-effective charges (Z^*) were calculated for the optimised cubic structure. Density functional perturbation theory (DFPT), as implemented in CASTEP, was used to calculate the linear response of PTO to an electric field and to obtain the Z^*. However, DFPT is not available for ultra soft pseudo potentials in CASTEP 8.0. In order to employ

Table 8.1: Born-effective charges of of cubic $PbTiO_3$ calculated with the Wu and Cohen [1] (WC) functional (this work) and with the PBEsol functional [2].

	present work (WC)	reference (PBEsol) [2]
$Z^*(Pb)$	3.92	3.90
$Z^*(Ti)$	7.10	7.10
$Z^*(O \parallel)$	-2.58	-2.58
$Z^*(O \perp)$	-5.85	-5.86

this functionality for PTO, I switched to norm-conserving pseudo potentials, together with a much higher plane wave cut-off of 1400 eV. The use of the norm-conserving potentials allowed us to calculate the Z^*, which are reported in table 8.1. Although the Z^* were calculated for lattice parameters obtained from different pseudo potentials, they are in excellent agreement with Z^* obtained from the PBEsol GGA functional in a recent work [2]. We see that for each ion the Z^* exceed their formal charges (Pb: +2, Ti: +4, O: -2) by a significant amount, which is characteristic of ferroelectric materials.

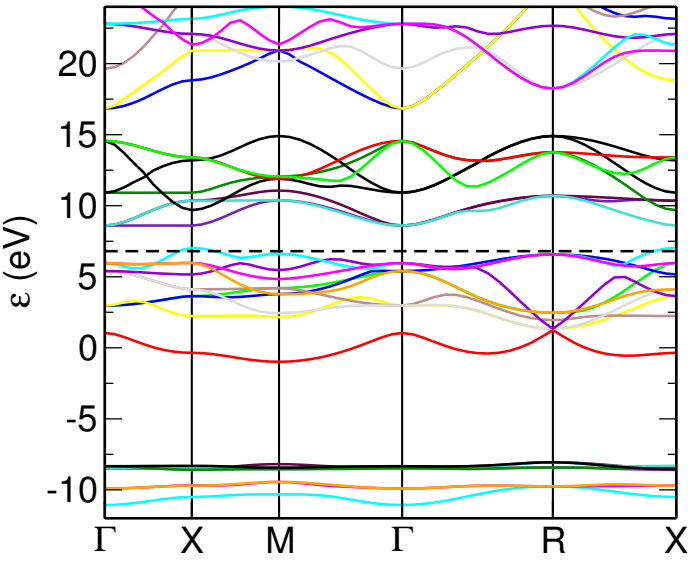

Figure 8.1: Calculated electronic band structure of cubic $Pm\bar{3}m$ $PbTiO_3$ along the high symmetry points. The dotted line indicates the Fermi energy (E_F).

Besides the structural parameters of PTO, I calculated the electronic band structure as seen in Fig. 8.1. The band structure was calculated along the high symmetry points of

the Brillouin zone for cubic PTO in the $Pm\bar{3}m$ space group. The band structure shows that PTO has an indirect band gap, where the top of the valence band (VB) is at X, while the bottom of the conduction band (CB) is at Γ. Overall the dispersion corresponds to the band structure reported for PBEsol [2]. The electronic band gap is 1.64 eV which is expectedly smaller than the experimental band gap of 3.4 eV [145].

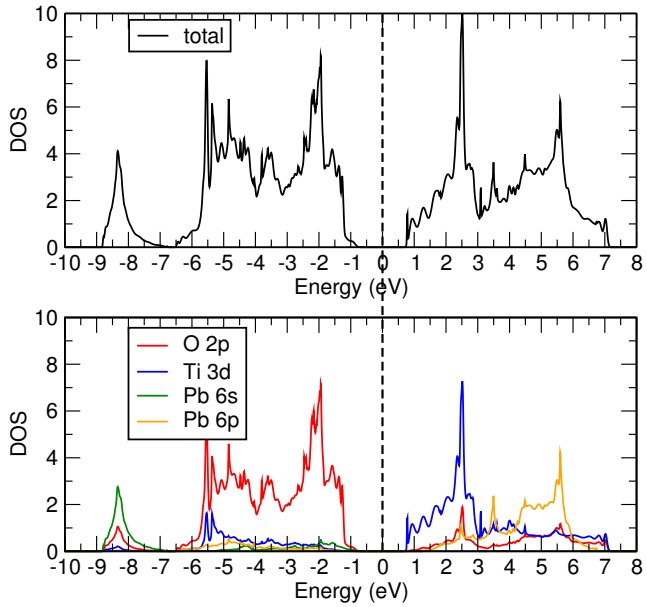

Figure 8.2: Density of states (DOS) (upper) and projected DOS (lower) of cubic $PbTiO_3$.

The electronic density of states (DOS) is shown in Fig. 8.2 as total DOS and projected DOS (PDOS) for a few selected orbitals. The analysis of the electric structure of PTO (see Fig. 8.2) demonstrates that the top of the conduction band is mostly formed by O 2p states and contains a contribution of the Pb lone pair. This is a well known effect in Pb-containing perovskites materials, where the high piezo- and ferroelectric response is believed to originate from the redistribution of the electron density related to the Pb lone pair [146]. The bottom of the conduction band consists mostly 3d states of Ti.

8.1.2 Tetragonal $PbTiO_3$

The optimised lattice parameters for tetragonal *P4mm* $PbTiO_3$ are $a = 3.867$ Å and $c = 4.214$ Å with a cell volume of $V = 63.00$ Å^3. This agrees well with all electron WC calculations [96], but overestimates the c/a ratio of experimental results [77] (1.088 vs. 1.071). This enhanced tetragonality (c/a ratio) is common for GGA calculations on perovskites [96]. Additionally, the spontaneous polarisation (P) of PTO was calculated via $P_i = Z^*_{ij} u_j$, with u_j being the ferroelectric displacements of atom j and with Z^* obtained for

cubic PTO in table 8.1, which gives a value of 113.2 $\mu C/cm^2$. This value overestimates the experimental P that reaches values between 20 $\mu C/cm^2$ and 100 $\mu C/cm^2$ [4], depending on the sample preparation. Again, this overestimation is common for GGA functionals and stems from the enhanced tetragonality of the tetragonal phase. The energy difference between the cubic and the tetragonal phase is 78.8 meV, with the tetragonal phase being lower in energy, which agrees with the 99.7 meV found in previous WC calculations [96]. The DOS of the tetragonal phase shown in Fig. 8.3 shows similar features to that of cubic PTO. Indeed the top of the VB is formed by the 2p states of O, while bottom of the CB is predominately formed by the 3d states of Ti. Remarkably, the band gap in tetragonal PTO is 1.74 eV which is 0.1 eV larger than in cubic PTO. This increase of the band gap is probably due to the splitting of the Ti t_{2g} states in the tetragonal symmetry.

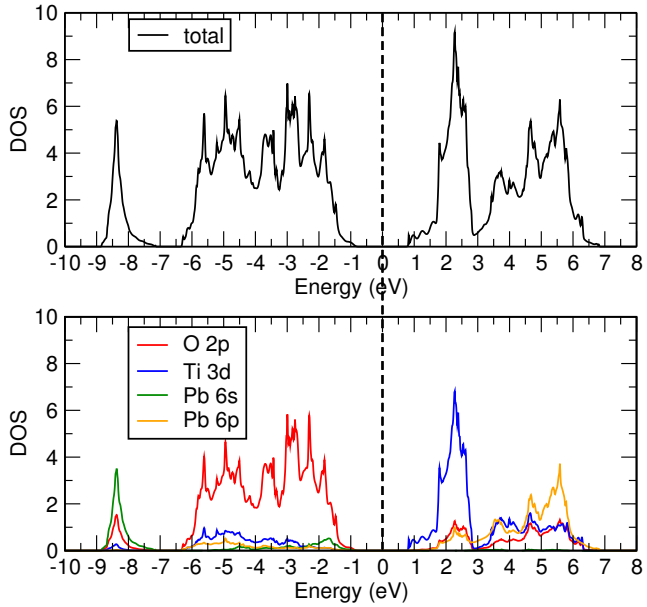

Figure 8.3: DOS (upper) and projected DOS (lower) of tetragonal $PbTiO_3$.

Overall I find that the structure, the Born-effective charges, the electronic structure and the energy difference of the two phases of PTO are well reproduced with the WC GGA functional and the CASTEP USPPs. The shortcomings of the choice of this potential are a slight overestimation of the tetragonality and the significantly reduced band gap. Since this chapter does not present a complete analysis of electronic properties, but rather a qualitative comparison of the effect of point defects and domain walls on the electronic structure and the polarisation in PTO, I continue to choose the WC functional in the next sections.

8.2 Defects in Bulk $PbTiO_3$

In order to stabilise charged domain walls in PTO, the polarisation charge at the wall needs to be compensated [147]. This compensation can be achieved by point defects, either as vacancies or as substitutions. In this section the structure and DOS of several defects (neutral oxygen vacancy, lead vacancy, niobium substitution, scandium substitution and iron substitution of titanium) in tetragonal bulk PTO, that might help stabilising charged DWs, were calculated. The same computational details as described in 8.1 were applied. Both, the vacancies and the B-cation substitutions were calculated in a 3x3x3 tetragonal supercell (135 atoms in the non-defective cell), where atomic positions were optimised until the forces were below 0.005 eV/Å and the cell vectors were optimised until the pressure was below 0.1 GPa. All supercells were uncharged, as a single atom was removed without compensating the charge in any form. I approximated the defect formation energy (ΔE_f) as follows:

$$\Delta E_f = E_{tot}^{def} - (E_{tot}^{bulk} - E_{tot}^{atom}), \tag{8.1}$$

where E_{tot}^{def} is the total energy of the system with the defect, E_{tot}^{bulk} is the total energy of the perfect bulk system and E_{tot}^{atom} is the total energy of the isolated defect atom. In case of the substitutions of the Ti atom, E_{tot}^{Ti} was added to eq. 8.1. For Pb, Nb, Sc, Fe and Ti E_{tot}^{atom} was calculated with the single atom in a 22 Å×22 Å×22 Å cell. For O half of the energy of an O_2 dimer (O in triplet state) in a 22 Å×22 Å×22 Å cell was taken as the single atom energy. The box length of 22 Å was chosen after a series of convergence tests to reduce the error in total energy below 10^{-5}.

8.2.1 Oxygen Vacancy in $PbTiO_3$

8.2.1.1 Axial Oxygen Vacancy

Two inequivalent O vacancy (V_O) positions exist in tetragonal PTO: axial and in-plane. I first discuss the axial case, where the O atom is removed from the Ti-O-Ti chain along the polar c axis. Such a neutral V_O, also called an F-centre, is one of the most common defects in oxides [148]. Creating this defect results in the neighbouring Ti atoms moving away from the vacancy with a displacement of 0.18 Å for the Ti on top and 0.09 Å for the Ti below. The relaxation of Ti is the largest of all atoms, and followed by a 0.12 Å displacement of the 4 nearest neighbour Pb atoms, which all displace towards the O defect. Interestingly, the Pb atoms move towards the defect and against the Coulomb repulsion between their outer

shell electrons and the electron density at the vacancy site. This is explained by the large size of the Pb atoms, which makes them fill the empty space generated by the O vacancy [149]. The neighbouring O atoms only shift about 0.03 Å along the z-axis and do not contribute much to the total displacement. The displacements of the closest atoms to the O defect are visualized in Fig. 8.4 and qualitatively agree with a Hartree-Fock (HF) study on PTO [149]. However, I report an outwards displacement of the bottom Ti atom, which contrasts the calculation by Stashans et. al. [149]. This difference is probably due to the different lattice parameters produced by the different methods (GGA vs. HF), which will allow for different atomic relaxations.

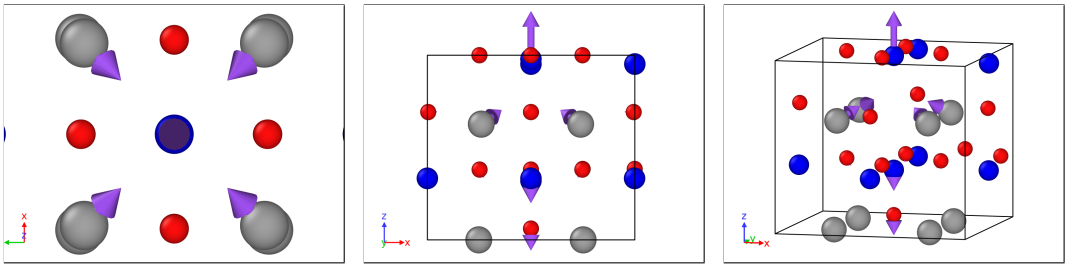

Figure 8.4: Displacement field around the axial oxygen vacancy in top (left), side (middle) and perspective view (right). Pb atoms are shown in grey, Ti in blue and O in red, with purple arrows indicating the direction of the displacements.

The total DOS and the PDOS were calculated for the neutral axial oxygen vacancy and are shown in Fig. 8.5 (left). The defect state at the bottom of the CB is well localised at the vacancy site and formed by the t_{2g} states of Ti. I find that the defect state is split from the CB by 0.48 eV, whereas a previous hybrid DFT study reports the defect level to be split of the CB by 0.97 eV [150]. This a known shortcomming of GGA functionals, which underestimates the split from the bottom of the conduction band [151]. Nevertheless, the WC functional shows that the neutral oxygen vacancy introduces a donor level into the band gap, by leaving two electrons at the vacancy site. The fact that a V_O acts as an electron donor can be used to compensate the polarisation at charged domain walls.

The highest occupied molecular orbital (HOMO), corresponding to the vacancy level, is shown in Fig. 8.7 left. The defect state is centred on the vacancy and the closest Ti atom, with the shape of the wavefunction indicating mostly a d_{z^2} character. Recent hybrid DFT calculations show a similar defect state due to an axial O vacancy in PTO, and the authors suggest that the d_{z^2} shape stems from the ruptured bond between the Ti 3 d_{z^2} and O 2p

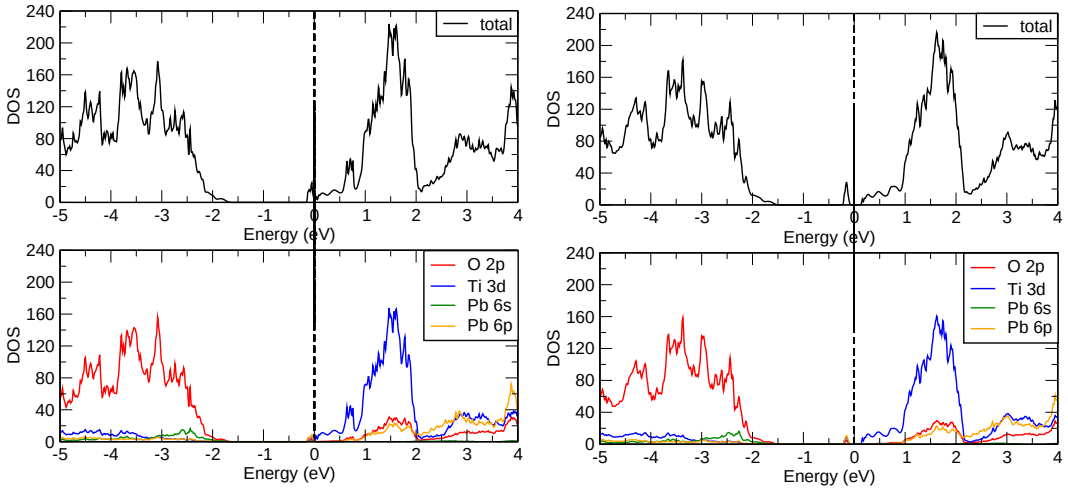

Figure 8.5: DOS (upper) and projected DOS (lower) of tetragonal $PbTiO_3$ with a single oxygen vacancy (V_O) in axial position (left) and in in-plane position (right).

orbitals [152].

8.2.1.2 In-Plane Oxygen Vacancy

A neutral in-plane oxygen vacancy has been created by removing an oxygen from the Ti-O-Ti chain along the x-axis. The structural relaxations of the neighbouring atoms of the vacancy are distinct from the axial V_O case and they are visualised in Fig. 8.6. Here, the largest movement stems from the Pb atoms above the V_O, which shift towards the vacancy by 0.15 Å. The Pb atoms below the vacancy move only slightly towards the defect. For the Ti atoms only the two closest ions are affected, which move away from the defect with a displacement of 0.12 Å. As for the axial vacancy, the neighbouring O ion only show small displacements towards the V_O.

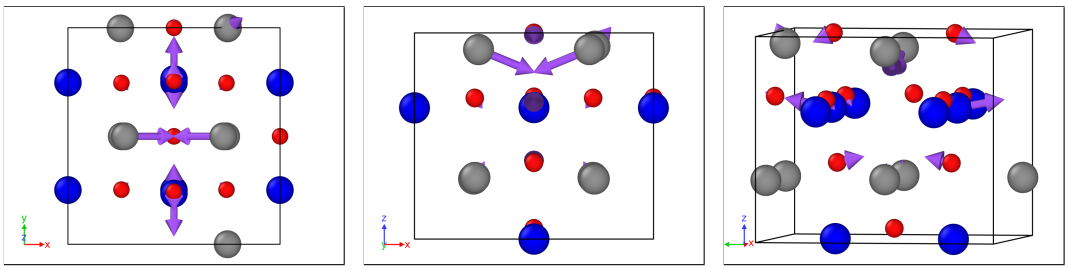

Figure 8.6: Displacement field around the in-plane oxygen vacancy in top (left), side (middle) and perspective view (right). Pb atoms are shown in grey, Ti in blue and O in red, with purple arrows indicating the direction and magnitude of the displacements.

The total and the projected DOS of the in-plane V_O, as seen in Fig. 8.5 right, looks

very similar to the DOS of the axial V_O (Fig. 8.5 left). Here, the defect level of the O vacancy is split from the bottom of the CB by 0.53 eV. The occupied defect state is plotted in Fig. 8.7 right. Here, no d_{z^2} character is visible, compared to the axial V_O. This is due to the in-plane vacancy breaking the in-plane bond between Ti and O, where there is no d_{z^2} contribution. However, the Pb s character of the defect state wavefunction is larger in this type of oxygen vacancy. Besides the small differences in the shape of the defect state, both types of V_O have donor levels close to the edge of the CB and their defect states are localised on the vacancy and the nearest Ti atom.

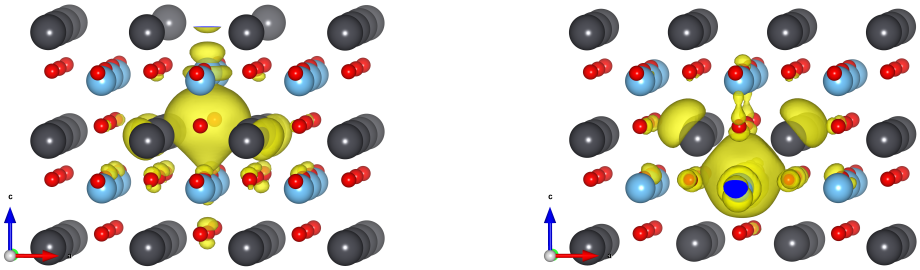

Figure 8.7: Defect states of the axial oxygen vacancy (left) and the in-plane oxygen vacancy (right). The electronic charge density is shown in yellow, while Pb atoms are grey, Ti blue and O red.

8.2.2 Lead Vacancy in $PbTiO_3$

The displacement field of the neutral lead vacancy is visualised for three different perspectives in Fig. 8.8. The largest displacement compared to the stoichiometric bulk PTO is given by the 4 O atoms closest to the defect. These ions, placed below the vacancy, move away from the defect by 0.13 Å. The 4 O atoms situated above the defect display a smaller displacement of 0.07 Å, also away from the vacancy. The 4 Pb atoms on the same xy-plane as the missing atom move towards V_{Pb} by 0.06 Å, thereby reducing the empty space created by the vacancy. Similarly, the 4 nearest Ti atoms above V_{Pb} move down towards the defect by 0.02 Å. The 4 Ti atoms situated below the vacancy move away from the defect with a displacement of 0.06 Å.

The total and the projected DOS of V_{Pb} is shown in Fig. 8.9. We see that the Fermi energy crosses the top of the valence band, leaving the highest of the O 2p states unoccupied. As for the oxygen vacancies, the defect level is not split from the band edge, giving the impression that the system is metallic. However, this is an effect of the GGA functional

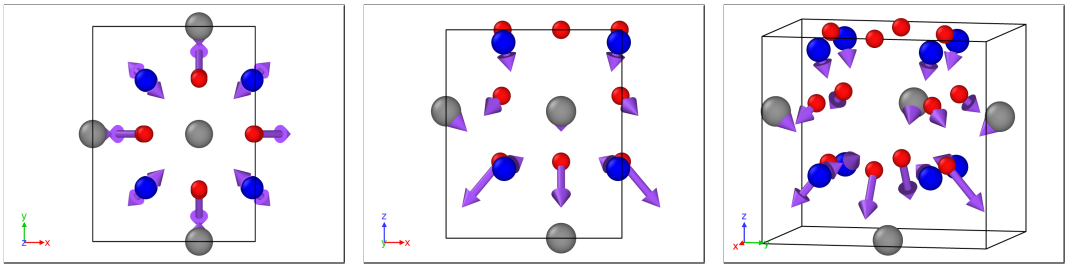

Figure 8.8: Displacement field around the lead vacancy in top (left), side (middle) and perspective view (right). Pb atoms are shown in grey, Ti in blue and O in red, with purple arrows indicating the direction and magnitude of the displacements.

which underestimates the split from the VB in the V_{Pb} [151].

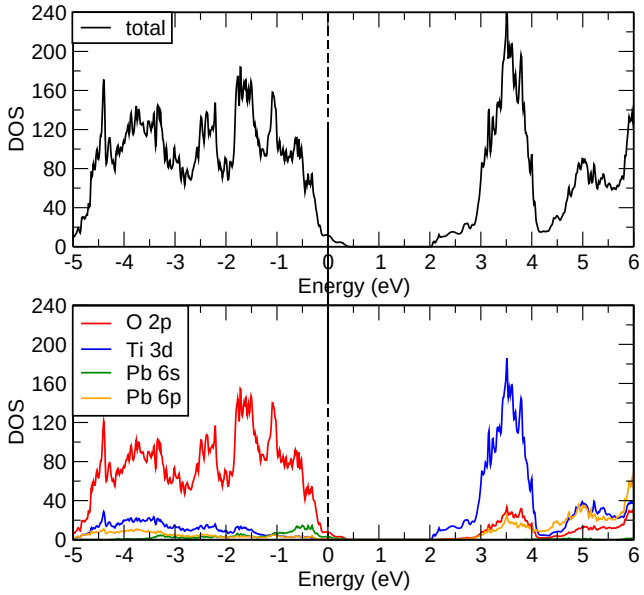

Figure 8.9: DOS (upper) and projected DOS (lower) of the lead vacancy (V_{Pb}) in tetragonal $PbTiO_3$.

8.2.3 Niobium Substitution in $PbTiO_3$

The Nb impurity (Nb_{Ti}) in PTO was created by replacing a Ti atom with a Nb (5+) atom. The DOS and the PDOS for both spin channels of Nb:PTO are plotted in Fig. 8.10. As for the oxygen vacancies, the E_F crosses the bottom of the CB, indicating that the Nb impurity acts as an electron donor. This results in two occupied defect states, one spin up, and one spin down, at the bottom of the CB. Again, these defect states are shallow which might be an effect of the GGA functional.

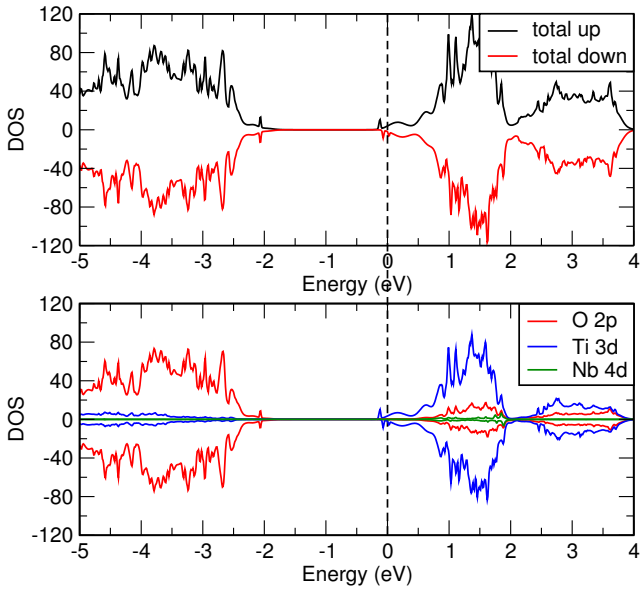

Figure 8.10: DOS (upper) and projected DOS (lower) of the Nb substitution of the Ti atom in tetragonal $PbTiO_3$.

8.2.4 Scandium Substitution in $PbTiO_3$

A Sc impurity (Sc_{Ti}) has been created by substituting a Ti atom for a Sc (3+) atom. The DOS and PDOS of the Sc:PTO system is shown in Fig. 8.11. Similar to the Pb vacancy, the Sc defect acts as an electron acceptor. Again the E_F is crossing at the top of the VB and the defect level is not split from the band edge as a result of the GGA functional. No Sc states lie within the VB, but there is a small contribution of Sc 3d states in the CB. The HOMO and the LUMO are both predominantly made up from O 2p orbitals.

8.2.5 Iron Substitution in $PbTiO_3$

The Fe impurity (Fe_{Ti}) was created by substituting a Ti atom for a Fe (3+) atom. Fig. 8.12 shows the DOS and PDOS for both spin channels in Fe:PTO. From the DOS one can identify two defect states in the band gap, a Fe state at the top of the VB and several Fe states at the bottom of the CB. Interestingly, the two deep lying gap states are both spin down states. This reduces the band gap of the down spin channel to 0.2 eV, while the band gap of the spin up channel is 1.4 eV.

The two localised gap states of the Fe impurity are visualised in Fig. 8.13. The HOMO state is localised on the Fe atoms and the 4 neighbouring O atoms. This defect state has a strong Fe d_{xy} and O p character and is occupied by the minority spin carrier. The LUMO state is also centred on the Fe atom but consists of Fe d_{yz} and O p orbitals. However, the

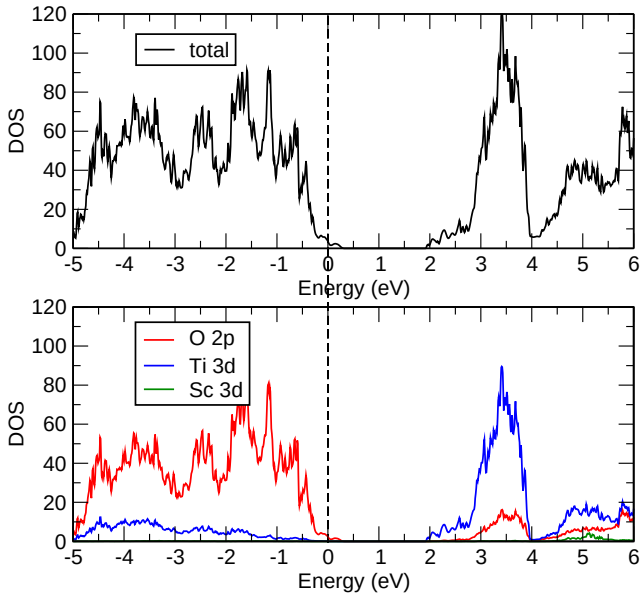

Figure 8.11: DOS (upper) and projected DOS (lower) of the Sc substitution of the Ti atom in tetragonal $PbTiO_3$.

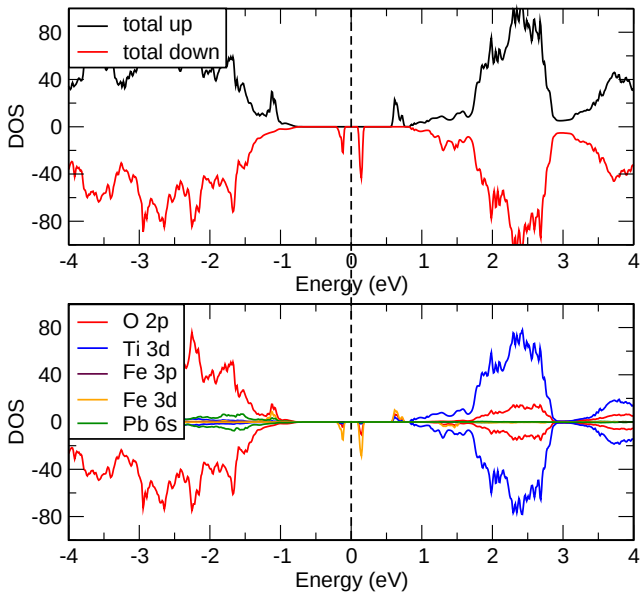

Figure 8.12: DOS (upper) and projected DOS (lower) of the Fe substitution of the Ti atom in tetragonal $PbTiO_3$.

unoccupied band gap state is not symmetric, because of the polar displacements along the c axis in the ferroelectric PTO.

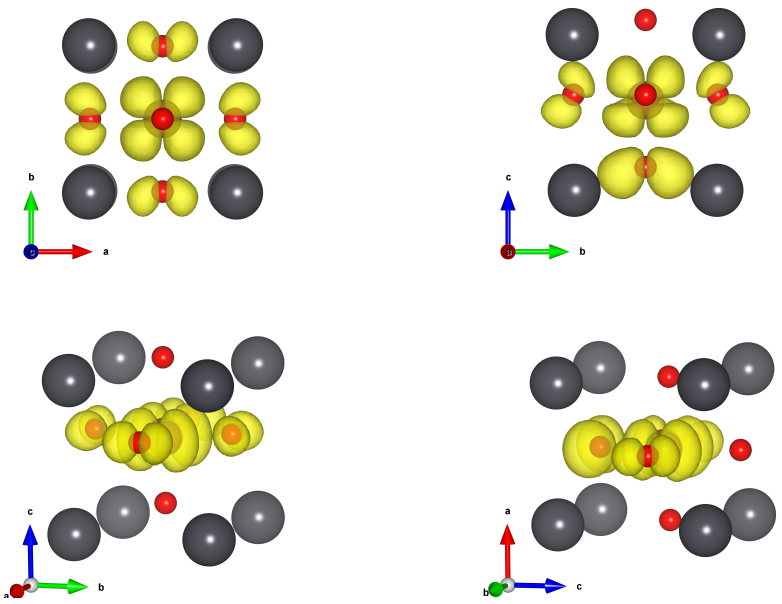

Figure 8.13: Localised defect states of the Fe impurity in tetragonal $PbTiO_3$. (left) The HOMO state in top and perspective view. (right) The LUMO state in top and perspective view. The electronic defect state centred on the Fe atom (orange) is shown in yellow, while Pb atoms are grey, Ti blue and O red.

8.2.6 Formation Energies

The formation energies (ΔE_f) of the defects were approximated according to equation 8.1, where the chemical potential was not taken into account. The results are shown in table 8.2. The two oxygen vacancies show similar formation energies of 5.78 eV for the axial and 5.51 eV for the in-plane defect. Thus, I find the in-plane V_O to be slightly more stable in tetragonal PTO, which is in contrast to $BaTiO_3$, where the axial vacancy is more stable according to recent a DFT study [123]. This is related to the significant Pb contribution in PTO that stabilises the non-polar vacancy. The substitutions of the Ti atom show much lower E_f for Nb_{Ti} (0.7 eV) and Sc_{Ti} (3.16 eV), making those defects more stable in tetragonal PTO than the studied vacancies. The Nb substitution has an especially low formation energy which facilitates the migration or doping of Nb into the material. On the other hand, the Fe_{Ti} demonstrates a large formation energy of 7.33 eV, similar to V_{Pb} (8.09 eV).

Table 8.2 also shows the defect type which was determined, as either acceptor or donor, from the DOS. This property of the defect allows to utilize them in order to compensate the positive polarisation charge at tail-to-tail or the negative charge at the head-to-head domain

Table 8.2: Formation energies (ΔE_f) calculated with eq. 8.1, of point defects in tetragonal PbTiO3 and the type of defect.

Defect	defect type	ΔE_f (eV)
V_O axial	donor	5.78
V_O in-plane	donor	5.51
Nb_{Ti}	donor	0.70
V_{Pb}	acceptor	8.09
Sc_{Ti}	acceptor	3.16
Fe_{Ti}	acceptor	7.33

walls, depending on their type. This compensation of charged DWs has been previously performed in 180° domain walls in PTO by Wu and Vanderbilt [141]. The authors used Nb_{Ti} as a donor and Sc_{Ti} as an acceptor which agrees with my results. I have further characterised the O vacancies as donors with shallow defect levels. The Pb vacancy, on the other hand, is an acceptor defect with no band gap states. Despite their larger formation energies, these two types of vacancies are common in PTO [149] and allow for strong charge compensation due to their doubly charged state. The last defect I investigated, the Fe substitution of Ti, is another acceptor which can be used to compensate electrons at head-to-head walls.

8.3 Band Gap of Domain Walls

8.3.1 180° Domain Wall

To calculate the structure of a 180° DW a 1x12x1 periodic system with a domain wall centred on the PbO layer (see Fig 8.14) was used. The Pb centred 180° DW was shown to be lower energy than the Ti centred wall in PTO from DFT [153], which is why I have chosen this configuration. Furthermore, a supercell size of 12 has been demonstrated to be sufficient to converge the 180° DW energy with size in PTO [154]. Since the chosen system is periodic, it contains two equal domain walls, separated by 6 unit cells (∼24Å). To obtain the ground state structure, the atomic coordinates and the cell vectors were optimised until the forces and the stress where below 0.005 eV/Å and 0.1 GPa, respectively.

The calculated band gap of the 180° DW is 1.66 eV which is slightly below the bulk value of 1.74 eV. This decrease of the band gap agrees with a recent DFT and Greens-

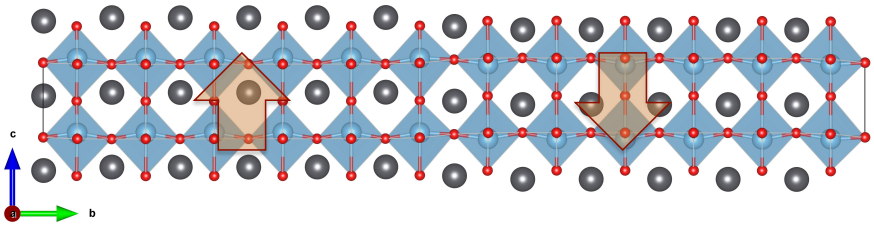

Figure 8.14: Structure of the Pb centred 180° domain wall containing 12 unit cells (60 atoms). Pb atoms are shown in grey, Ti in blue and O in red

function study [155], where a reduction of the band gap in PTO including a 180° DW is reported. The authors claim that the reduced band gap results in an enhancement of the leakage current at the DW, which can explain the higher conductance measured in such systems. I further calculated the DOS for each atomic layer perpendicular to the y-direction. All layers are insulating with a DOS which resembles the DOS in bulk PTO. However, at the DW one notices a slight increase of Ti d and O p density in the TiO_2 layers towards the band edges.

8.3.2 90° Domain Wall

For the head-to-tail 90° DW a $1x\frac{12}{\sqrt{2}}x\sqrt{2}$ periodic system (60 atoms) with a domain wall centred on the O_2 layer (see Fig. 8.15) was used. A supercell size of 12 unit cells has been shown to be sufficient to converge the domain wall energy with size [154]. I choose a supercell where the c-axis points along [011] or [01$\bar{1}$] depending on the domain, in order to accommodate the 90° DW in a periodic box. As for the 180° DW, the atomic coordinates and the cell vectors were optimised until the forces and the stress were below 0.005 eV/Å and 0.1 GPa, respectively.

The band gap was calculated to be 1.70 eV for the 90° DW, which is slightly smaller than the bulk value, yet higher than the 180° DW value (1.66 eV). Analysing the layer resolved DOS, I find a small increase in the DOS at the bottom of the CB of the PbTiO layers at the domain walls. This small shift of DOS towards the band edges is the reason for the slightly reduced band gaps of both types of domain walls in PTO. Calculating the atomic displacements from an ideal, centro-symmetric PTO reference structure for each unit cell, together with the Born-effective charges as described in section 3.4.1.1, allows for obtaining the local polarisation. Fig. 8.16 shows the total polarisation and the P_Z component

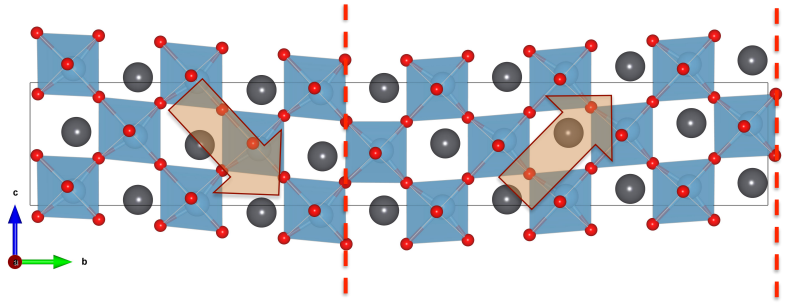

Figure 8.15: Structure of the neutral (head-to-tail) 90° domain wall containing 12 unit cells (60 atoms). Pb atoms are shown in grey, Ti in blue and O in red

across the two domain walls for the 90° and 180° case. Both systems show relatively narrow domain walls (centre and edge of the plot) of about 2 unit cell width. The total polarisation within the domains is constant, while there is a significant decrease of P_{tot} at the domain walls, where the P_Z component changes sign. Interestingly, there is a large asymmetry for the 90° DW system, where one domain consists of 7 unit cells, while the other domain consists of only 5. This asymmetry is due to an asymmetric electrostatic potential at the wall which has been recently found in DFT calculations and was subsequently confirmed experimentally in PTO [156].

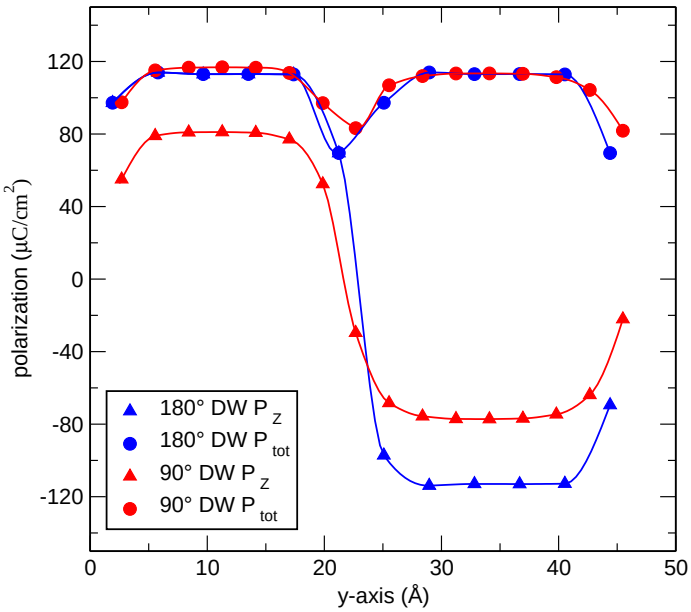

Figure 8.16: Total polarisation and the z-component of polarisation (P_Z) along the y-axis of the 180° and 90° domain walls (DW) in $PbTiO_3$.

I find that the reduction of the total P at the walls is larger for the 180° case than for the

90° case, which is related to their different symmetries at the walls. For the 180° DW the polarisation can only be reduced and reverted along the polar mode, while for the 90° DW the polarisation rotates, which allows for larger P_{tot}. This difference might explain the lower band gap in the 180° DW system, where the unit cells at the walls approach a tetragonal paraelectric PTO structure, which has a band gap of 1.50 eV. The 90° DW system retains more of its polarisation across the wall together with a stronger axial Ti-O bond, therefore showing a band gap closer to the ferroelectric bulk PTO. Nevertheless, both domain walls show a reduced band gap which can explain the higher conductance found at domain walls in ferroelectric thin films [18, 157, 158, 159], as recently proposed [155].

8.4 Metallicity in Charged 90° Domain Walls

After confirming that the common head-to-tail 90° DW is stable in PTO in the previous section (8.3.2), I went on to investigate the stability of charged head-to-head DWs. For this task I used a $1x\frac{12}{\sqrt{2}}x\sqrt{2}$ periodic system with a domain wall centred on the PbTiO layer, where the domains were oriented along $[0\bar{1}\bar{1}]$ and $[01\bar{1}]$, respectively. By applying periodic boundary conditions this creates two domain walls: A head-to-head (HH) wall at the center of the cell and a tail-to-tail (TT) wall at the cell edge, as seen in Fig. 8.17. Performing a geometry optimisation on this system results in a mono domain state, where the domain walls have been eliminated. The polarisation charge located on both walls (positive charge at the head-to-head wall, negative charge at the tail-to-tail wall) leads to a strong electrostatic repulsion which forces the domains to rotate and reduce the wall area during the geometry optimisation.

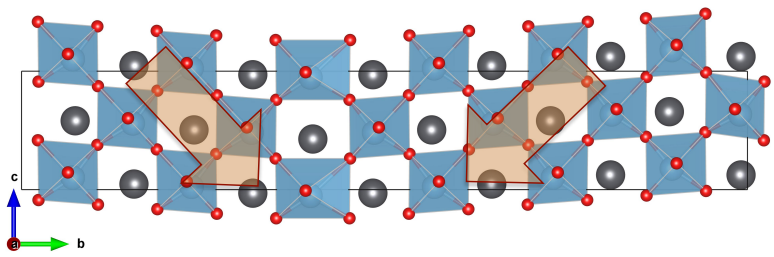

Figure 8.17: Structure of charged 90° domain walls in $PbTiO_3$. The head-to-head wall appears in the middle of the cell and and the tail-to-tail wall at the cell edge.

Plotting the layer resolved DOS (see Fig. 8.18) of the original charged DW system, where no optimisation of coordinates was performed (see Fig. 8.17), confirms the picture of unstable DWs: Although each PbTiO and each O_2 layer shows a band gap and is insulating,

the whole system is metallic. The metallicity occurs as a result of the large band bending across the the system, where the CB and the VB shift to lower energies from the TT towards the HH wall. At the walls, the CB and VB edges then cross E_F, which generates free carriers. The free carriers at the HH wall are electrons, while the free carriers generated at the TT wall are holes. The band bending I report for charged PTO 90° DWs, which is large enough to bridge the band gap, agrees with the model of charged domain walls by Sluka et at. [21].

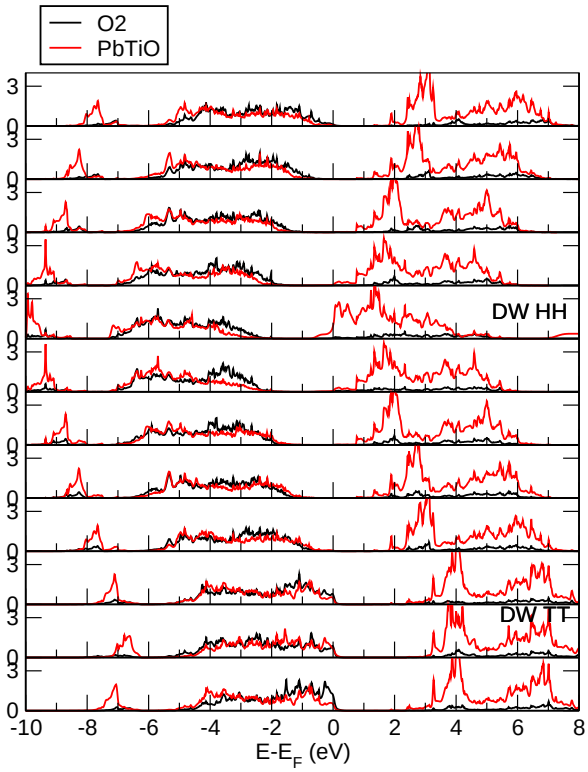

Figure 8.18: Layer resolved density of states (DOS) of a charged 90° domain wall (DW) in $PbTiO_3$ showing large band bending. Black indicates the DOS from the O_2 planes while red indicates the PbTiO planes. The atomic layers at the domain walls are marked with HH for head-to-head or TT for tail-to-tail.

8.5 Defect Mediated Stabilisation of Charged Domain Walls

In the previous section (8.4), I confirmed that charged domain walls are metallic and unstable against polarisation rotation, as previously shown by theoretical studies [141, 21]. In order to stabilise charged 90° DWs, point defects at both the HH and the TT walls were introduced, following the approach of previous DFT calculations of 180° head-to-head and tail-to-tail domain walls [141, 142]. I chose an acceptor/donor pair to compensate

the electrons at the HH wall (with an acceptor) and the holes at the TT wall (with a donor). For this the defects that were previously characterized as donors or acceptors in tetragonal PTO (see table 8.2) were used. The atomic coordinates of the domain wall systems with donor/acceptor pairs were then optimised until the forces were below 0.005 eV/Å.

8.5.1 90° Domain Wall: V_{Pb}/V_O

For the head-to-head and tail-to-tail 90° DW a $1x\frac{12}{\sqrt{2}}x\sqrt{2}$ periodic system with a Pb vacancy at the HH and an in-plane O vacancy at the TT wall (see Fig. 8.19) was used. The V_{Pb} acts as an acceptor and the V_O as an electron donor, both compensating the bound polarisation charge at the walls and leaving the system charge neutral. The two domain walls in the periodic system are centred on the PbTiO layers with the respective vacancy.

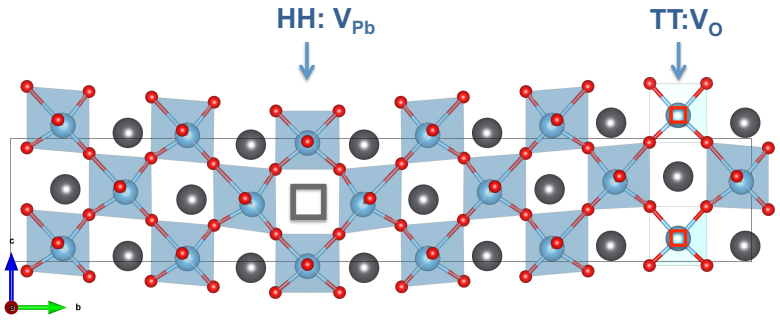

Figure 8.19: Structure of the head-to-head (HH) and tail-to-tail (TT) 90° domain wall in $PbTiO_3$ with a Pb vacancy (V_{Pb}) and an in-plane O vacancy (V_O). The V_{Pb} is located at the HH wall and indicated by a grey square, while the V_O is located at the TT wall and denoted with a red square (appears twice in the displayed cell because of the periodic boundary conditions). Pb atoms are grey, Ti blue and O red.

The relaxed structure with the two vacancies kept its polarisation state and has two clearly visible domain walls, as seen in Fig. 8.19. Therefore, the defect pair stabilises the HH and TT walls in PTO and prevents the elimination of the walls through polarisation rotation. The layer resolved DOS of this system is plotted in Fig. 8.20. In this plot the layers consist of alternating PbTiO and O_2 planes, which are perpendicular to the b axis and parallel to the DWs. In contrast to the uncompensated charged 90° DW (see Fig. 8.18), there is no band bending across the cell. All layers, except the TT wall layer with the V_O, are insulating. The layer containing the O vacancy and its two adjacent layers show a large DOS contribution at the bottom of the CB. This is similar to the effect of the V_O in bulk PTO, which shows defect levels at the bottom of the CB (see section 8.2). Interestingly,

at the TT domain wall the vacancy results in a closed band gap which makes the system metallic. The neighbouring layers remain insulating with a slightly reduced band gap, so that the metallicity is confined to the DW. On the other side, the HH wall layer with the V_{Pb} is insulating and shows only a slight increase of DOS at the CB bottom.

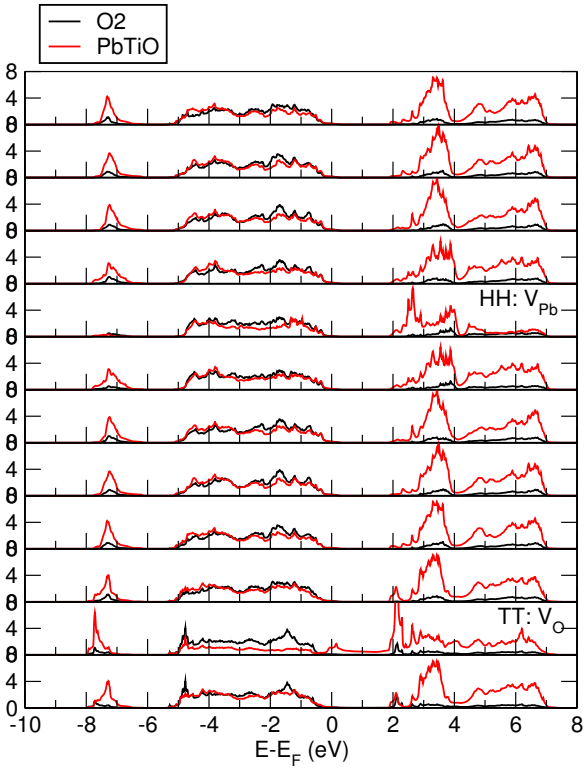

Figure 8.20: Layer resolved density of states (DOS) of the head-to-head (HH) and tail-to-tail (TT) 90° domain wall in $PbTiO_3$ with a Pb vacancy (V_{Pb}) and a O vacancy (V_O). Black indicates the DOS from the O_2 planes while red indicates the Pb-Ti-O planes. The atomic layers at the domain walls are marked with HH for head-to-head or TT for tail-to-tail.

Furthermore, the coordinates of the same DW system were optimised with only one vacancy, either V_{Pb} or V_O. I find that a sole O vacancy at the TT wall is not enough to stabilise the TT and the HH walls in the system. The geometry optimisation rotated both domains to eliminate the domain walls completely, resulting in a monodomain. Noteworthy, a single V_{Pb} was sufficient to keep the polarisation in the HH and TT configuration in PTO. The relaxed cell with the Pb defect at the HH wall is shown in Fig. 8.21. Here, the head-to-head DW is clearly visible and similar to the HH wall in Fig. 8.19. On the other hand, the regions close to the TT wall are less polarised, due to the lack of charge compensation. Nevertheless, the single V_{Pb} successfully stabilises the charged 90° DW configuration in

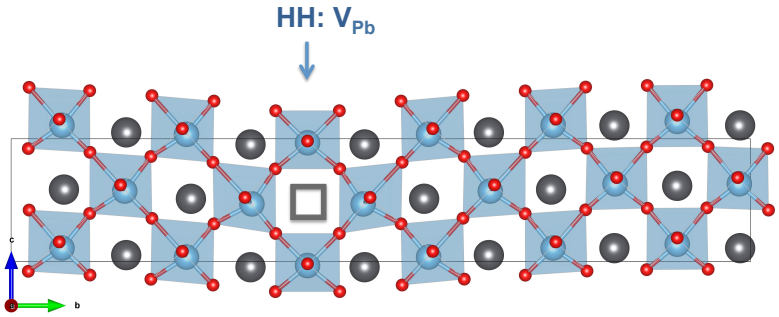

Figure 8.21: Structure of the head-to-head (HH) and tail-to-tail (TT) 90° domain wall in $PbTiO_3$ with a Pb vacancy (V_{Pb}). The V_{Pb} is located at the HH wall and indicated by a grey square. Pb atoms are grey, Ti blue and O red.

PTO.

8.5.2 90° Domain Wall: Sc_{Ti}/Nb_{Ti}

The relaxed structure of the 90° DW with a Sc_{Ti}/Nb_{Ti} defect pair is shown in Fig. 8.22. A $1x\frac{12}{\sqrt{2}}x\sqrt{2}$ system was used, where the defect atoms substitute the Ti atoms at the HH and the TT DW. In this case the Sc^{3+} defect acts as an acceptor, while the Nb^{5+} impurity is an electron donor. The optimised structure is charge neutral, insulating and has a HH wall centred on the Sc_{Ti} and a TT wall centred on Nb_{Ti}.

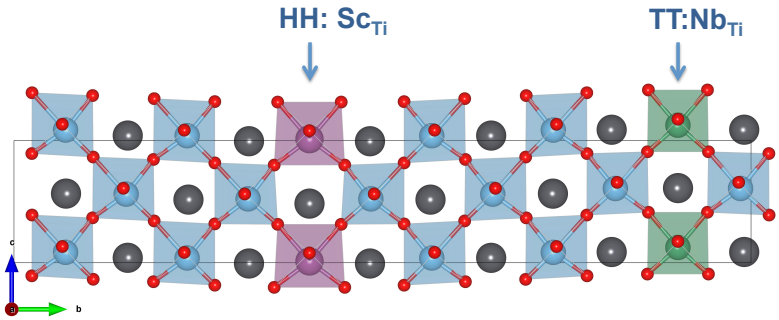

Figure 8.22: Structure of the head-to-head (HH) and tail-to-tail (TT) 90° domain wall in $PbTiO_3$ with a Sc impurity (Sc_{Ti}) and a Nb impurity (Nb_{Ti}). The Sc_{Ti} in purple is located at the HH wall, while the Nb_{Ti} in green is located at the TT wall. Pb atoms are grey, Ti blue and O red.

Fig. 8.23 shows the layer resolved DOS of the PbTiO and O_2 layers parallel to the DWs. Here, all the layers are insulating, including the domain walls, and the system has a band gap of 2.08 eV. The PbScO layer at the HH wall has a reduced DOS at the bottom of the CB because of the missing Ti atom, while the states of the Sc substitution lie higher in energy. The TT wall with the Nb impurity shows a DOS similar to the Nb_{Ti} in bulk PTO,

where the bottom of the CB shows a slightly increased DOS. The band gap, however, is not closed by defect states in the DW system, in contrast to what is seen in the TT DW with an O vacancy. Note, that the charge compensation in this system is less complete than the V_{Pb}/V_O case. since the actual polarisation charge at the charged 90° walls in PTO is 2.2 e (with a PTO polarisation of 113.2 $\mu C/cm^2$). A doubly charged V_O or V_{Pb} should, therefore, compensate the polarisation to a good degree, while the singly charged Sc and Nb impurities won't be able to fully compensate the charge. Nevertheless, the Sc_{Ti}/Nb_{Ti} systems stabilises both charged 90° DWs in PTO, which means that a near perfect charge compensation is not necessary to stabilise HH and TT walls.

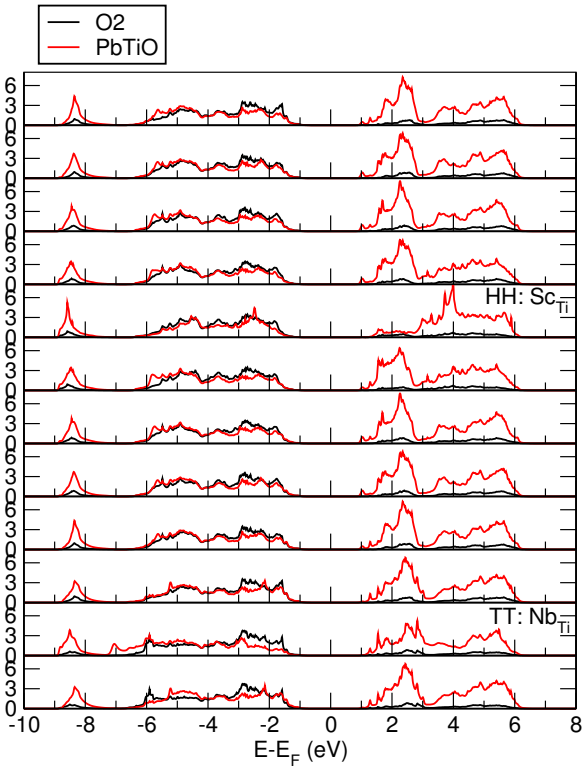

Figure 8.23: Layer resolved density of states (DOS) of the head-to-head (HH) and tail-to-tail (TT) 90° domain wall in $PbTiO_3$ with a Sc impurity (Sc_{Ti}) and a Nb impurity (Nb_{Ti}). Black indicates the DOS from the O_2 planes while red indicates the PbTiO planes. The atomic layers at the domain walls are marked with HH for head-to-head or TT for tail-to-tail.

8.5.3 90° Domain Wall: Fe_{Ti}/Nb_{Ti}

A Fe_{Ti}/Nb_{Ti} 90° DW system was optimised in a similar way to the above to cases. Here, the donor defect is a Nb^{5+} substitution of Ti at the TT wall and the acceptor defect is a Fe^{3+} substitution of Ti at the HH wall. The optimised structure is visualised in Fig. 8.24. Again,

I find that the defect pair stabilises the head-to-head and tail-to-tail facing domains with their polarisation state. The overall structure looks similar to the Sc_{Ti}/Nb_{Ti} DW system and the the ferroelectric displacements close to the wall are smaller than the V_{Pb}/V_O case.

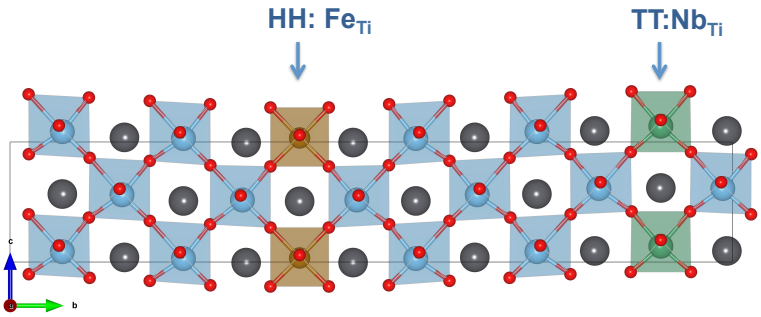

Figure 8.24: Structure of the head-to-head (HH) and tail-to-tail (TT) 90° domain wall in $PbTiO_3$ with a Fe impurity (Fe_{Ti}) and a Nb impurity (Nb_{Ti}). The Fe_{Ti} in brown is located at the HH wall, while the Nb_{Ti} in green is located at the TT wall. Pb atoms are grey, Ti blue and O red.

Fig. 8.25 shows the layer resolved DOS of the PbTiO and O_2 layers parallel to the DWs. No band bending is found across the system and all layers are insulating except the HH plane. At the HH wall the Fe defect closes the band gap in one spin channel, while the other spin shows a small band gap of 0.5 eV. This is in agreement with the Fe_{Ti} in bulk PTO, where the deep gap states originates from one spin channel. As for the V_{Pb}/V_O DW system the gap closure is confined to the domain wall layer.

The V_{Pb}/V_O, Sc_{Ti}/Nb_{Ti} and Fe_{Ti}/Nb_{Ti} defect pairs all stabilise the head-to-head and tail-to-tail domains in PTO. Interestingly, only the Sc_{Ti}/Nb_{Ti} is fully insulating, while the V_{Pb}/V_O and Fe_{Ti}/Nb_{Ti} cases show metallicity at the defective DWs. This metallicity originates from the gap states of the defects and not from the charge states, as both Sc and Fe are in a 3+ oxidation state.

8.5.4 Polarisation in Charged Domain Walls

Besides the structure and the DOS the polarisation across the stable head-to-head and tail-to-tail domain walls was approximated. The polarisation was calculated as described in section 3.4.1.1 which approximates P from the Born effective charges and ionic displacements. This approximation of P has the advantage that it gives a unit cell based value and that its applicable in metallic systems where the polarisation is formally ill-defined. Further, the Born effective charges (Z^*) of the substitutions were estimated as: $Z^*_{Ti} - 1$ for Sc and Fe as and as $Z^*_{Ti} + 1$ for Nb, following the approach of Wu and Vanderbilt [141]. In

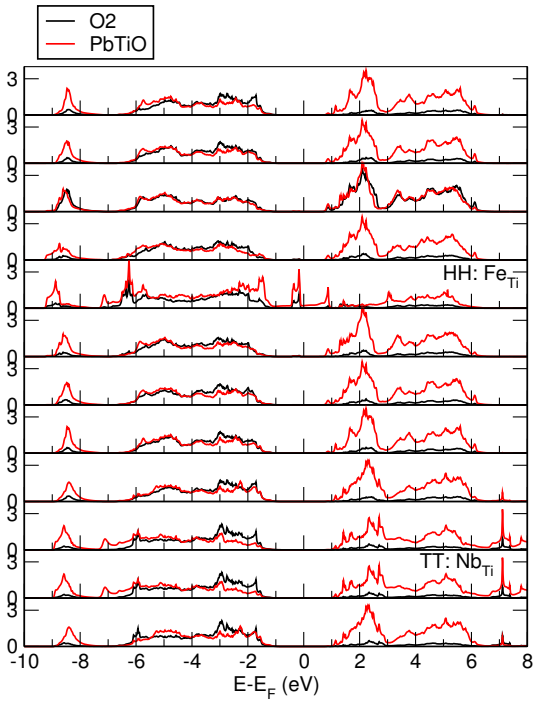

Figure 8.25: Layer resolved density of states (DOS) of the head-to-head (HH) and tail-to-tail (TT) 90° domain wall in $PbTiO_3$ with a Fe impurity (Fe_{Ti}) and a Nb impurity (Nb_{Ti}). Black indicates the DOS from the O_2 planes while red indicates the PbTiO planes. The atomic layers at the domain walls are marked with HH for head-to-head or TT for tail-to-tail.

the case of the O and Pb vacancies, I assumed the vacant atom to be in its average position in order to calculate the polarisation of the defective unit cells. Fig. 8.26 shows the total polarisation of the tested DW systems. For all systems, including the head-to-tail case, the polarisation dips at the domain walls, which are at the PbTiO layer 5 (HH) and 11 (TT). Overall, the magnitude of the polarisation in the domains is lower in the defective systems than in the head-to-tail (HT) reference. The V_{Pb}/V_O shows the highest domain polarisation, reaching the value of bulk PTO (dotted horizontal line). However, at both domain walls the polarisation drops drastically to around 60 $\mu C/cm^2$. Interestingly, there is a large increase in polarisation and tetragonality at the HH wall with the Pb vacancy, which can be seen in the atomic structure displayed in Fig. 8.19. Here, the missing Pb atom allows for a larger displacement of the Ti atoms, which increases the polarisation in the adjacent layers of the DW to 132 $\mu C/cm^2$. As expected, the single V_{Pb} system shows very similar behaviour to the V_{Pb}/V_O cell around the Pb vacancy at the HH wall, including the enhanced polarisation in the adjacent layers to the wall. The TT wall, on the other side, exhibits the same polari-

sation as the defect free system. However, the polarisation within the domains is lower than the defect free head-to-tail reference system and the V_{Pb}/V_O DW system. This is a result of the missing charge compensation at the TT wall which reduces the polarisation towards the wall. The fact that the TT wall is stable and its surrounding domains carry polarisation is likely due to the charge compensated HH wall being nearby. Increasing the separation between the two domain walls will probably lead to a further reduction of polarisation in proximity of the HH wall and eventually eliminate the polarisation and thereby the domain wall completely.

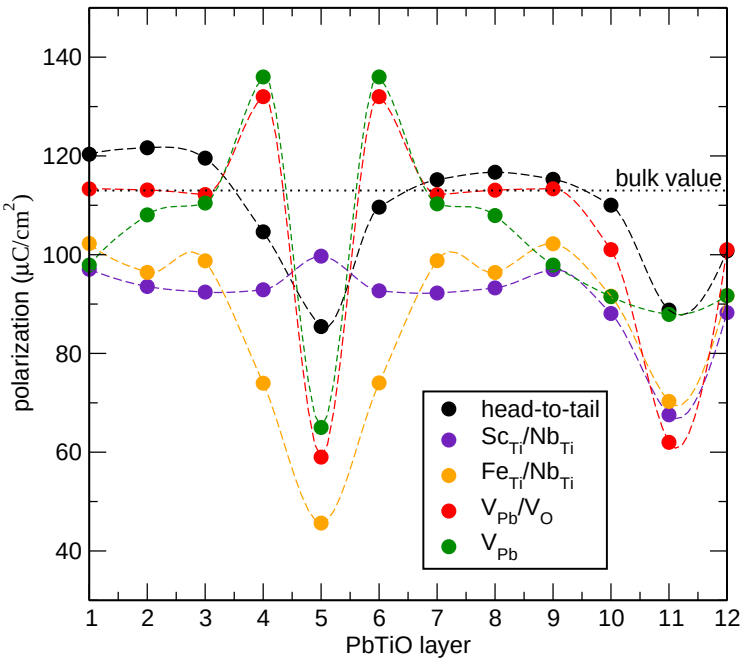

Figure 8.26: Polarisation across the two domain walls in $PbTiO_3$ for the head-to-tail and the head-to-head/tail-to-tail systems with defect pairs. The dotted line denotes the bulk value of the polarisation for comparison. For the charged domain walls the head-to-head wall is centred on PbTiO layer 5, while the tail-to-tail wall is centred on PbTiO layer 11.

The polarisation in the domains of the Sc_{Ti}/Nb_{Ti} and Fe_{Ti}/Nb_{Ti} systems is significantly reduced compared to the HT reference and the bulk PTO value, due to the incomplete charge compensation. At the TT wall with the Nb^{5+} defect, both systems have a similar polarisation value of around 70 $\mu C/cm^2$. However, at the HH wall the Sc_{Ti} has a much larger polarisation than the Fe_{Ti} wall, which shows the lowest polarisation of all systems at 45 $\mu C/cm^2$. The large reduction of the polarisation around the Fe^{3+} defect is further accompanied by a broader HH domain wall. Note, that the polarisation at the HH wall in

Sc_{Ti}/Nb_{Ti} actually increases compared to the domain polarisation and it even surpasses the DW value of the HT system. Overall, the defects have a large effect on the polarisation, not just in the vicinity of the domain wall but also within the domains.

8.5.5 Stability of the Charged Domain Walls with Defects

The formation energy of the domain walls including the defects was calculated according to equation 8.1. For the three investigated systems I find the total formation energies to be 11.00 eV for the V_{Pb}/V_O DW system, 2.15 eV for the Sc_{Ti}/Nb_{Ti} DW system and 7.23 eV for the Fe_{Ti}/Nb_{Ti} DW case. I report that the vacancy formation energy is higher than then for the B-cation substitution which agrees with ΔE_f in bulk PTO. The Sc_{Ti}/Nb_{Ti} DW cell demonstrates the lowest formation energy due to the low individual ΔE_f of the defects in bulk. Remarkably, all DW systems with defect pairs have lower formation energies than the individual defects in bulk together. This means the defects are more stable at their respective domain walls than in tetragonal bulk, which agrees with a previous LDA study reporting that O vacancies in PTO have lower formation energies at 180° domain walls than in bulk [17]. Here, I show that this is true for all the tested defect pairs in 90° DWs. The increased stability at the DW means that the defects will pin the walls at the defect site, effectively immobilising them. Considering the strong interaction of the defect with the polarisation of the adjacent domains, selective doping of PTO could, therefore, influence its domain pattern. However, the pinning of the domain walls would likely alter its switching behaviour.

Note, that in the examined 90° DW systems the planar defect concentration in x-z plane is very large with one defect per wall area of a x $\sqrt{2}a$, where a is the lattice parameter. Very high impurity or defect concentrations would be necessary to form the investigated domain structures in real materials. Nevertheless, this could be achieved by modern synthesis methods of thin films, such as pulsed laser deposition (PLD), which could incorporate such layers of defect atoms in ferroelectric oxides.

8.6 Conclusions

In this chapter the defect mediated stabilisation of charged domain walls in PTO from WC-DFT calculations was investigated. I found that the WC GGA functional accurately represents the structure and the Born-effective charges of bulk PTO. The electronic band structure is well reproduced, although with an expectedly underestimated band gap (1.74 eV) than

the experimental values (3.4 eV [145]). Analysing a series of defects in bulk PTO, namely V_O, V_{Pb}, Nb_{Ti}, Sc_{Ti} and Fe_{Ti}, I found the lowest formation energies for the Nb and Sc substitutions (0.7 eV and 3.16 eV respectively).

I report that 180° and 90° DWs in PTO lower the band gap by 0.08 eV and 0.04 eV, respectively. This reduction of the band gap has recently been seen in DFT study on 180° DWs in PTO [155], where the authors claim it to be the reason for increased conductance at domain walls. Here, I also to confirm a small reduction in band gap for 90° DWs which could lead to increased conductivity at such walls. The increased conductivity might, therefore, be an intrinsic phenomenon in ferroelectrics and not originate from common defects that accumulate at domain walls.

Additionally, the calculations are in agreement with earlier theoretical models [147], predicting the metallic nature of uncompensated head-to-head and tail-to-tail 90° domain walls, which are unstable against polarisation rotation that eliminates the domain walls. I further demonstrated how a charged, insulating 90° DW can be stabilised with a Sc_{Ti}/Nb_{Ti} defect pair, analogous to what has been found for 180° in PTO from DFT [141]. Noteworthy, a V_{Pb}/V_O and a Fe_{Ti}/Nb_{Ti} acceptor/donor pair also stabilised the HH and TT polarisation state in 90° DWs, but formed a metallic layer at the TT and the HH walls, respectively. Interestingly, I find that these metallic layers are confined to the domain wall layers, as they are induced by the defect states of the dopants. The results thereby confirm that O vacancies can partially stabilise charged DWs, as recently postulated [147], but they may effect the conductivity of the system.

I conclude that a defect charge of 1 e is sufficient to stabilise nanometre sized 90° head-to-head and tail-to-tail domain walls in PTO, but that the choice of defect can have a severe effect on the conductivity. The type of defect further influences the polarisation at and nearby the domain wall, which in return will influence the strain state of the ferroelastic 90° walls. The strong interaction between the defects and the polarisation charge that I observe, could open up novel routes to engineer nanoscale domain patterns with enhanced piezoelectric properties via controlled doping of ferroelectric compounds.

Chapter 9

Conclusions

In this thesis, I provide theoretical insight into the properties and functionality of the industrially important material $Pb(Zr_{1-x}Ti_x)O_3$. I have developed a robust shell model force field for $Pb(Zr_{1-x}Ti_x)O_3$ (PZT) based on the results of density functional theory (DFT) calculations. The force field successfully reproduces the temperature and composition induced phase transitions of PZT which allows for the modelling of properties and dynamics of PZT under external stimuli. The efficient shell model further enables simulations of domain wall dynamics and stability, various types of defects, and the variation of the B-cations to provide insight into the fundamental physics of solid solution materials.

$Pb(Zr_{1-x}Ti_x)O_3$ is a solid solution of $PbTiO_3$ (PTO) and $PbZrO_3$ (PZO) where the B-cations are conventionally thought to be randomly distributed. However, my results show that the two B-cations contribute differently to the polarisation of the material and that their arrangement crucially effects the piezoelectric properties. This means that coercing the order of the B-cations could greatly improve the properties of PZT materials. In more detail, I find that a Ti rich environment adopts high polarisation values and a Zr rich environment adopts low polarisation states. Furthermore, my simulations demonstrate that the formation of B-cation clusters in $PbZr_{0.5}Ti_{0.5}O_3$ heavily influences the properties of the material, with small clusters having a positive effect while large clusters deteriorate the material's properties. The tuning of the B-cation arrangement, especially reducing the appearance of large clusters, can therefore add control and performance to PZT based piezoelectric devices.

Applying the force field to study the effect of electric fields on ferroelectric PZT, I reproduced experimental P-E loops and their temperature behaviour. The results show that the coercive field (E_C) decreases exponentially with temperature, which seems to be generic for

ferroelectric materials and independent of the actual switching process. The implication of this exponential behaviour is that it will be necessary to use high fields to employ switchable ferroelectric devices at low temperatures. These findings can provide guidance for temperature/voltage regimes of ferroelectric-based devices in aeronautical and space applications, as they are exposed to a wide range of operating temperatures. Studying the switching dynamics in PZT in more detail, I found two competing mechanisms that govern the polarisation dynamics: at room temperature nucleation and subsequent domain growth is the dominating switching process. However, at low temperatures, I predict that homogeneous nucleation is inhibited and single domain systems will switch through a polarisation rotation mechanism. This rotational mode has not been observed experimentally but it could play an important role in materials where inhomogeneous nucleation from surfaces, defects or grain boundaries is not prevailing.

Molecular dynamics simulations offer a straight forward way to calculate the electrocaloric effect (ECE) in ferroelectrics. Performing MD simulations on PZT, I studied the fundamental principles of the ECE in ferroelectrics and antiferroelectrics: My simulations show a giant ECE in PTO of 16 K and further confirm the negative ECE found in PZO. Most importantly, I report a trade-off in the ECE across the PZT solid solution, where a large ECE is accompanied with a large T_C and therefore requires high operating temperatures. Nevertheless, PZT offers a great variance in ECE magnitude, which allows for compositional engineering of materials for electrocaloric applications.

I conclude this thesis with DFT calculations on domain walls in PTO, where I find a reduction of the band gap in 180° an 90° domain walls. This reduction, albeit small, can explain the increased conductivity found in ferroelectric domain walls, making the origin intrinsic to the material. I further studied charged 90° domain walls, which I found to be unstable and metallic in nature. However, my DFT calculations show how such charged 90° domain walls can be successfully stabilised by an acceptor/donor defect pair such as Sc_{Ti}/Nb_{Ti}. This strong interaction between defects and the polarisation state could provide novel pathways to engineer nanoscale domain patterns with enhanced piezoelectric properties via the controlled doping of ferroelectrics.

The developed $Pb(Zr_{1-x}Ti_x)O_3$ force field offers great potential for studying ferroelectric materials. By mainly considering the effects of electric fields, the B-cation ordering and domain patterns in PZT, I only touched a subset of interesting topics in this material and

many open questions remain. Statistical analysis of the different phases around the morphotropic phase boundary (MPB) and in the Zr part of the phase diagram would add to the understanding of PZT and further characterise the force field and its applicability. Another natural topic to study with the force field would be the effect of defects and their interactions with domain walls. Furthermore, the competition between the two switching mechanisms, polarisation rotation and nucleation, in PZT is not fully explored yet. It would be important to investigate the difference in switching speed and performance between the two mechanisms and to map out the temperatures and fields in which they are predominant. Although I have quantified the electrocaloric effect in the PZT solid solution, the methodology offers further investigations, such as the effect of pressure, strain or defects on the magnitude of the effect. Studies of these stimuli could help increasing the ECE in the ubiquitous PZT and finally take the ECE from the laboratory to real devices.

Chapter 10

Bibliography

[1] Z. Wu and R. E. Cohen, "More accurate generalized gradient approximation for solids," *Physical Review B - Condensed Matter and Materials Physics*, vol. 73, 2006.

[2] M. F. M. Taib, M. K. Yaakob, O. H. Hassan, and M. Z. a. Yahya, "Structural, Electronic, and Lattice Dynamics of $PbTiO_3$, $SnTiO_3$, and $SnZrO_3$: A Comparative First-Principles Study," *Integrated Ferroelectrics*, vol. 142, no. 1, pp. 119–127, 2013.

[3] L. E. Cross and R. E. Newnham, "History of Ferroelectrics," *Ceramics and Civilization*, vol. III, pp. 289–305, 1987.

[4] N. Izyumskaya, Y. I. Alivov, S. J. Cho, H. Morkoç, H. Lee, and Y. S. Kang, "Processing, Structure, Properties, and Applications of PZT Thin Films," *Critical Reviews in Solid State and Materials Sciences*, vol. 32, pp. 111–202, jul 2007.

[5] K. M. Rabe, M. Dawber, C. Lichtensteiger, C. H. Ahn, and J. M. Triscone, "Modern physics of ferroelectrics: Essential background," *Topics in Applied Physics*, vol. 105, pp. 1–30, 2007.

[6] K. M. Rabe, C. H. Ahn, J. M. M. Triscone, M. Dawber, and C. Lichtensteiger, *Physics of Ferroelectrics*, vol. 105. 2007.

[7] J. Curie and P. Curie, "Développement, par pression, de l'électricité polaire dans les cristaux hémièdres à faces inclinées," *Comptes-Rendus de l'Académie des Sciences*, vol. 91, pp. 294–295, 1880.

[8] J. Valasek, "Piezo-electric and allied phenomena in Rochelle salt," *Physical Review*, vol. 17, pp. 475–481, 1921.

[9] G. Shirane and K. Susuki, "Crystal structure of PZT," *Journal of the Physical Society of Japan*, vol. 7, p. 333, 1952.

[10] T. Shimada and T. Kitamura, "Multi-physics Properties in Ferroelectric Nanowires and Related Structures from First-principles," *Nanowires*, no. March, 2010.

[11] "License, by-nc-sa." `https://creativecommons.org/licenses/by-nc-sa/3.0/`.

[12] H. Fan, "The influence of fabrication processing on domain structure and polarization switching in PZN-based ferroelectric ceramics," in *Materials Science and Engineering B: Solid-State Materials for Advanced Technology*, vol. 120, pp. 114–118, 2005.

[13] J. Liu, W. Chen, B. Wang, and Y. Zheng, "Theoretical Methods of Domain Structures in Ultrathin Ferroelectric Films: A Review," *Materials*, vol. 7, pp. 6502–6568, sep 2014.

[14] A. Pramanick, A. D. Prewitt, J. S. Forrester, and J. L. Jones, "Domains, Domain Walls and Defects in Perovskite Ferroelectric Oxides: A Review of Present Understanding and Recent Contributions," *Critical Reviews In Solid State And Materials Sciences*, vol. 37, no. 4, pp. 243–275, 2012.

[15] J. Guyonnet, "Ferroelectric Domain Walls," *Springer Thesis*, p. Chap. 2, 2014.

[16] P. R. Potnis, N. T. Tsou, and J. E. Huber, "A review of domain modelling and domain imaging techniques in ferroelectric crystals," *Materials*, vol. 4, no. 2, pp. 417–447, 2010.

[17] L. X. He and D. Vanderbilt, "First-principles study of oxygen-vacancy pinning of domain walls in $PbTiO_3$," *Physical Review B*, vol. 68, no. 13, p. 7, 2003.

[18] J. Seidel, L. W. Martin, Q. He, Q. Zhan, Y.-H. Chu, A. Rother, M. E. Hawkridge, P. Maksymovych, P. Yu, M. Gajek, N. Balke, S. V. Kalinin, S. Gemming, F. Wang, G. Catalan, J. F. Scott, N. a. Spaldin, J. Orenstein, and R. Ramesh, "Conduction at domain walls in oxide multiferroics.," *Nature Materials*, vol. 8, no. 3, pp. 229–234, 2009.

[19] P. S. Bednyakov, T. Sluka, A. K. Tagantsev, D. Damjanovic, and N. Setter, "Formation of charged ferroelectric domain walls with controlled periodicity," *Scientific Reports*, vol. 5, p. 15819, 2015.

[20] Y. L. Tang, Y. L. Zhu, Y. J. Wang, W. Y. Wang, Y. B. Xu, W. J. Ren, Z. D. Zhang, and X. L. Ma, "Atomic-scale mapping of dipole frustration at 90 charged domain walls in ferroelectric $PbTiO_3$ films.," *Scientific Reports*, vol. 4, p. 4115, 2014.

[21] T. Sluka, A. K. Tagantsev, D. Damjanovic, M. Gureev, and N. Setter, "Enhanced electromechanical response of ferroelectrics due to charged domain walls," *Nature Communications*, vol. 3, p. 748, 2012.

[22] P. Gao, J. Britson, J. R. Jokisaari, C. T. Nelson, S.-H. Baek, Y. Wang, C.-B. Eom, L.-Q. Chen, and X. Pan, "Atomic-scale mechanisms of ferroelastic domain-wall-mediated ferroelectric switching.," *Nature Communications*, vol. 4, no. 2791, p. 2791, 2013.

[23] R. P. Zdravko Kutnjak, Brigita Rožič, "Electrocaloric Effect: Theory, Measurements, and Applications," 2015.

[24] J. Scott, "Electrocaloric Materials," *Annual Review of Materials Research*, vol. 41, no. 1, pp. 229–240, 2011.

[25] P. Kobeko and J. Kurtschatov, "Dielektrische Eigenschaften der Seignette-salzkristalle," *Zeitschrift fur Physik*, vol. 66, no. 3-4, pp. 192–205, 1930.

[26] A. S. Mischenko, Q. Zhang, J. F. Scott, R. W. Whatmore, and N. D. Mathur, "Giant electrocaloric effect in thin-film PZT," *Science*, vol. 311, no. 5765, pp. 1270–1271, 2006.

[27] W. Geng, Y. Liu, X. Meng, L. Bellaiche, J. F. Scott, B. Dkhil, and A. Jiang, "Giant Negative Electrocaloric Effect in Antiferroelectric La-Doped $Pb(ZrTi)O_3$ Thin Films Near Room Temperature," *Advanced materials (Deerfield Beach, Fla.)*, vol. 27, no. 20, pp. 3165–3169, 2015.

[28] H. Gu, X. Qian, X. Li, B. Craven, W. Zhu, A. Cheng, S. C. Yao, and Q. M. Zhang, "A chip scale electrocaloric effect based cooling device," *Applied Physics Letters*, vol. 102, no. 12, 2013.

[29] S. Zhang, R. Xia, and T. R. Shrout, "Lead-free piezoelectric ceramics vs. PZT?," *Journal of Electroceramics*, vol. 19, no. 4, pp. 251–257, 2007.

[30] N. Zhang, H. Yokota, a. M. Glazer, Z. Ren, D. a. Keen, D. S. Keeble, P. a. Thomas, and Z.-G. Ye, "The missing boundary in the phase diagram of $Pb(Zr_{1-x}Ti_x)O_3$.," *Nature Communications*, vol. 5, p. 5231, jan 2014.

[31] A. K. Tagantsev, K. Vaideeswaran, S. B. Vakhrushev, a. V. Filimonov, R. G. Burkovsky, a. Shaganov, D. Andronikova, a. I. Rudskoy, a. Q. R. Baron, H. Uchiyama, D. Chernyshov, a. Bosak, Z. Ujma, K. Roleder, a. Majchrowski, J.-H. Ko, and N. Setter, "The origin of antiferroelectricity in $PbZrO_3$.," *Nature Communications*, vol. 4, p. 2229, jan 2013.

[32] L. B. Kong, J. Ma, W. Zhu, and O. K. Tan, "Preparation and characterization of lead zirconate ceramics from high-energy ball milled powder," *Materials Letters*, vol. 49, no. June, pp. 96–101, 2001.

[33] D. I. Woodward, J. Knudsen, and I. M. Reaney, "Review of crystal and domain structures in the PZT solid solution," *Physical Review B*, vol. 72, p. 104110, 2005.

[34] B. S. Kwak, A. Erbil, B. J. Wilkens, J. D. Budai, M. F. Chisholm, and L. A. Boatner, "Strain relaxation by domain formation in epitaxial ferroelectric thin films," *Physical Review Letters*, vol. 68, pp. 3733–3736, 1992.

[35] B. Noheda, D. E. Cox, G. Shirane, J. A. Gonzalo, L. E. Cross, and S.-E. Park, "A monoclinic ferroelectric phase in the $Pb(Zr_{1-x}Ti_x)O_3$ solid solution," *Applied Physics Letters*, vol. 2059, no. May 2015, p. 6, 1999.

[36] B. Noheda, J. Gonzalo, L. Cross, and R. Guo, "Tetragonal-to-monoclinic phase transition in a ferroelectric perovskite: The structure of $Pb(Zr_{52}Ti_{48})O_3$," *Physical Review B*, vol. 61, no. 13, pp. 8687–8695, 2000.

[37] B. Noheda and D. E. Cox, "Noheda, Cox - 2006 - Phase Transitions - Bridging phases at the morphotropic boundaries of lead oxide solid solutions.pdf," *Phase Transitions*, vol. 79, pp. 5–20, 2006.

[38] F. Cordero, F. Craciun, M. Dinescu, N. Scarisoreanu, C. Galassi, W. Schranz, and V. Soprunyuk, "Elastic response of (1-x)$Ba(Ti_{0.8}Zr_{0.2})O_3$ - (x$Ba_{0.7}Ca_{0.3}$)TiO_3

(x=0.45-0.55) and the role of the intermediate orthorhombic phase in enhancing the piezoelectric coupling," *Applied Physics Letters*, vol. 105, p. 232904, dec 2014.

[39] S.-E. Park and T. R. Shrout, "Ultrahigh strain and piezoelectric behavior in relaxor based ferroelectric single crystals," *Journal of Applied Physics*, vol. 82, p. 1804, 1997.

[40] A. M. George, J. Iñiguez, and L. Bellaiche, "Anomalous properties in ferroelectrics induced by atomic ordering.," *Nature*, vol. 413, pp. 54–57, 2001.

[41] G. SaghiSzabo and R. E. Cohen, "Long-range order effects in $Pb(Zr_{1/2}Ti_{1/2})O_3$," *Ferroelectrics*, vol. 194, no. 1-4, pp. 287–298, 1997.

[42] L. C. Zhang, A. L. Vasiliev, I. B. Misirlioglu, R. Ramesh, S. P. Alpay, and M. Aindow, "Cation ordering in epitaxial lead zirconate titanate films," *Applied Physics Letters*, vol. 93, 2008.

[43] R. Kirchhofer, D. R. Diercks, B. P. Gorman, J. F. Ihlefeld, P. G. Kotula, C. T. Shelton, and G. L. Brennecka, "Quantifying Compositional Homogeneity in $Pb(Zr, Ti)O_3$ Using Atom Probe Tomography," *Journal of the American Ceramic Society*, vol. 97, no. 34858, pp. 2677–2697, 2014.

[44] A. A. Bokov and Z. G. Ye, "Recent progress in relaxor ferroelectrics with perovskite structure," *Journal of Materials Science*, vol. 41, no. 1, pp. 31–52, 2006.

[45] R. A. Cowley, S. N. Gvasaliya, S. G. Lushnikov, B. Roessli, and G. M. Rotaru, "Relaxing with relaxors: a review of relaxor ferroelectrics," *Advances in Physics*, vol. 60, no. 2, pp. 229–327, 2011.

[46] K. Uchino, *Piezoelectric Actuators and Ultrasonic Motors*. Springer, 1997.

[47] S. E. E. Park and W. Hackenberger, "High performance single crystal piezoelectrics: Applications and issues," *Current Opinion in Solid State and Materials Science*, vol. 6, no. 1, pp. 11–18, 2002.

[48] IBM, "Research Communications."

[49] P. Ghosez and J. Junquera, "Chapter 134 : First-Principles Modeling of Ferroelectric Oxides Nanostructures," *Handbook of Theorectical and Computational Nanotechnology*, 2006.

[50] P. Ewald, "Die Berechnung optischer und elektrostatischer Gitterpotentiale," *Annalen der Physik*, vol. 369, no. 3, pp. 253–287, 1921.

[51] M. P. Allen and D. J. Tildesley, *Computer Simulation of Liquids*, vol. 5. Oxford University Press, 1989.

[52] B. Dick and A. Overhauser, "Theory of the Dielectric Constants of Alkali Halide Crystals," *Physical Review*, vol. 112, no. 1, pp. 90–103, 1958.

[53] D. F. Shanno, "Conditioning of quasi-Newton methods for function minimization," *Mathematics of Computation*, vol. 24, pp. 647–647, 1970.

[54] M. Allen, "Introduction to molecular dynamics simulation," *Computational Soft Matter*, vol. 23, pp. 1–28, 2004.

[55] H. C. Andersen, "Rattle: A velocity version of the shake algorithm for molecular dynamics calculations," *Journal of Computational Physics*, vol. 52, pp. 24–34, 1983.

[56] L. Verlet, "Computer "experiments" on classical fluids. I. Thermodynamical properties of Lennard-Jones molecules," *Physical Review*, vol. 159, pp. 98–103, 1967.

[57] R. W. Hockney and J. W. Eastwood, *Computer Simulation Using Particles*, vol. 25. 1988.

[58] H. J. C. Berendsen, J. P. M. Postma, W. F. van Gunsteren, A. DiNola, and J. R. Haak, "Molecular dynamics with coupling to an external bath," *The Journal of Chemical Physics*, vol. 81, pp. 3684–3690, 1984.

[59] S. Nosé, "A unified formution of the constant temperature molecular dynamics methods," *Journal of Chemical Physics*, vol. 81, pp. 511–519, 1984.

[60] W. G. Hoover, "Canonical dynamics: Equilibrium phase-space distributions," *Physical Review A*, vol. 31, pp. 1695–1697, 1985.

[61] K. W. Hohenberg P, "Inhomogeneous electron gas," *Physical Review*, vol. 136, no. 3B, pp. 1912–1919, 1964.

[62] W. Kohn and L. J. Sham, "Self-consistent equations including exchange and correlation effects," *Physical Review*, vol. 140, no. 4A, 1965.

[63] D. M. Ceperley and B. J. Alder, "Ground state of the electron gas by a stochastic method," *Physical Review Letters*, vol. 45, pp. 566–569, 1980.

[64] J. Perdew, K. Burke, and M. Ernzerhof, "Generalized Gradient Approximation Made Simple.," *Physical Review Letters*, vol. 77, pp. 3865–3868, 1996.

[65] C. Fiolhais, F. Nogueira, M. Marques, and E. Engel, *A Primer in Density Functional Theory*. Heidelberg: Springer, 2003.

[66] R. D. King-Smith and D. Vanderbilt, "Theory of polarization of crystalline solids," *Physical Review B*, vol. 47, no. 3, pp. 1651–1654, 1993.

[67] R. Resta, "Macroscopic polarization in crystalline dielectrics: The geometric phase approach," *Reviews of Modern Physics*, vol. 66, no. 3, pp. 899–915, 1994.

[68] M. Sepliarsky and R. E. Cohen, "First-principles based atomistic modeling of phase stability in PMN-xPT.," *Journal of Physics: Condensed matter*, vol. 23, p. 435902, 2011.

[69] A. García and D. Vanderbilt, "Electromechanical behavior of $BaTiO_3$ from first principles," *Applied Physics Letters*, vol. 72, no. 1998, pp. 2981–2983, 1998.

[70] A. L. Kholkin, N. A. Pertsev, and A. V. Goltsev, "Piezoelectricity and crystal symmetry," in *Piezoelectric and Acoustic Materials for Transducer Applications*, pp. 17–38, 2008.

[71] T. Hashimoto and H. Moriwake, "Dielectric properties of $BaTiO_3$ by molecular dynamics simulations using a shell model," *Molecular Simulation*, vol. 7022, no. May 2015, pp. 1–7, 2014.

[72] "Gindeleo Github Repositories." `https://github.com/gindeleo?tab=repositories`. Accessed: 2016-11-28.

[73] J. D. Gale, "GULP: A computer program for the symmetry-adapted simulation of solids," *Journal of the Chemical Society, Faraday Transactions*, vol. 93, pp. 629–637, 1997.

[74] I. T. Todorov, W. Smith, K. Trachenko, and M. T. Dove, "DL_POLY_3: new dimensions in molecular dynamics simulations via massive parallelism," *Journal of Materials Chemistry*, vol. 16, no. 20, p. 1911, 2006.

[75] S. J. Clark, M. D. Segall, C. J. Pickard, P. J. Hasnip, M. I. J. Probert, K. Refson, M. C. Payne, M. D. S. Ii, C. J. P. Ii, P. J. H. Iii, M. I. J. P. Iv, and K. R. V, "First principles methods using CASTEP," *Zeitschrift fuer Kristallographie*, vol. 220, pp. 567–570, 2005.

[76] J. VandeVondele, M. Krack, F. Mohamed, M. Parrinello, T. Chassaing, and J. Hutter, "QUICKSTEP: Fast and accurate density functional calculations using a mixed Gaussian and plane waves approach," *Computer Physics Communications*, vol. 167, pp. 103–128, 2005.

[77] A. M. Glazer and S. A. Mabud, "Powder profile refinement of lead zirconate titanate at several temperatures. II. Pure $PbTiO_3$," *Acta Crystallographica Section B*, vol. 34, no. 4, pp. 1065–1070, 1978.

[78] S. Piskunov, A. Gopeyenko, E. Kotomin, Y. Zhukovskii, and D. E. E. Ellis, "Atomic and electronic structure of perfect and defective $PbZrO_3$ perovskite: Hybrid DFT calculations of cubic and orthorhombic phases," *Computational Materials Science*, vol. 41, pp. 195–201, dec 2007.

[79] R. Guo, L. E. Cross, S.-E. Park, B. Noheda, D. E. Cox, and G. Shirane, "Origin of the High Piezoelectric Response in $Pb(Zr_{1-x}Ti_x)O_3$," *Physical Review Letters*, vol. 84, pp. 5423–5426, 2000.

[80] D. Vanderbilt, "First-principles based modelling of ferroelectrics," *Current Opinion in Solid State and Materials Science*, vol. 2, no. 6, pp. 701–705, 1997.

[81] K. M. Rabe and P. Ghosez, "First-principles studies of ferroelectric oxides," *Topics in Applied Physics*, vol. 105, pp. 117–174, 2007.

[82] P. Marton, T. Shimada, T. Kitamura, and C. Elsässer, "First-principles study of the interplay between grain boundaries and domain walls in ferroelectric $PbTiO_3$," *Physical Review B*, vol. 83, no. 6, 2011.

[83] X. Liu, Y. Wang, P. V. Lukashev, J. D. Burton, and E. Y. Tsymbal, "Interface dipole effect on thin film ferroelectric stability: First-principles and phenomenological modeling," *Physical Review B*, vol. 85, no. 12, 2012.

[84] T. Shimada, K. Wakahara, Y. Umeno, and T. Kitamura, "Shell model potential for $PbTiO_3$ and its applicability to surfaces and domain walls," *Journal of Physics: Condensed Matter*, vol. 20, p. 325225, aug 2008.

[85] T. Kitamura, Y. Umeno, F. Shang, T. Shimada, and K. Wakahara, "Development of Interatomic Potential for $Pb(Zr, Ti)O_3$ Based on Shell model," *Journal of Solid Mechanics and Materials Engineering*, vol. 1, no. 12, pp. 1423–1431, 2007.

[86] C. J. Pickard and R. J. Needs, "High-pressure phases of silane," *Physical Review Letters*, vol. 97, p. 045504, 2006.

[87] C. J. Pickard and R. J. Needs, "Ab initio random structure searching.," *Journal of Physics. Condensed Matter*, vol. 23, no. 5, p. 53201, 2011.

[88] D. Vanderbilt, "Soft self-consistent pseudopotentials in a generalized eigenvalue formalism," *Physical Review B*, vol. 41, pp. 7892–7895, 1990.

[89] Z. Wu and H. Krakauer, "First-principles calculations of piezoelectricity and polarization rotation in $Pb(Zr_{0.5}Ti_{0.5})O_3$," 2003.

[90] B. Noheda, N. Cereceda, T. Iglesias, G. Lifante, and J. A. Gonzalo, "Composition dependence of the ferroelectric paraelectric transition in the mixed system pzt," vol. 51, no. 22, pp. 388–391, 1995.

[91] Y. Chen, B. Liu, Y. Ma, and Y. Zhou, "Modification of a shell model for the study of the radiation effects in $BaTiO_3$," *Nuclear Instruments and Methods in Physics Research, Section B*, vol. 267, pp. 1–7, sep 2009.

[92] X.-j. Zheng, L.-p. Tang, Q.-y. Wu, and B. Wu, "Evaluation of effective elastic constants for polycrystalline PZT thin films by XRD patterns and pole figures," *Journal of Central South University of Technology*, vol. 14, pp. 130–133, feb 2007.

[93] S. P. Beckman, X. Wang, K. M. Rabe, and D. Vanderbilt, "Ideal barriers to polarization reversal and domain-wall motion in strained ferroelectric thin films," *Physical Review B*, vol. 79, no. December 2008, pp. 1–8, 2009.

[94] B. Jaffe, W. Cook, and H. Jaffe, *Piezoelectric Ceramics*, vol. 41. London and New York: Academic Press, 1971.

[95] S. Kumar, D. a. Ochoa, J. E. García, and K. B. R. Varma, "Relaxor Ferroelectric Behavior and Structural Aspects of $SrNaBi_2Nb_3O_{12}$ Ceramics," *Journal of the American Ceramic Society*, vol. 95, pp. 1339–1342, apr 2012.

[96] D. I. Bilc, R. Orlando, R. Shaltaf, G. M. Rignanese, J. Íñiguez, and P. Ghosez, "Hybrid exchange-correlation functional for accurate prediction of the electronic and structural properties of ferroelectric oxides," *Physical Review B*, vol. 77, no. 16, pp. 1–13, 2008.

[97] J. P. Perdew, A. Ruzsinszky, G. I. Csonka, O. a. Vydrov, G. E. Scuseria, L. a. Constantin, X. Zhou, and K. Burke, "Generalized gradient approximation for solids and their surfaces," *Physical Review Letters*, vol. 136406, no. April, pp. 1–4, 2007.

[98] S. Goedecker, M. Teter, and J. Hutter, "Separable dual-space Gaussian pseudopotentials," *Physical Review B*, vol. 54, no. 3, pp. 1703–1710, 1996.

[99] J. VandeVondele and J. Hutter, "Gaussian basis sets for accurate calculations on molecular systems in gas and condensed phases," *Journal of Chemical Physics*, vol. 127, 2007.

[100] S. Poykko and D. J. Chadi, "Ab initio study of 180 degrees domain wall energy and structure in $PbTiO_3$," *Applied Physics Letters*, vol. 75, pp. 2830–2832, 1999.

[101] T. Shimada, Y. Umeno, and T. Kitamura, "Ab initio study of stress-induced domain switching in $PbTiO_3$," 2008.

[102] A. P. Sutton and J. Chen, "Long-range Finnis-Sinclair potentials," *Philosophical Magazine Letters*, vol. 61, no. 3, pp. 139–146, 1990.

[103] M. A. Mclachlan, D. W. Mccomb, M. P. Ryan, A. N. Morozovska, E. A. Eliseev, E. A. Payzant, S. Jesse, K. Seal, A. P. Baddorf, and S. V. Kalinin, "Probing local and global ferroelectric phase stability and polarization switching in ordered macroporous PZT," *Advanced Functional Materials*, vol. 21, no. 5, pp. 941–947, 2011.

[104] H. C. Nie, X. F. Chen, N. B. Feng, G. S. Wang, X. L. Dong, Y. Gu, H. L. He, and Y. S. Liu, "Effect of external fields on the switching current in PZT ferroelectric ceramics," *Solid State Communications*, vol. 150, no. 1-2, pp. 101–103, 2010.

[105] J. Y. Li, R. C. Rogan, E. Ustündag, and K. Bhattacharya, "Domain switching in polycrystalline ferroelectric ceramics.," *Nature Materials*, vol. 4, no. 10, pp. 776–781, 2005.

[106] J. Li, B. Nagaraj, H. Liang, W. Cao, C. H. Lee, and R. Ramesh, "Ultrafast polarization switching in thin-film ferroelectrics," *Applied Physics Letters*, vol. 84, no. 7, pp. 1174–1176, 2004.

[107] J. Y. Jo, H. S. Han, J. G. Yoon, T. K. Song, S. H. Kim, and T. W. Noh, "Domain switching kinetics in disordered ferroelectric thin films," *Physical Review Letters*, vol. 99, no. 26, pp. 1–4, 2007.

[108] M. Sepliarsky, S. R. Phillpot, S. K. Streiffer, M. G. Stachiotti, and R. L. Migoni, "Polarization reversal in a perovskite ferroelectric by molecular-dynamics simulation," *Applied Physics Letters*, vol. 79, no. 26, pp. 4417–4419, 2001.

[109] T. Nishimatsu, U. V. Waghmare, Y. Kawazoe, and D. Vanderbilt, "Fast molecular-dynamics simulation for ferroelectric thin-film capacitors using a first-principles effective Hamiltonian," *Physical Review B*, vol. 78, no. 10, pp. 1–11, 2008.

[110] X. Zeng and R. E. Cohen, "Thermo-electromechanical response of a ferroelectric perovskite from molecular dynamics simulations," *Applied Physics Letters*, vol. 99, no. 14, p. 142902, 2011.

[111] K. B. Lazarus, E. F. Crawley, J. D. Bohlmann, and F. Worth, "Static aeroelastic control using strain actuated adaptive structures," *Journal of Intelligent Material Systems and Structures*, vol. 2, no. 3, pp. 386–440, 1991.

[112] Y. H. Zhao and H. Y. Hu, "Active Control of Vertical Tail Buffeting by Piezoelectric Actuators," *Journal of Aircraft*, vol. 46, no. 4, pp. 1167–1175, 2009.

[113] P. Jänker, F. Claeyssen, R. Leletty, O. Sosniki, A. Pages, G. Magnac, and M. Christmann, "New Actuators for Aircraft , Space and Military Applications," *ACTUATOR 2010, 12th International Conference on New Actuators*, no. June, pp. 346–354, 2008.

[114] J. Wooldridge, S. Ryding, S. Brown, T. L. Burnett, M. G. Cain, R. Cernik, R. Hino, M. Stewart, and P. Thompson, "Simultaneous measurement of X-ray diffraction and

ferroelectric polarization data as a function of applied electric field and frequency," *Journal of Synchrotron Radiation*, vol. 19, no. 5, pp. 710–716, 2012.

[115] S. Ryding, R. Cernik, J. Wooldridge, T. L. Burnett, M. Stewart, C. Vecchini, M. G. Cain, A. Lennie, F. Yuan, C. Tang, and P. Thompson, "Simultaneous measurement of X-ray powder diffraction and ferroelectric polarisation data as a function of applied electric field at a range of frequencies," *Powder Diffraction*, vol. 28, no. S2, pp. S220–S227, 2013.

[116] D. Wang, Y. Fotinich, and G. P. Carman, "Influence of temperature on the electromechanical and fatigue behavior of piezoelectric ceramics," *Journal of Applied Physics*, vol. 83, no. 10, p. 5342, 1998.

[117] M. W. Hooker, "Properties of PZT-Based Piezoelectric Ceramics Between -150 and 250 C," *Lockheed Martin Engineering Sciences Company*, no. September, p. 28, 1998.

[118] F. Yan, G. Z. Xing, and L. Li, "Low temperature dependent ferroelectric resistive switching in epitaxial $BiFeO_3$ films," *Applied Physics Letters*, vol. 104, no. 13, pp. 13–17, 2014.

[119] A. Jiang, M. Dawber, J. F. Scott, C. Wang, P. Migliorato, and M. Gregg, "Studies of Switching Kinetics in Ferroelectric Thin Films," *Japanese Journal of Applied Physics, Part 1*, vol. 42, no. 11, pp. 6973–6982, 2003.

[120] W. J. Hu, D.-M. Juo, L. You, J. Wang, Y.-C. Chen, Y.-H. Chu, and T. Wu, "Universal ferroelectric switching dynamics of vinylidene fluoride-trifluoroethylene copolymer films.," *Scientific Reports*, vol. 4, p. 4772, 2014.

[121] Y.-H. Shin, I. Grinberg, I.-W. Chen, and A. M. Rappe, "Nucleation and growth mechanism of ferroelectric domain-wall motion.," *Nature*, vol. 449, pp. 881–884, oct 2007.

[122] I. Stolichnov, A. Tagantsev, N. Setter, J. S. Cross, and M. Tsukada, "Crossover between nucleation-controlled kinetics and domain wall motion kinetics of polarization reversal in ferroelectric films," *Applied Physics Letters*, vol. 83, no. 16, pp. 3362–3364, 2003.

[123] A. V. Kimmel, P. M. Weaver, M. G. Cain, and P. V. Sushko, "Defect-mediated lattice relaxation and domain stability in ferroelectric oxides," *Physical Review Letters*, vol. 109, no. 11, pp. 1–5, 2012.

[124] Y. W. So, D. J. Kim, T. W. Noh, J.-G. G. Yoon, and T. K. Song, "Polarization switching kinetics of epitaxial $Pb(Zr_{0.4}Ti_{0.6})O_3$ thin films," *Applied Physics Letters*, vol. 86, no. 9, p. 92905, 2005.

[125] M. Avrami, "Kinetics of Phase Change. II - Transformation-Time Relations for Random Distribution of Nuclei," *Journal of Chemical Physics*, vol. 8, no. 1940, pp. 212–224, 1940.

[126] M. V. Rane, A. Navrotsky, and G. a. Rossetti, "Enthalpies of Formation of Lead Zirconate Titanate (PZT) Solid Solutions," *Journal of Solid State Chemistry*, vol. 161, pp. 402–409, 2001.

[127] M. Ceramics, "PZT ceramics." url = http://www.morgantechnicalceramics.com/products/product-groups/piezo-ceramic-components/piezo-ceramic-tutorials/typical-properties. Accessed: 2016-07-25.

[128] D. Wu, Q. Zhou, K. K. Shung, S. N. Bharadwaja, D. Zhang, and H. Zheng, "Dielectric and piezoelectric properties of PZT composite thick films with variable solution to powder ratios," *Journal of the American Ceramic Society*, vol. 92, no. 6, pp. 1276–1279, 2009.

[129] I. Ponomareva and S. Lisenkov, "Bridging the Macroscopic and Atomistic Descriptions of the Electrocaloric Effect," *Physical Review Letters*, vol. 108, no. 16, p. 167604, 2012.

[130] S. Kar-Narayan and N. D. Mathur, "Direct and indirect electrocaloric measurements using multilayer capacitors," *Journal of Physics D: Applied Physics*, vol. 43, no. 3, p. 032002, 2010.

[131] S. G. Lu, B. Rožič, Q. M. Zhang, Z. Kutnjak, X. Li, E. Furman, L. J. Gorny, M. Lin, B. Malič, M. Kosec, R. Blinc, and R. Pirc, "Organic and inorganic relaxor ferroelectrics with giant electrocaloric effect," *Applied Physics Letters*, vol. 97, no. 16, 2010.

[132] S. G. Lu, B. Rožič, Q. M. Zhang, Z. Kutnjak, R. Pirc, M. Lin, X. Li, and L. Gorny, "Comparison of directly and indirectly measured electrocaloric effect in relaxor ferroelectric polymers," *Applied Physics Letters*, vol. 97, no. 20, 2010.

[133] T. Zhang, W. Li, Y.-F. Hou, Y. Yu, W. P. Cao, Y. Feng, and W. Fei, "Positive/Negative Electrocaloric Effect Induced by Defect Dipoles in PZT Ferroelectric Bilayer Thin Films," *Royal Society of Chemistry Advances*, vol. 6, pp. 71934–71939, 2016.

[134] Z. Zuo, B. Chen, B. Wang, H. Yang, Q. Zhan, Y. Liu, J. Wang, and R.-W. Li, "Strain assisted electrocaloric effect in $Pb(Zr_{0.95}Ti_{0.05})O_3$ films on $0.7Pb(Mg_{1/3}Nb_{2/3})O_3$-$0.3PbTiO_3$ substrate," *Scientific Reports*, vol. 5, no. October, p. 16164, 2015.

[135] J. H. Qiu and Q. Jiang, "Misfit strain dependence of electrocaloric effect in epitaxial $Pb(Zr_{1-x}Ti_x)O_3$ thin films," *Journal of Applied Physics*, vol. 103, no. 8, 2008.

[136] U. D. C. Rica and S. Jos, "Why is the electrocaloric effect so small in ferroelectrics?," vol. 064106, 2016.

[137] M. C. Rose and R. E. Cohen, "Giant electrocaloric effect around Tc," *Physical Review Letters*, vol. 109, no. November, pp. 1–5, 2012.

[138] R. Pirc, B. Rožič, J. Koruza, B. Malič, and Z. Kutnjak, "Negative electrocaloric effect in antiferroelectric $PbZrO_3$," *EPL (Europhysics Letters)*, vol. 107, no. 1, p. 17002, 2014.

[139] Y. Liu, J. F. Scott, and B. Dkhil, "Some strategies for improving caloric responses with ferroelectrics," vol. 064109, pp. 0–9, 2016.

[140] B. Li, X. Zhang, J. B. Wang, X. L. Zhong, F. Wang, and Y. C. Zhou, "Giant electrocaloric effect of $PbTiO_3$ thin film tuned in a wide temperature range by the anisotropic misfit strain," *Mechanics Research Communications*, vol. 55, pp. 40–44, 2014.

[141] X. Wu and D. Vanderbilt, "Theory of hypothetical ferroelectric superlattices incorporating head-to-head and tail-to-tail 180 domain walls," *Physical Review B*, vol. 73, no. 2, pp. 1–4, 2006.

[142] K. Rahmanizadeh, D. Wortmann, G. Bihlmayer, and S. Blügel, "Charge and orbital order at head-to-head domain walls in $PbTiO_3$," *Physical Review B*, vol. 90, no. 11, p. 115104, 2014.

[143] R. M. Martin, *Electronic Structure: Basic Theory and Practical Methods*. Cambridge University Press, 2004.

[144] G. Shirane, S. Hoshino, and K. Suzuki, "X-Ray Study of the Phase Transition in Lead Titanate," *Physical Review*, vol. 80, no. 6, pp. 1105–1106, 1950.

[145] C. H. Peng, J.-F. Chang, and S. B. Desu, "Optical Properties of PZT, PLZT, and PNZT Thin Films," in *Symposium G - Wide Band-Gap Semiconductors*, vol. 243 of *MRS Proceedings*, p. 21 (6 pages), 1991.

[146] E. Snoeck, A. Lubk, and C. Magen, *Structural Characterization of Ferroelectric and Multiferroic Nanostructures by Advanced TEM Techniques*, pp. 275–324. John Wiley Sons, 2016.

[147] T. Sluka, A. K. Tagantsev, P. Bednyakov, and N. Setter, "Free-electron gas at charged domain walls in insulating $BaTiO_3$," *Nature Communications*, vol. 4, no. May, p. 1808, 2013.

[148] Y. F. Zhukovskii, E. A. Kotomin, S. Piskunov, and D. E. Ellis, "A comparative ab initio study of bulk and surface oxygen vacancies in $PbTiO_3$, $PbZrO_3$ and $SrTiO_3$ perovskites," *Solid State Communications*, vol. 149, no. 33-34, pp. 1359–1362, 2009.

[149] A. Stashans, S. Serrano, and P. Medina, "A quantum-chemical study of oxygen-vacancy defects in $PbTiO_3$ crystals," *Physica B*, vol. 381, no. 1-2, pp. 82–89, 2006.

[150] E. A. Kotomin, Y. F. Zhukovskii, S. Piskunov, and D. E. Ellis, "Hybrid DFT calculations of the F centers in cubic ABO_3 perovskites," *Journal of Physics: Conference Series*, vol. 117, p. 012019, 2008.

[151] M. V. Ganduglia-Pirovano, "Oxygen defects at reducible oxide surfaces: The example of ceria and vanadia," *Springer Series in Surface Sciences*, vol. 58, pp. 149–190, 2015.

[152] T. Xu, T. Shimada, Y. Araki, J. Wang, and T. Kitamura, "Multiferroic Domain Walls in Ferroelectric $PbTiO_3$ with Oxygen Deficiency," *Nano Letters*, vol. 16, no. 1, pp. 454–458, 2016.

[153] R. K. Behera, C.-W. Lee, D. Lee, A. N. Morozovska, S. B. Sinnott, A. Asthagiri, V. Gopalan, and S. R. Phillpot, "Structure and energetics of 180 domain walls in $PbTiO_3$ by density functional theory.," *Journal of Physics: Condensed matter*, vol. 23, no. 17, p. 175902, 2011.

[154] B. Meyer and D. Vanderbilt, "Ab initio study of ferroelectric domain walls in $PbTiO_3$," *Physical Review B*, vol. 65, no. September 2001, p. 12, 2001.

[155] X. Jiang, Q. Yang, and J. Cao, "The effect of domain walls on leakage current in $PbTiO_3$ thin films," *Physics Letters A*, vol. 380, no. 9-10, pp. 1071–1074, 2016.

[156] A. Chandrasekaran, X.-K. Wei, L. Feigl, D. Damjanovic, N. Setter, and N. Marzari, "Asymmetric structure of 90 domain walls and interactions with defects in $PbTiO_3$," *Physical Review B*, vol. 93, no. 14, p. 144102, 2016.

[157] J. Guyonnet, I. Gaponenko, S. Gariglio, and P. Paruch, "Conduction at domain walls in insulating $Pb(Zr_{0.2}Ti_{0.8})O_3$ thin films.," *Advanced Materials*, vol. 23, no. 45, pp. 5377–82, 2011.

[158] D. Meier, J. Seidel, C. A, K. Delaney, Y. Kumagai, M. Mostovoy, N. Spaldin, R. Ramesh, and M. Fiebig, "Anisotropic conductance at improper ferroelectric domain walls," *Nature Materials*, vol. 11, no. 4, pp. 284–288, 2012.

[159] W. Wu, Y. Horibe, N. Lee, S. W. Cheong, and J. R. Guest, "Conduction of topologically protected charged ferroelectric domain walls," *Physical Review Letters*, vol. 108, no. 7, 2012.